CRANFIELD UNIVERSITY

L.SMITH

MICRO-STABILISED SIGHTLINE FOR MISSILE APPLICATIONS

CRANFIELD DEFENCE AND SECURITY

MSc THESIS

Academic Year: 2011-12

Supervisor: Dr. M. Richardson

March 2012

CRANFIELD UNIVERSITY

CRANFIELD DEFENCE AND SECURITY

MSc THESIS

Academic Year 2011-2012

L SMITH

Micro-Stabilised Sightline for Missile Applications

Supervisor: Dr M Richardson

September 2012

This thesis is submitted in partial fulfilment of the requirements for the degree of Master of Science

Abstract

The feasibility of un-cooled long wave infrared (LWIR) imager line of sight (LOS) stabilization without the use of gimbals has been assessed with the aim of improving the existing performance of electro-optics (EO) sensors. In order to accomplish this, an initial review of current state of the art electro-optical systems is made in order to assess their potential for this application. Following this review the most promising candidate technologies are down selected and several options are chosen for further study and analysis.

Acknowledgments

This MSc thesis would not be possible without the support of many people. The author wishes to express gratitude to his supervisor Dr. Mark Richardson of Cranfield University for his invaluable assistance throughout. He would like to express gratitude to members of Sagem Défense Sécurité for their ongoing inputs and to members of Selex Galileo for their knowledge and assistance. Special thanks to his family and friends for their constant support throughout his studies.

Table of Contents

Introduction and Project Aims 1

1. Basic Optics 2

1.1 Optical Systems 2

1.2 Types of Mirror 3

1.3 Types of Lens 4

1.4 Available Infrared Lenses 6

1.5 Transmission and Reflection 7

1.6. Image Stabilisation Techniques in Cameras [8] 7

1.7. Optics Equations [9] 8

1.7.1 Plane Mirrors 8

1.7.2 Spherical Surface Mirrors 9

1.7.3 Thin Lenses 9

1.7.4 Thick Lenses 11

2. State of the Art Electro-Optical Components 12

2.1 Liquid Lenses 12

2.1.1 Electro-wetting 12

2.1.2 Dynamorph Lenses (DML) 13

2.1.3 Mechanical Wetting Lens 14

2.1.4. Available Liquid lens products 16

2.1.5. Summary of Liquid Lenses 16

2.2 Liquid Crystal Lenses 17

2.2.1 Summary of Liquid Crystal Lenses 20

2.3 Beam Steering 20

2.3.1Risley Prisms 21

2.3.2 Risley Gratings 22

2.3.3Decentred Lenses 23

2.3.4 Fast Steering Mirrors (FSM) 25

2.3.5 Currently Available FSM systems 27

2.3.6 Infrared Mirror Coatings 31

2.3.7 Beam Splitters 32

2.3.8 Summary of Beam Steering 32

2.4 Micro Electro-Mechanical Systems (MEMS) 33
2.4.1 Electro-Thermal Based MEMS Micro-Mirrors 33
2.4.2 Electrostatic Based MEMS Micro-Mirrors 42
2.4.3 Summary of MEMS 49
2.5 Non-Linear Materials 50
2.5.1 Summary of Non-Linear Materials 52
2.6 State of the Art Electro Optics Conclusion 53
3. Zemax Optical Design 1 55
3.1 Subsystem Specification 55
3.2 Lens Materials 56
3.3 Design Basis 59
3.3.1 Setting System Characteristics 60
3.4 Initial Design Development 61
3.4.1 System Analysis 62
3.4.2 Conclusion 63
3.5 Stage 2 Design Development 64
3.5.1System Design 64
3.5.2 System Analysis 65
3.5.3 Conclusion 66
3.6 Stage 3 Design Development 67
3.6.1 System Design 67
3.6.2 System Analysis 69
3.6.3 Conclusion 70
3.7 Stage 4 Design Development 70
3.7.1 System Design 70
3.7.2 System Analysis 71
3.7.3 Conclusion 73
3.8 Athermalisation 74
3.8.1 System Analysis 70°C 74
3.8.2 System Analysis -40°C 76
3.8.3 Conclusion 78
3.9 Decentred Capabilities 79

3.10 Conclusion 80
4. Zemax Optical Design 2 81
4.1 Design Basis 81
4.1.1Things to be adjusted in this design 82
4.2 Stage 1 Design Development 82
4.2.1 On axis Analysis 83
4.2.2 Decentered Analysis 87
4.3 Stage 2 Design Development 90
4.3.1On Axis System Analysis 90
4.3.2 Decentered System Analysis 93
4.4 Athermalisation 99
5. Summary 103
5.1 Design 1 103
5.2 Design 2 104
5.3 Other Technologies 105
6. References 106

Introduction and Project Aims

The aim of the project is to improve the existing performance of electro-optics (EO) sensors by assessing the feasibility of un-cooled long wave infrared (LWIR) imager line of sight (LOS) stabilization without the use of gimbals. In order to accomplish this, an initial review of current state of the art electro-optical systems will be made in order to assess their potential for this application. Following this review the most promising candidate technologies are down selected and several options are chosen for further study and analysis.

Table 1 outlines the optical sub-system specification provided by the project sponsor. These properties were taken in to account when assessing the current state of the art electro-optical systems for their suitability for this project and were used as parametric inputs in the optical design phase.

Focal length	**48 mm**
F-number	1 - 1.2
Field-Of-View (full)	30° x 22.5°
Field-Of-View at sensor level	25.2 mm x 18.9 mm
Total length (including focal plane)	≤ 150 mm (TBC)
Optical MTF at 2 cy/mrad (42 cy/mm)	> 20% (TBC)
Required field values of MTF (radius at focal plan level)	0 mm
	13 mm
Mass of the moving lens	≤ 50 grams (TBC)
Stroke	Cf. Actuator and Sensor CPS
Temperature range	[-40°C; +70°C]

Table 1 *– Required Optical System Specification*

1. Basic Optics

1.1 Optical Systems

There are two basic types of optical system, reflective and refractive. Both types of system are used to focus radiation from a source on to a detector. Reflective systems use a series of mirrors to direct radiation to a desired focal point. Refractive systems rely on a series of lenses to refract light to a desired focal point.

- Reflective Optical Systems

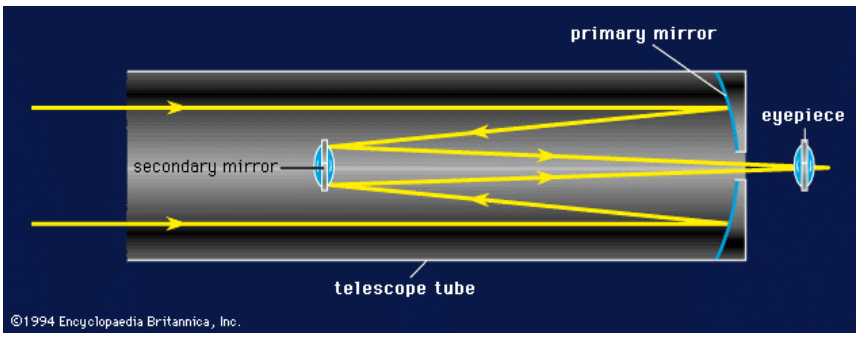

Figure 1 *– Reflecting Telescope* [1]

Reflecting optical systems like the reflecting telescope (***Figure 1)*** work by directing incoming light with a set of curved primary mirrors onto a secondary mirror, which in turn focuses the incoming light onto the eyepiece or detector.

- Refractive Optical Systems

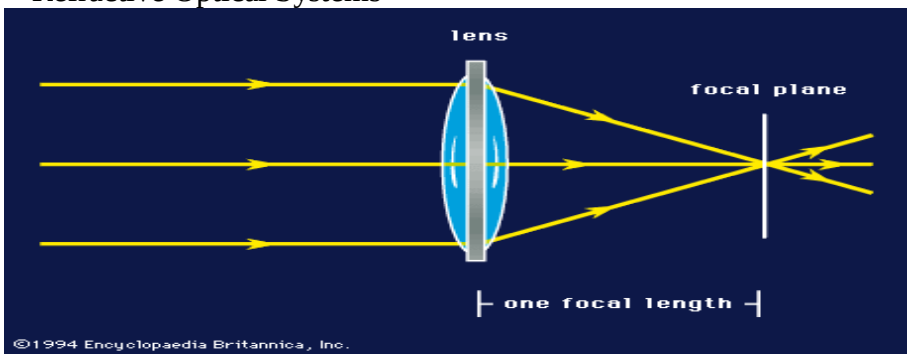

Figure 2 *– Refractive Optical System* [1]

Refracting systems use a lens that is shaped to focus parallel light on to the sensor or focal plane (***Figure 2)***. The distance between the centre of the lens and the focal point is called the focal length. Refractive optical systems generally give higher quality images than reflective systems.

1.2 Types of Mirror

There are three main types of mirror; plane mirrors, converging mirrors and diverging mirrors. Plane mirrors and converging mirrors are often found in optical systems such as telescopes and beam steering equipment. The characteristics of these different types of mirror are outlined below.

- Plane mirror

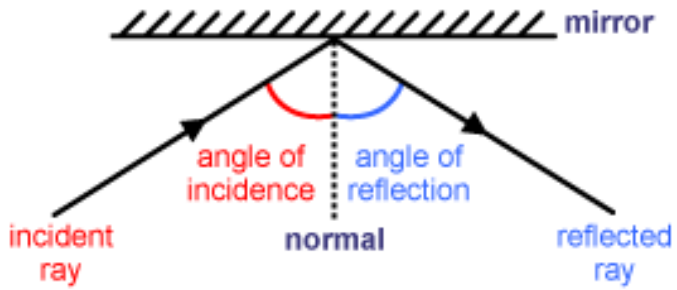

***Figure 3**- Plane Mirror* [2]

The simplest type of mirror to describe is the plane mirror. It is a flat reflecting surface that totally internally reflects incoming radiation at an angle equal to the angle of incidence. As seen in ***Figure 3*** the angle of incidence and reflection are measured from the plane of the wave-front to the normal of the surface. This is a common characteristic shared with all reflecting surfaces, whether a flat surface or a curved surface.

- Converging Mirror

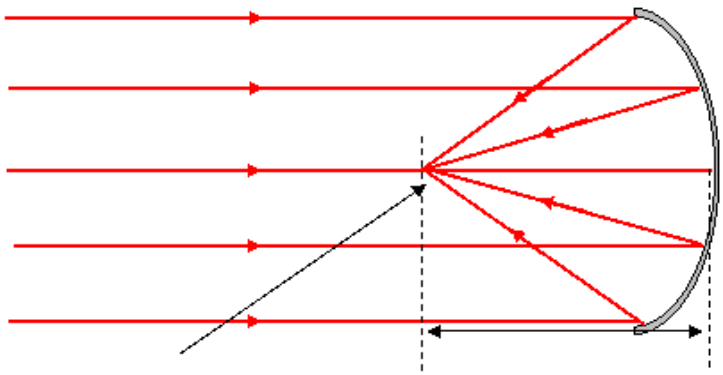

***Figure 4** – Converging mirror* [3]

Curved mirrors also satisfy the rule that angle of incidence equals angle of reflection. The angle of incidence with a curved surface is defined as the angle between the ray and the normal to the tangent of the curved surface at that particular point. In this case where we are looking at a concave or 'converging' mirror, all parallel light coming into the system is focused at one particular point called the focal point (***Figure 4***). The length from the centre of the mirror face to the focal point is called the focal length. Converging mirrors create 'real' focal points that all incident parallel rays pass through.

- Diverging mirror

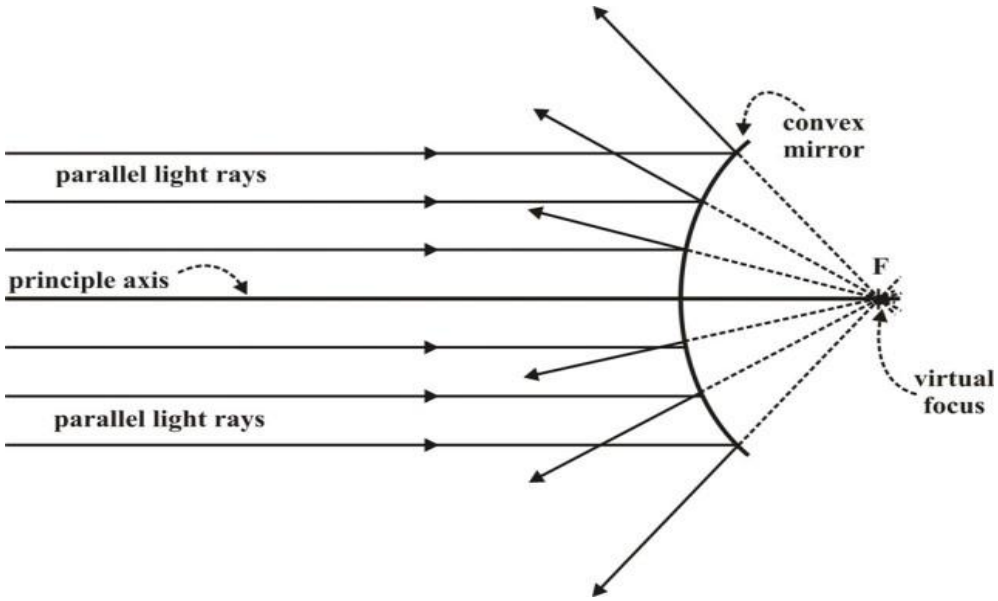

Figure 5 – *Diverging Mirror* [4]

Diverging mirrors separate incident parallel light as shown in ***Figure 5***. When the reflected rays are traced back in a straight line through the mirror it can be seen that a virtual focal point is found, this is where the image 'appears' to be when looking into a diverging mirror.

1.3 Types of Lens

There are two main types of Lens, converging and diverging.

- Converging lenses have similar features to concave mirrors. When parallel light travels through a converging lens it is ‘bent’ towards the focal point as shown in ***Figure 2***. This type of lens is generically used in telescopes and cameras to focus the rays onto a sensor or the user’s retina.

- Diverging lenses are curved in the opposite way to converging lenses as shown in ***Figure 6***. Parallel light travelling through a diverging lens is separated, and so by ray tracing to find the focal point you need to trace backwards to find where the image would appear. This creates what is known as a virtual image. From ***Figure 6*** you can see that incoming light directed at the focal point on the opposite side of the lens is refracted and emerges from the lens parallel to the optical axis. Plano-convex lenses are popular shape lenses that have one flat edge and one curved edge like a converging lens. (***Figure 7***)

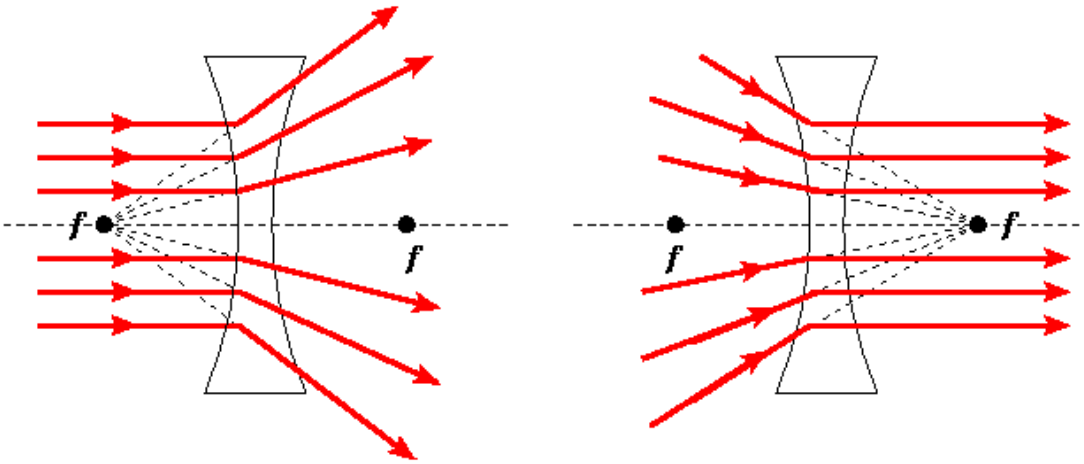

Figure 6 – *The refraction of light through a thin diverging lens* [5]

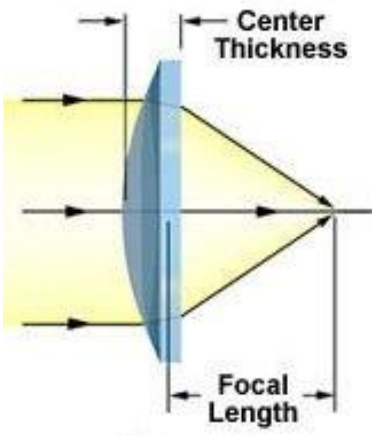

Figure 7 – *Plano-convex lens* [6]

1.4 Available Infrared Lenses

Different materials transmit IR radiation with different wavelengths. Sapphire, Zinc Selenide, Calcium Fluoride and AMTIR-1 are different IR lenses available from Newport Experience Solutions [7].

- Sapphire - These lenses are suitable for high power, high-pressure applications, and vacuum or corrosive atmospheres. Sapphire is a single crystal form of alumina, Al_2O_3. The material is extremely hard and resistant to attack by strong acids. It has high compressive strength, a high melting point, and excellent thermal conductivity. Transmission range is from 150 nm to 5 µm.

- Zinc Selenide - Zinc Selenide lenses are an excellent choice of materials for IR lenses for application between 600 nm to 16 microns wavelengths. Its low absorption coefficient makes it a perfect candidate for applications/instruments using C02 lasers. In Mid IR regime it has a very low GVD which makes it suitable for applications using femtosecond IR pulses. ZnSe aspheric lenses provide diffraction limited focusing performance, making it ideal for focusing the output of a CO_2 laser.

- Calcium Fluoride - Calcium Fluoride lenses are an excellent choice of material for making lenses for UV to Near IR wavelength (180 nm-8 µm). It has a high average transmission and low chromatic aberration compared to various IR materials. In Near IR regime it has a very low GVD which makes it suitable for applications using femtosecond IR pulses.

- AMTIR-1 - These are our most economical IR lenses. AMTIR-1 is a synthetic material transmissive in the Near IR to Mid IR range (800 nm to 16 µm). Transmittance is approximately 70% over the entire range.

- Germanium (Ge)

- Zinc Sulfide (ZnS)

1.5 Transmission and Reflection

Lenses are made from different types of materials as are mirrors. These different materials have different refractive indices arising to different reflection and transmission properties. Optical systems that rely on mirrors to direct incoming light to a sensor generally give bright images, whereas using plain lenses can produce dim images. In order to get the brightest image possible when using a lens system the lenses need to be as wide as possible. When designing an optical system such as telescopes and cameras that work in the visible light section of the electromagnetic spectrum there are many materials that can be used to produce a bright and clear image. However, when designing an optical system for use in the IR range of the spectrum the amount of available materials is more restrictive. The higher refractive indices of the materials available for IR lenses result in higher reflection coefficients. To overcome these higher reflection values IR lenses are coated with low reflective coatings to allow IR radiation to be transmitted at different wavelengths. ***Equation 1*** below calculates the reflection coefficient of a material knowing its refractive index**.**

$$\mathbf{R = (n\text{-}1/n+1)^2} \qquad \textbf{\textit{Equation 1}}$$

Where **R** *is the Reflectivity, and* **n** *is the refractive index.*

1.6. Image Stabilisation Techniques in Cameras [8]

Image Stabilisation techniques are used in cameras to counteract camera and object movements to obtain undistorted still images. In this sub-section these techniques are outlined in order to identify the techniques with the potential to adapt to micro-stabilisation in the infrared. Below is a qualitative description of some of the image stabilisation techniques currently used in photography.

- ISO Based

ISO or International Organisation for Standardisation is a setting on most digital cameras that varies the light sensitivity. To determine the required ISO the focal length and shutter speed are analysed to determine how sharp an image will be. If needed the shutter speed is increased and so the light sensitivity also needs to be increased so to not give a dull image. High sensitivity can often result in noisy images and so other methods of stabilisation are often preferred.

- Sensor Based

Sensor based image stabilisation also uses focal length and shutter speed to analyse what is needed for a successful image. Unlike ISO based stabilisation however Sensor based stabilisation works by physically moving the sensor within the camera body. Sensor based stabilisation was initially used in the DiMAGE A1 camera from Minolta, and has since been employed in the Konica 7D DSLR. The main benefit of using sensor based stabilisation is that lenses can be made smaller as there is less need for lens based image stabilisation.

- Lens Based

Lens based stabilisation works by adjusting a group of lenses inside the lens itself. Gyro sensors inside the lens give two degrees of freedom for pitch and yaw, tracking movement in the object. This is calculated from measuring the optical flow of the target against the stationary background of the image. With this information being fed to a micro-processor the necessary movement of the lens group is computed. Lens based stabilisation is often preferred to other methods as the adjustments are made by tracking the motion of the subject directly. Also the user can see the final image through the view finder since the stabilisation takes place in the lens and not the body of the camera. The Canon Hybrid IS system uses two correction types, one for recognising vibrations or rotational shaking and one for linear movement of the object with respect to the camera, or vice versa.

1.7. Optics Equations [9]

Below are some standard equations used in optics that may help when designing a lens or mirror system.

1.7.1 Plane Mirrors

- For plane mirrors the angle of the incident ray is equal to the angle of the reflected ray.

$$\theta_i = \theta_r \qquad \textbf{\textit{Equation 2}}$$

- Image and object location after reflection

$$s' = -s \qquad \textit{Equation 3}$$

The minus sign shows that the image is virtual and not that it is behind the mirror.

1.7.2 Spherical Surface Mirrors

- Object distance, and image distance are related by the curvature of the mirror.

$$1/s + 1/s' = -2/R \qquad \textit{Equation 4}$$

Where **s** *is the Object distance,*
s' *is the image distance,*
and **R** *is the radius of curvature.*

- Focal length f of a curved mirror is also related to the curvature of the mirror. This is found by setting the object distance to infinity, therefore comparing rays parallel to the optical axis. The focal point is set equal to the image distance as parallel rays from an infinite object distance are focused at the focal point.

$$f = -R/2 \qquad \textit{Equation 5}$$

- So for curved mirrors the focal length is related to the object distance and the image distance by

$$1/s + 1/s' = 1/f \qquad \textit{Equation 6}$$

Convex mirrors always have a negative image distance ($s' < 0$) and therefore create virtual images. Concave mirrors can create real or virtual images. If the object distance is greater than the focal length ($s > f$) a real image is formed, and if the object distance is less than the focal length ($s < f$) then a virtual image is formed.

1.7.3 Thin Lenses

- Refractive index of a material is defined by the ratio of the speed of light in a vacuum to that of the speed of light through the material.

$$\mathbf{n = v_0 / v} \qquad \textbf{\textit{Equation 7}}$$

Where **n** *is the refractive index*
$\boldsymbol{v_0}$ *is the speed of light in a vacuum*
and **v** *is the speed of light through the material in question*

The refractive index of a vacuum is 1 and so all values of v_0/v are greater than 1.

- When radiation travels through an interface between two materials with different refractive indices then the following happens;

    1. The velocity of the wave changes.
    2. The wavelength changes.
    3. The frequency and period remain the same.
    4. If the angle of incidence is not perpendicular to the plane of the interface then the direction of the wave will change.

$$\mathbf{v_1 / v_2 = n_2 / n_1} \qquad \mathbf{\lambda_1/\lambda_2 = n_2 / n_1} \qquad \mathbf{f_1 = f_2} \qquad \textbf{\textit{Equation 8(a), (b) and (c)}}$$

- Snell's Law

$$\mathbf{n_i \sin(\theta_i) = n_r \sin(\theta_r)}$$

$$\mathbf{\therefore \sin(\theta_i) / \sin(\theta_r) = n_r / n_i} \qquad \textbf{\textit{Equation 9}}$$

- Paraxial Ray Approximation (for incident angles of less than 10°)

$$\mathbf{\sin(\theta) \approx \tan(\theta) \approx \theta} \qquad \textbf{\textit{Equation 10}}$$

- Apparent depth using the Paraxial Ray approximation

$$\mathbf{s' = (n_2 / n_1)\, s} \qquad \textbf{\textit{Equation 11}}$$

- When a ray of light is incident on the interface of two materials with different refractive indices at a particular angle, the light runs along the interface and does not pass into the second material. The angle at which this happens is called the critical angle. Any angle larger than the critical angle and the ray is totally internally reflected with the properties of reflected light from a mirror.

$$\mathbf{\theta_c = \sin^{-1} (n_2 / n_1)} \qquad \textbf{\textit{Equation 12}}$$

Where $\boldsymbol{\theta_c}$ *is the critical angle*

1.7.4 Thick Lenses

- The lens maker equation is useful to determine the radii of curvature needed to produce lenses with a particular focal length when made from a material with a known refractive index.

$$\mathbf{1/f = (n_2\text{-}n_1)/n_1\ (1/R_1 - 1/R_2)} \qquad \textit{Equation 13}$$

- Lenses with positive focal length (Converging)
    1. Biconvex
    2. Plano-convex
    3. Convex-concave

  Lenses with negative focal length (Diverging)

    1. Biconcave
    2. Plano-concave
    3. Convex-concave

- Magnification for thin lenses

$$\mathbf{m = h_i / h_o = -s'/s} \qquad \textit{Equation 14}$$

Where $\mathbf{h_i}$ *is the image height*
and $\mathbf{h_o}$ *is the object height*

- Angular magnification

$$\mathbf{M = \alpha_m / \alpha_o} \qquad \textit{Equation 15}$$

Where $\boldsymbol{\alpha_m}$ *is the angle the image makes*
and $\boldsymbol{\alpha_o}$ *is the angle the object makes at the near point.*

2. State of the Art Electro-Optical Components

This chapter provides an outline of the current state of the art electro-optical beam steering and variable focus technologies. This report on state of the art technologies will make it possible to highlight those with the potential to meet the project requirements with regards to the subsystem specification provided by the sponsor.

2.1 Liquid Lenses

The meniscus of certain fluids can be utilized to form variable focus lenses, known as liquid lenses. A lot of attention has recently been paid to the development of liquid lens technology[11,12,13]. Their small radius and variable focal lengths are the main advantages of this technology making them highly suitable components for mobile phone cameras and similar systems. There are various ways of creating liquid lenses that are outlined in this chapter. The two main ways of producing a liquid lens are 'electro-wetting' where the meniscus of a liquid-liquid interface is varied with an applied voltage, and by physically changing the volume of the chamber in which a liquid is contained by use of a piezoelectric actuator.

2.1.1 Electro-wetting

Electro-wetting liquid lenses consist of two immiscible fluids with different refractive indices. One of the fluids is an electrically conducting aqueous solution and the other, a non-conducting oil. The two fluids are cased in a tube with clear caps at either end. The inside of the tube and one of the end caps are coated in a hydrophobic material which repels the aqueous solution towards the non-coated end cap in a semi-spherical converging lens shape (***Figure 8(a)***). By applying an electric field across the hydrophobic coating the surface tension at the interface of the aqueous solution and the solid wall changes, and the solution rises against the walls of the tube in a process called electro-wetting (***Figure 8(b)***). With greater electric fields the conducting fluid rises higher along the tube walls and eventually becomes flat showing no lens like properties (***Figure 8(d)***). Further increase in electric field causes the meniscus to become inverted creating a diverging lens shape (***Figure 8(b), 7(e)***). When there is a change in electric field the resulting response time of the lens is around 10ms.

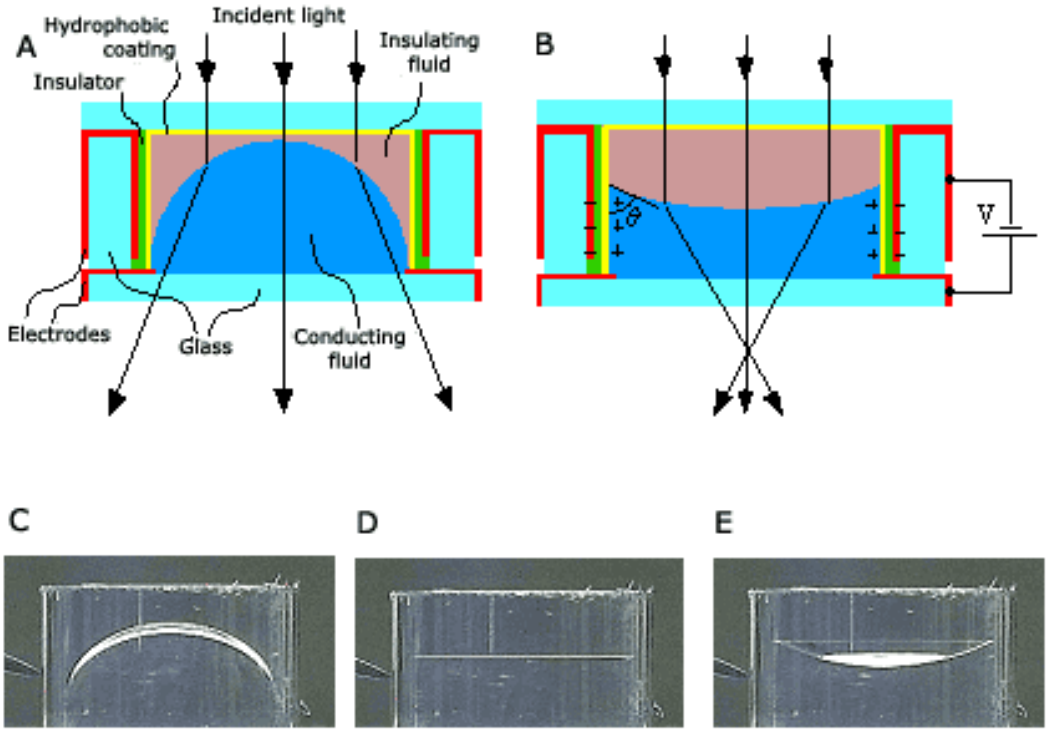

Figure 8 *– Liquid Lenses under different DC voltage* [10]

Daisuke Koyama *et al*. [11] have achieved a response time of 6.7ms using this method with a mixture of degassed water and silicone oil and applying an acoustic radiation force from a transducer.

2.1.2 Dynamorph Lenses (DML)

Hiromasa Oku *et al.*[12] have recorded a response time close to 2ms by capturing high speed video footage through their prototype switching its focal length every 10ms. The lens system consists of two immiscible fluids (ultra purified water and poly-dimethyl-siloxane (PDMS)) with different refractive indices, interfaced at a circular hole which acts as the lens aperture. The two immiscible fluids form the semi-spherical shaped refracting interface when a piezo stack actuator thrusts against a deformable wall in chamber one. This thrust causes chamber one's volume to change and induces a change in shape of the interface. When the piezo stack actuator is extended, chamber one's volume decreases changing the shape of the interface from convex to planar. Further extension of the actuator creates a concave interface that acts as a diverging lens (***Figure 9***).

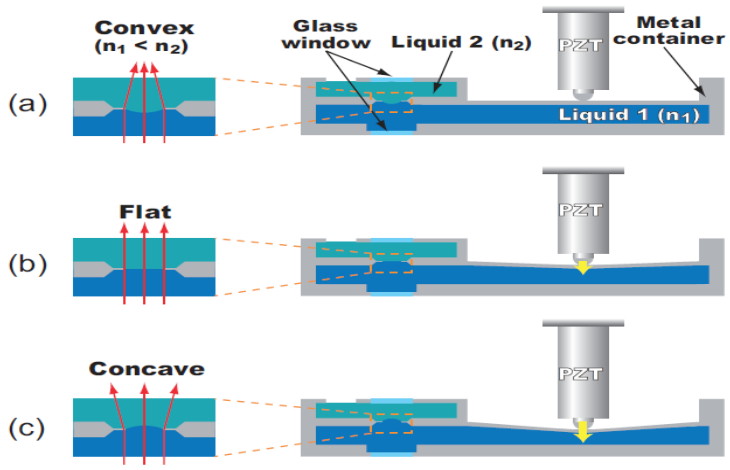

Figure 9 *– Actuation of DML for a) Convex Lenses, b) Plane Lenses, c) Concave Lenses*

2.1.3 Mechanical Wetting Lens

Su Xu *et al.* [13] have developed a liquid lens that doesn't contain Polydimethylsiloxane (PDMS) and can function in the near Infrared part of the spectrum. This Mechanical wetting lens has similarities to the DML lens described above. In these device four actuators are used, two acting on each liquid. To create a converging lens shape the actuators move in a manner which decreases the volume of the aqueous chamber and increases the volume of the oil chamber as shown in ***Figure 10 (c)***. To create a diverging lens the volume of the oil chamber is decreased and the volume of the aqueous chamber is increased (***Figure.10b***). By using Glycerol and ultra-pure water to make the liquid-liquid interface the gravity effect is minimal because they have similar densities, and there is a large refractive index difference between the two. The Lens shows good transmittance in both the visible and near infrared regions of the spectrum. The liquid-liquid interface can only be kept uniform if the response time is slow (~ tens of seconds). When the transition time is reduced to a few seconds then aberrations become large. The aberrations become worse with greater aperture size. Diameter of the observation hole is 5mm and the diameter of the aperture hole is 4mm. The total thickness of the whole devise is 15mm. ***Figure 11*** shows some photographic results of the mechanical-wetting lens. ***Figure 12*** shows evidence of the lens working in the near infrared.

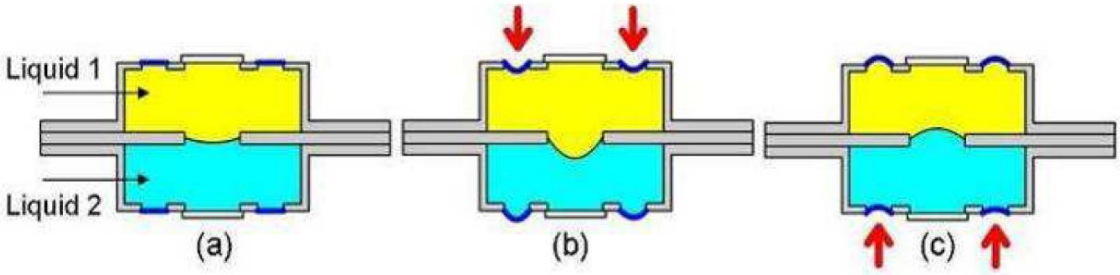

Figure 10 – a) *No change in either chamber volume,* ***b)*** *Diverging lens shape due to compression in oil chamber,* ***c)*** *Converging lens shape due to compression in aqueous solution chamber.*

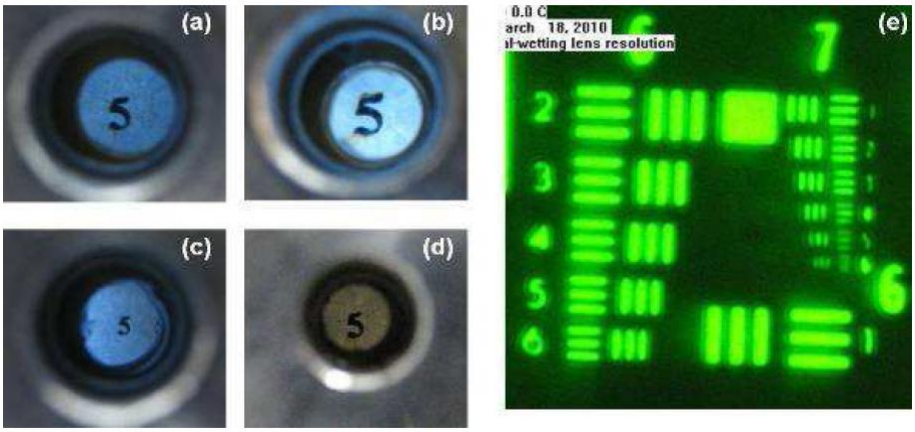

Figure 11 – *Pictures taken with the mechanical-wetting lens in the visible spectrum*

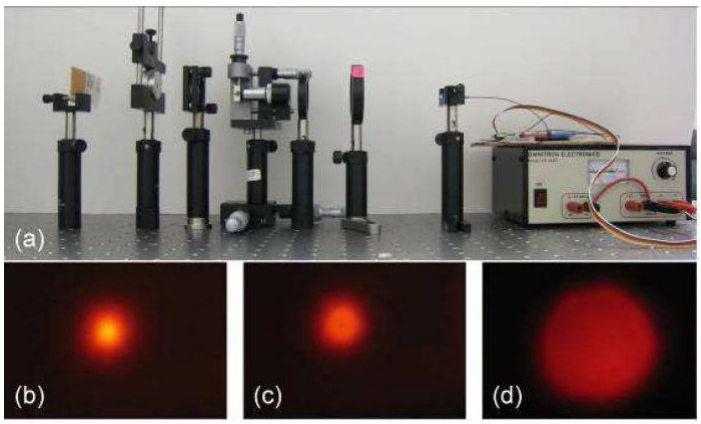

Figure 12 *– Pictures taken with the mechanical-wetting lens in the near infrared*

2.1.4. Available Liquid lens products

- Optotune[14] – Electrically tunable lens. Changes focal length in the range of 15mm-100mm with a response time in the millisecond range. Wavelength range covers the visible to NIR. Diameter of the lens > 5mm, although still relatively small.
  http://www.optotune.com/index.php?option=com_content&task=view&id=18&Itemid=37

- Varioptic[15] ARCTIC 416 – variable liquid lens designed for ¼ inch (5-6mm) optical systems such as mobile phones, PDPAs, barcode readers and webcams. Optical power ranges from -5D to +13D. Designed to transmit in the visible wavelength range (97% transmission at 587nm).
  http://www.varioptic.com/en/products/arctic-416-af.html

- Varioptic Baltic 617 – Variable focus and variable tilt liquid lens. Has an aperture size of up to 2.5mm, Optical power ranges from -5D to +15D, Tilt range ±0.6°, 97% transmission at 587nm. Designed for low light conditions with auto focus and OIS.
  http://www.varioptic.com/en/products/baltic-617-1.html

- Variaoptic Arctic 316 –Designed for 1/4" optical systems such as barcode readers, industrial cameras and medical imaging. Good for low light conditions. Response time <20ms, Focus range from 5cm – infinity. Optical power ranges from -5D to +13D, 97% transmission at 587nm.
  http://www.varioptic.com/en/products/arctic-316-af.html

2.1.5. Summary of Liquid Lenses

Recent developments in liquid lens technology have provided a solution for small diameter lens needs in the visible part of the electromagnetic spectrum. Variable focal lengths have been achieved as well as transitions between positive and negative lenses. Although there is some evidence of this technology working in the near infrared development of liquid lenses to work in the 8-12 microns wavelength range are yet to be touched on. Various ways have been shown to vary focal length with a liquid lens technology however the ability to change the direction or shape of incident wave fronts has not been accomplished. Small apertures have been produced for products such as mobile phone camera lenses but the need for large aperture lenses for high intensity levels cannot be achieved with this technology due to the liquid nature of the lens. Response times in the order of milliseconds have been achieved in various designs. Maintaining the shape of a liquid lens may become a problem when subject to forces in the range of tens of G's, therefore this technology is not going to satisfy the requirements for this project.

2.2 Liquid Crystal Lenses

Liquid Crystal lenses are variable focus lenses that rely on electric or magnetic fields to change the orientation of crystals. By changing the direction the crystals face the refractive index is changed and therefore changes the focal length of the lens.

Shin-Tson Wu and colleagues [16] from the University of Central Florida have designed a new lens that consists of a mixture of liquid-crystal molecules and N-vinylpyrrollidone monomers that are placed between two indium tin oxide coated glass substrates. Without the presence of an applied voltage the mixture is uniform across the gap between the two substrates, however when a voltage is applied the liquid-crystal molecules gather at either end of the gap where the electric field is highest and the monomers group in the middle where the electric field is lowest (***Figure 13***). This distribution of molecules causes a variance in refractive index across the mixture, higher at the ends and lower in the middle, giving the mixture lens like properties. The focal length of the lens has been found to increase with an increase in voltage across the device.

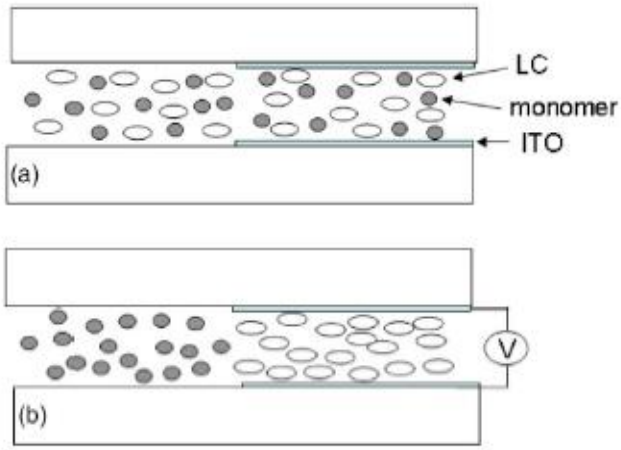

Figure 13– *Distribution of Liquid Crystals and Monomers in Shin-Tson Wu's new Liquid-crystal Lens*

Yi-Pai Huang *et al.*[17] have found that designing a liquid crystal lens system with the electrodes within the liquid crystal layer allows for focal properties to be achieved with much lower applied voltages than in conventional liquid crystal lenses. Conventional LC lenses use solid electrodes that are usually placed outside the substrate wall confining the liquid crystals, however, with the 'Multiple Electrodes Driving Fresnel Liquid Crystal (MeD-Fresnel LC) lens' designed by Yi-Pai Huang et al, the electric field is generated by a series of smaller electrodes placed closely together on the insides of the substrate wall (***Figure 13***). This allowed for lower applied voltages to

achieve the desired electric field and also better focus of the incoming radiation. A He-Ne laser with a wavelength of 632.8nm was used to test the focusing ability of the MeD-Fresnel LC lens. A focal length of 1mm was achieved by applying a 5Volts to the MeD-Fresnel LC lens which is a dramatic cut in needed voltage compared to the conventional MeD-LC lens which required ~30Volts to achieve the same focal length.

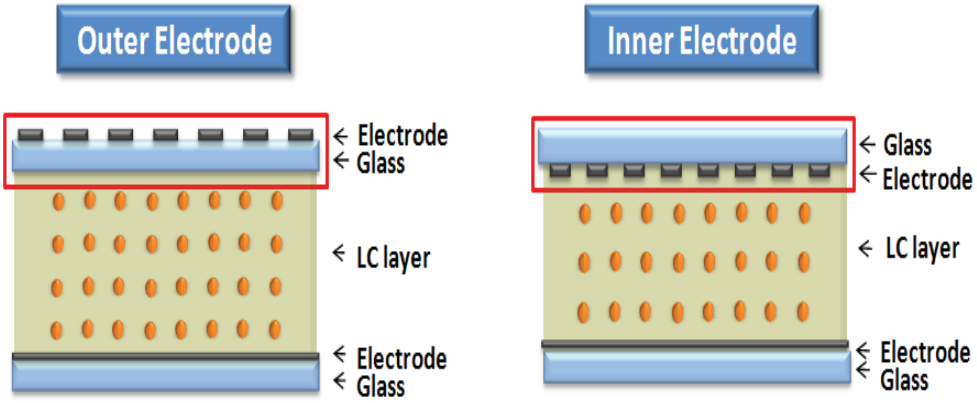

Figure 14 – Structure of the MeD-Fresnel LC lens

Hui Li *et al*. [18] have developed a lens with an electrically tuneable focal length. The lens is a liquid crystal cylindrical lens that consists of two glass substrates coated with indium tin oxide. Electrodes are on the insides of either substrate and are separated from the LC E44 (Merck) liquid crystal layer by two polyimide layers. A spacer at either end of the device keeps the glass substrates separated and gives the space for the liquid crystal layer to be injected in to the device. The author demonstrates a liquid crystal cylindrical micro-lens array in a 128 X 128 rectangular element electrode structure, capable of being tuned with an electric field to cover focal lengths between 60µm and 450µm with a response time of sub-micro-seconds, when the applied voltage ranges from $1.54V_{RMS}$ and $5.0V_{RMS}$.

Bin Wang *et al.* [19] have a similar design also using LC E44 (Merck) liquid crystals. The difference in their design is that they have included a dielectric slab between the liquid crystal layer and the electrode with a circular hole in the middle making it possible for larger apertures. (***Figure15***). Also an extra electrode is added to introduce a new voltage in the drive of the liquid crystal cell. The advantage of having two different driving voltages gives rise to an ability to change the focal length of the lens between positive and negative values. By doing this the direction the liquid crystal molecules face can be manipulated to simulate a convex and concave lens.

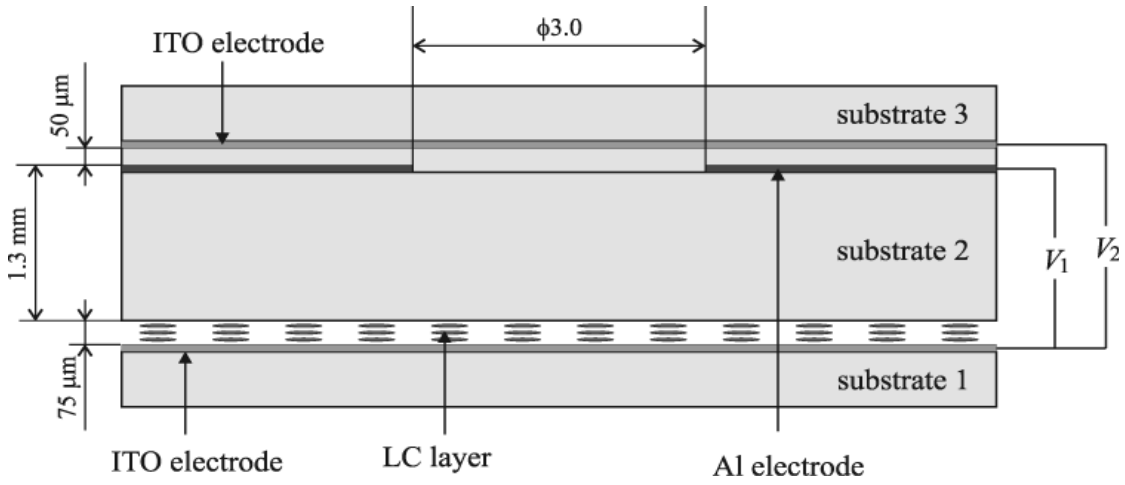

Figure 15 – *Liquid crystal lens cell structure by Hui Li et al*

When voltage V_1 is greater than voltage V_2 the LC layer acts as a converging lens. When V_1 is less than V_2 the LC layer aligns in a manner that acts as a diverging lens (***Figure 16***). Both of these types of lenses have their own advantages as shown in ***Figure 17***, when the light is converged to focus on a point in the focal plane a more intense spot is seen (b). When the LC layer acts as a diverging lens there is a zoom effect on the image which shows more detail however the image is overall less intense due to the separation of the incoming radiation (c).

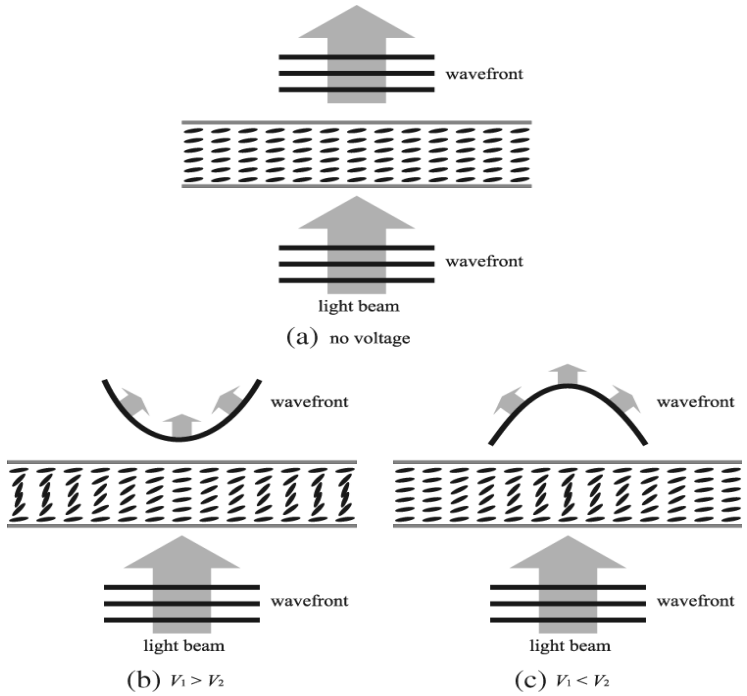

Figure 16 *– Voltage Effects on the incident wave-front*

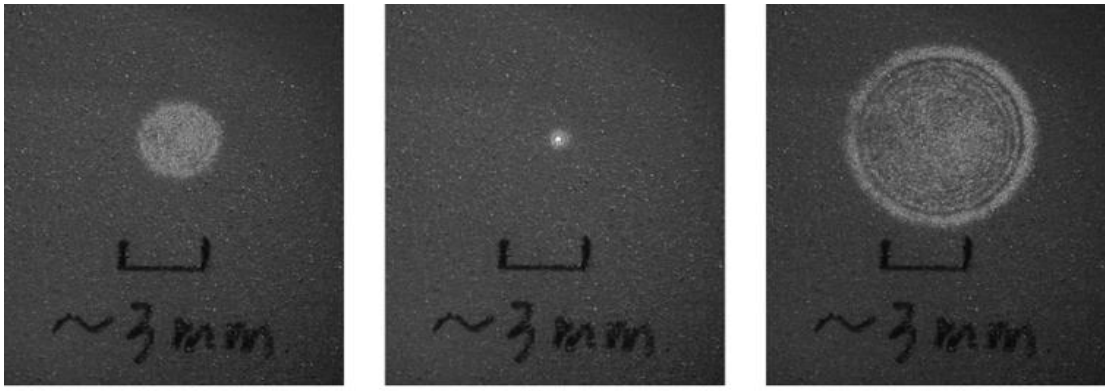

(a) (b) (c)

***Figure 17** – Images formed for different combinations of voltage, (a) $V_1 = 0$ $V_2 = 0$, (b) $V_1 = 35$ V_{RMS} $V_2 = 0$; (c)$V_1 = 0$ $V_2 = 60$ V_{RMS}*

2.2.1 Summary of Liquid Crystal Lenses

LC lenses are currently being developed in the visible light wave band but there are no signs of current development in the infrared. Although one case claims a response time of sub-microseconds the general response time of these liquid crystal systems is in the order of 10 milliseconds. It has been shown that positive and negative focal lengths can be achieved at ranges between (-)0.164m and (+)0.217m. The current TRL of these devices is medium since although products have been designed and fabricated there are not places to buy lenses in this form. This technology does not appear suitable for the project requirements since development in the infrared has not been applied and products are not readily available to consume.

2.3 Beam Steering

Beam steering technology is being developed to provide an alternative approach to Gimbal based systems for scanning and directing laser beams in both the visible and infrared parts of the electromagnetic spectrum. There are many types of beam steering system that provide different characteristics from large field of regard (FOR) to fast response times. The main types of beam steering components are Risley prisms, Decentred lenses and Fast Steering Mirrors (FSM). An outline of current beam steering systems is given in this section.

2.3.1Risley Prisms

Risley prisms consist of two or more prisms back to back. The prisms can be rotated to point the incident beam in the desired direction as shown in ***Figure 18.***

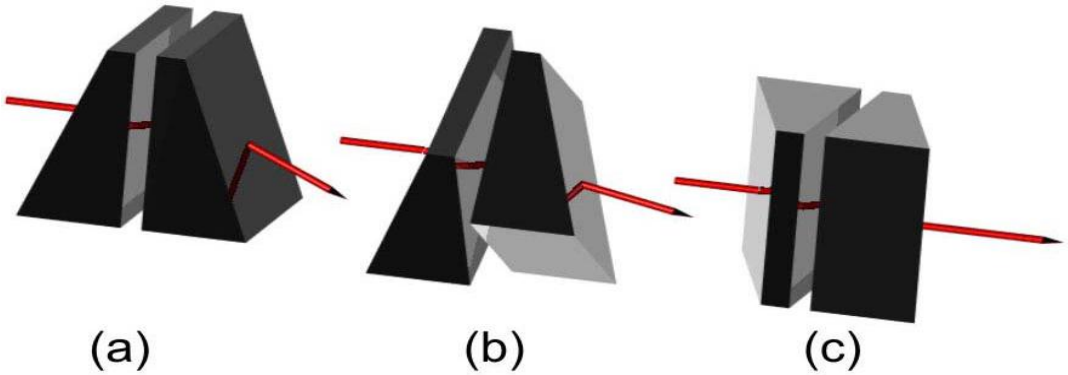

Figure 18 *– Risley Prisms at different angles,* a) *Two upright prisms back to back pointing the incident ray downwards as it exits the system,* b) *Two prisms rotated at equal angles in opposite directions changing the horizontal path of the incident ray,* c) *Two prisms arranged for the incident ray to pass through the system without redirection.*

Optra [20] have developed Risley prism laser beam steering systems for applications in collision avoidance LIDAR, Free-space optical communications and infrared countermeasures. Their infrared countermeasure steering system is designed to work over a wavelength range of 2.0µm-4.7µm, for an incident beam of 3mm diameter. The FOR of the product is 120º with beam divergence less than 1mrad. The size and weight of the system is 2.3 inch by 3.5 inch and 2.3lb respectively (***Figure 19***).

Figure 19 – *Risley Prism Infrared Countermeasure System from Optra*

Bradley D. Duncan *et al.* [21] have also developed a Risley prism beam steering system. The prisms are LiF/Zn doublets in reverse prism geometry (***Figure 20***). The system has been designed to steer radiation in the mid-infrared at angles up to ±45°. Reverse prism geometry is essential to the performance of the system. Advantages of using reverse prism geometry are that the system is fully reciprocal by 180° rotation of one prism, also the reverse geometry allows for full precise steering to zero degrees with no axial blind spots that are present in non-reversed prism geometry. The reverse geometry does have one disadvantage that the dispersion effects are slightly increased by having a sloped leading edge to the system that isn't present in non-reversed geometry, however this effect is small and is considered to be outweighed by the advantage of no present axial blind spots.

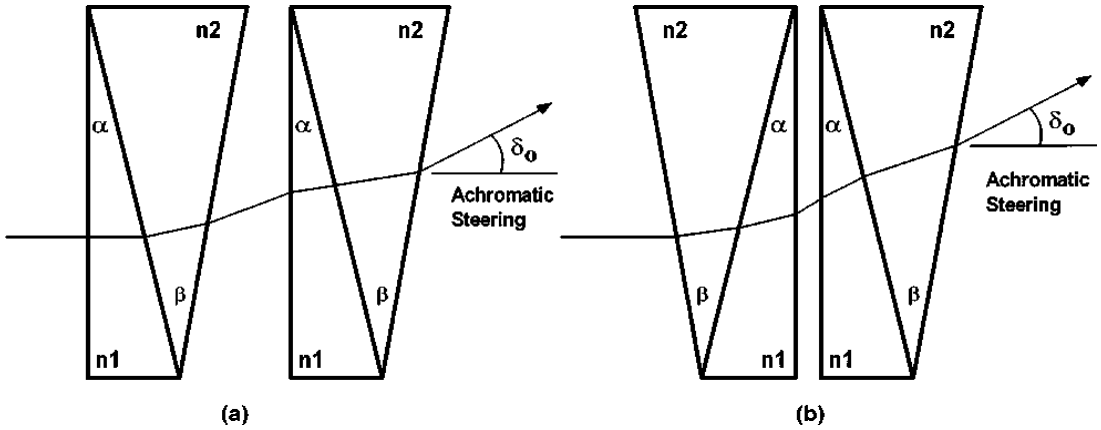

Figure 20 *– a) Non-Reversed Prism Geometry, b) Reversed Prism Geometry*

The beam dispersion of the system designed by Bradley D. Duncan et al is around 1.8mrad.

2.3.2 Risley Gratings

Risley gratings are a technology developed by Chulwoo Oh *et al.* [22]. The system has been designed as a potential replacement for Risley prism systems. The main advantages over prism systems are the size and weight of the product, also there is less beam walk off with theoretically no beam dispersion. The new system comprises of two polarizing gratings that contain rotating liquid crystals creating a FOR of 62º and a transmittance of 89%-92% with incident light from a 1550nm wavelength IR laser, therefore a continuous beam steering of ± 31º. ***Figure 21*** shows the liquid crystal Risley diffraction grating proposed by Chulwoo Oh *et al*. Also in figure 20 is a theoretical picture of some possible scans achievable with this system. ***Figure 22*** shows real images of the achieved scans with the Risley grating system. Circular and linear scans with a FOR of 62º are shown hinting that the system can steer an incident beam to any point within this circular area. Currently the system can be chosen to work over the

visible to mid-infrared wave bands with an 89%-92% throughput. Anti reflection coatings have been applied to the gratings to reduce the reflection values to less than 1% but there are still some losses due to leakage into the side lobes of the system.

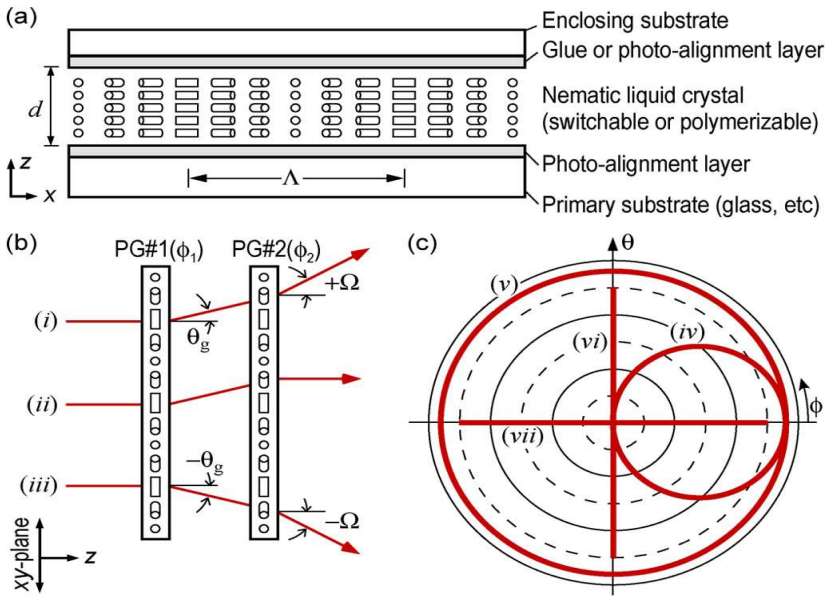

Figure 21 *– The LC Risley diffraction grating.* **A)** *The components of a single grating.* **B)** *Three possibilities of diffracted beams in the z-direction* **c)** *continuous scanning patterns as orientationsare varied* ***(iv)*** *{ø,0º},* ***(v)*** *{ ø+180º, ø},* ***(vi)*** *{ ø -90º, - ø+90º}* ***(vii)*** *{ ø, - ø+180º}*

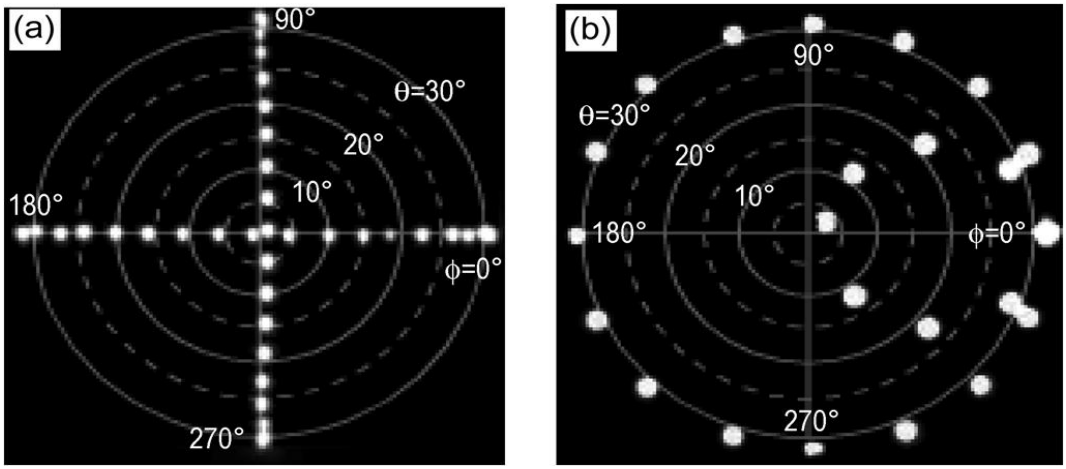

Figure 22 *– Visible results of the LC Risley Grating system* ***a)*** *Linear scans in x and y planes between ± 30º,* ***b)*** *Circular scans within the 62º FOR.*

2.3.3Decentred Lenses

By positioning two lenses off axis to each other light is steered through the lenses at an angle θ to the optical axis (***Figure 23***). Light from the first lens is

converged to the focal point. By positioning the second lens at twice the focal length of the first lens the light is steered and re-collimated. From figure 23 you can see that by positioning the second lens off axis to the first lens some of the light that exits near the edge of the first lens is lost from the system, known as vignetting.

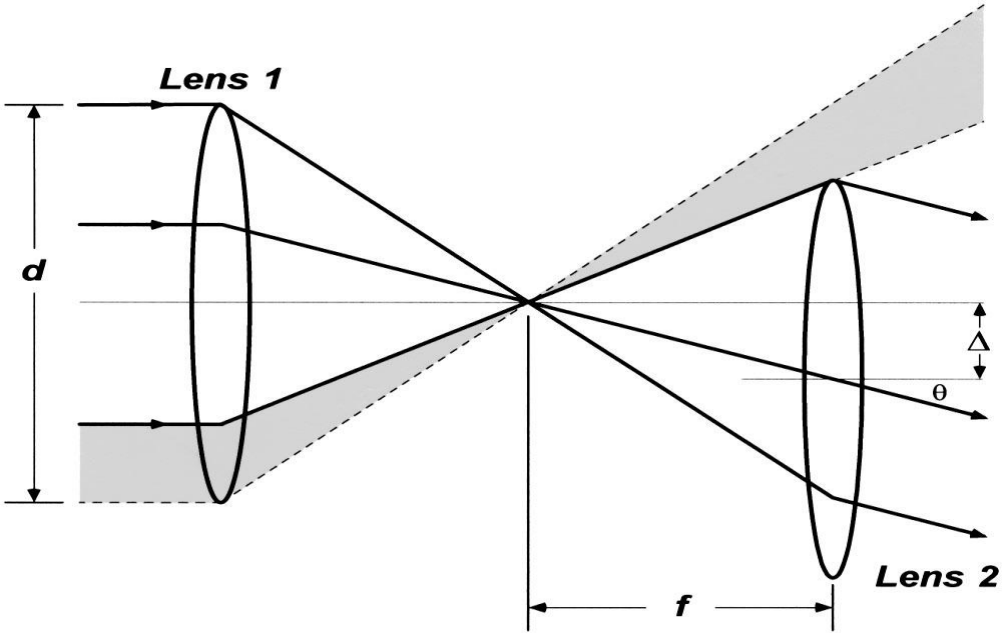

Figure 23 *– Beam steering with two converging lenses off axis to each other.*

Jennifer L. Gibson *et al.* [23] have designed a three lens system comprising of two converging lenses and a diverging lens with the potential to replace lenslet array systems. The advantages of using macroscopic lenses over lens arrays is that the system is free of blind spots, also arrays can create unwanted multiple beam orders and diffraction that are not present in the decentred lens system.

The first lens is used to converge incident parallel light and the final lens is the exit lens of the system that re-collimates the exiting light to maintain the wave-front shape that enters the system. The second lens is a field lens centred off the optical axis of the primary lens that keeps light from the edges of the primary lens in the system. By positioning the entering lens and exit lens on different optical axis the light is steered through the system. A steering angle of 22.5º has been achieved with a system throughput of 63% with an incident wavelength of 5μm. When light of 2μm was incident on the system there was a throughput of 95%. These values fall within a divergence of 1mrad. Spot diagrams of the detected radiation show evidence of a slight coma aberration but did not significantly change the values of beam divergence. The value of 63% throughput at a steering angle of 22.5º was found for a 1 inch diameter incident plane wave and also for a Gaussian beam input with a beam waist of 4.1mm. The amount of energy recorded was within a 1 mrad divergence angle and at a range of

6km since the steering device is intended for a transmitter and receiver. The final set-up is shown in ***Figure 24***. The initial design by Jennifer L. Gibson et al consisted of three converging lenses. The converging field lens was then replaced by a negative field lens to remove any internal foci in the system. With the aid of Code V software, they have made careful decisions on the materials of the lenses to minimize beam divergence in the 2µm-5µm wavelength range **(*Figure 24*)**

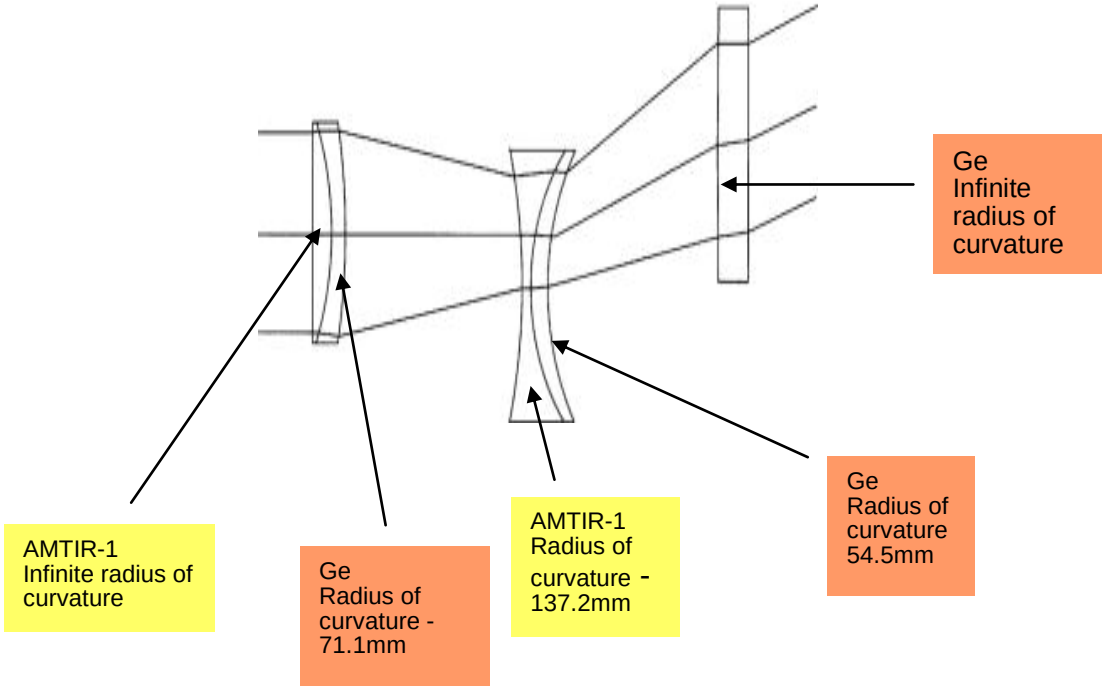

Figure 24 – *Final Modified Decentred Lens system*

2.3.4 Fast Steering Mirrors (FSM)

Qingkun Zhou *et al*. [24] have designed a fast steering mirror system (FSM) for precision laser beams steering. The mirrors in the system are mounted on two piezo-electric actuators that extend and contract to angle the mirror in the desired direction **(*Figure 25*).** To reflect radiation in both x and y planes a system with four actuators would be needed to tilt the mounted mirrors in both planes. To change the direction of an incident beam by the angle θ the mirror must tilt by an angle of θ/2. This is because both the angle of incidence and the angle of reflection will be changed by the angle θ/2. To create a field of regard of 30° the mirrors must be able to tilt by ±7.5° in both x and y planes. In this paper a four quadrant detector is used to sense the incident light. The system is designed to focus the incoming beam onto the centre of the sensor so that light is incident on all four quadrants by a small amount. If the light is shifted due to jitter disturbance then the beam will be steered to one particular quadrant more than the others. This information is then fed back into the system and the actuators move to

compensate for the jitter disturbance, focusing the beam onto the centre of the detector. To produce a precise spot on the centre of the detector a converging focusing lens is placed one focal length from the sensor. The systems designed with two FSMs have two detectors which feed back to the respective mirror system (***Figure 26***). Beam splitters are also included in the system which reflect most of the light but allow a small percentage of the energy to pass through. This transmitted energy is focused on the detector by a focusing lens, which eliminates any angular error.

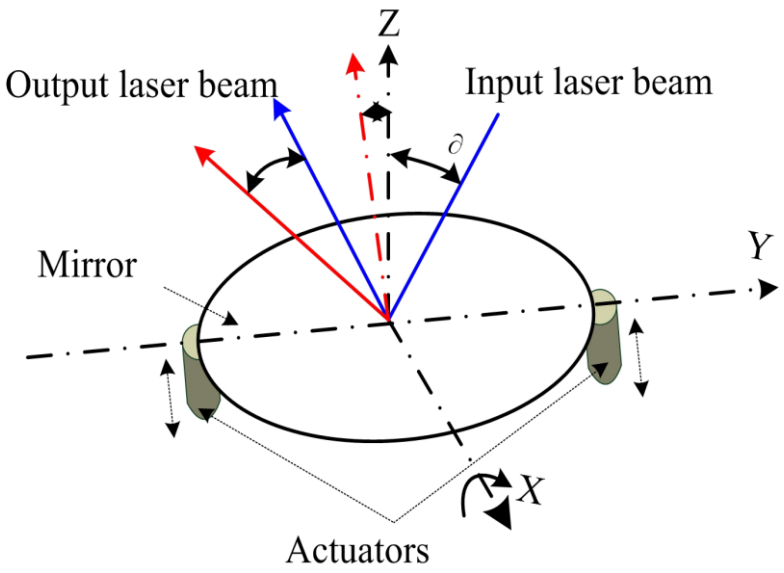

Fig 25 *– Fast steering mirror controlled by two actuators*

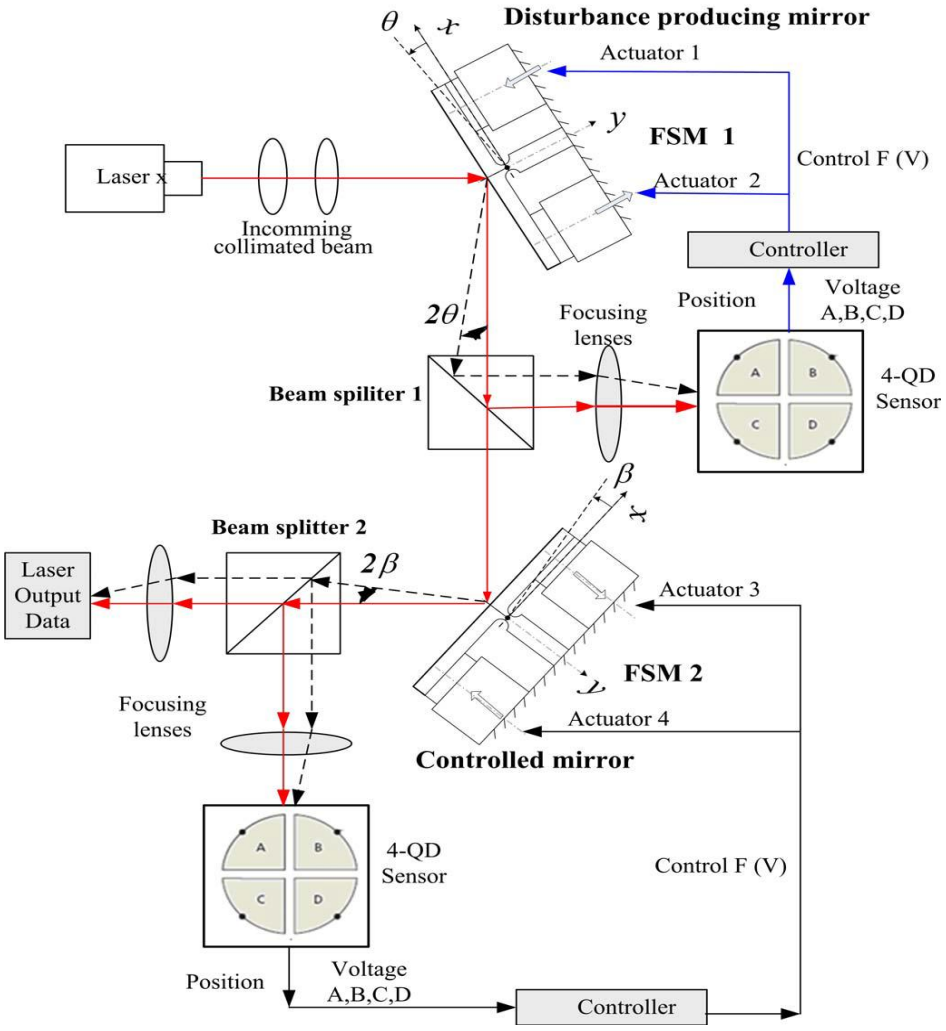

Figure 26 *– Two FSMs beam steering system*

One advantage of mirror beam steering systems is the option of smaller length systems. This is because the optical path can be doubled back on itself. Small dispersion levels are also possible with mirror systems as reflection coatings can be made very thin. Another advantage is the possibilities for beam splitting surfaces so that detectors can be added to the system to determine the need for movement at each individual reflecting surface.

2.3.5 Currently Available FSM systems

FSM systems are currently available to buy from various places. Two suppliers are shown below with their system specifications.

http://www.newport.com/ [25]

- offer a range of FSM's and controllers.

- Angular range - ±3°

- Angular resolution - ≤2μrad rms

- Loop control to 800Hz

- Replaceable 1 inch mirrors

Figure 27 *– Fast steering mirror and controller from Newport*

Typical Specifications

Mirror Assembly	FSM-300-01
Number of Axes	2 (tip-tilt)
Angular Range from ±10 V	±26.2 mrad (±1.5°), Mechanical(1)
Resolution	≤1 µrad rms, Mechanical(1)
Repeatability	≤3 µrad rms, Mechanical(1)
Accuracy from ±26.2 mrad, 25°C(1)	≤0.262 mrad (0.015°), Mechanical(1)
Linearity from ±26.2 mrad, 25°C(1)	≤1.0%
Closed-Loop Amplitude Bandwidth for small signal inputs (-3 dB)	600 Hz at 10 mV (typical)
Closed-Loop Phase Bandwidth (60° lag)	250 Hz (typical)
Response Flatness(2)	Peaking ≤3 dB
Noise Equivalent Angle	≤3 µrad rms
Resolution of Local Position Sensor	≤0.5 µrad
Operating Temperature Range	0 to 50°C (32 to 122°F)
Storage Temperature Range	-20 to 55°C (-4 to 131°F)
Sensor Warm-up Time for Mirror Stability at 25°C	≤10 minutes
Mass	1lb (0.45 kg)
Interconnect Cable Length	9.8 ft (3 m)
Dialectric Mirror Substrate Material	Pyrex
Mirror Retaining Mechanism	Mirror bonded to aluminum carrier, field replaceable
Pivot Point of Axes (centered on mirror)	12.19 mm behind mirror surface
Mirror Diameter	25.4 mm
Mirror Thickness	6.0 mm
Mirror Wedge	≤5 arc min
Clear Aperture (at 0° angle of incidence)	≥20.3 mm
Clear Aperture (at 45° angle of incidence)	≥14.4 mm
Reflectivity(2)	Enhanced Aluminum: >93%, 450-700 nm Protected Gold: >96%, 650-1700 nm; >98%, 1.7-2.0 µm
Surface Flatness(2) (after coating and bonding)	≤λ/8 at 632.8 nm over clear aperture
Surface Quality(2)	15-5 scratch-dig

Figure 28 *– FSM specification table from Newport*

http://www.physikinstrumente.com/en/index.php [26]

- Angular range – up to ± 50 mrad tilt range

- Angular resolution – sub-µrad resolution

- Response time – sub-milliseconds

Technical Data

Model	S-334.1SL S-334.1SD	S-334.2SL S-334.2SD	Units	Tolerance
Active Axes	θ_X, θ_X	θ_X, θ_Y		
Motion and positioning				
Integrated sensor	SGS	SGS		
*Open-loop tilt angle at -20 to +120 V	30	60	mrad	min. (+20%/-0%)
*Closed-loop tilt angle	25	50	mrad	
Open-loop resolution	0.2	0.5	µrad	typ.
Closed-loop resolution	1	5	µrad	typ.
Linearity	0.05	0.05	%	typ.
Repeatability	2	5	µrad	typ.
Mechanical properties				
Resonant frequency underload (with standard mirrors)	3.0	1.0	kHz	±20%
Load capacity	0.2	0.2	N	Max.
Distance of pivot point to platform surface	6	6	mm	±1 mm
Platform moment of inertia	1530	1530	g • mm²	±20%
Standard mirror (mounted)	diameter: 10 mm, thickness: 2 mm; BK7, λ/5, R > 98% (λ = 500 nm to 2 µm)	diameter: 10 mm, thickness: 2 mm; BK7, λ/5, R > 98% (λ = 500 nm to 2 µm)		
Drive properties				
Ceramic type	PICMA® P-885	PICMA® P-885		
Electrical capacitance per axis	3	3	µF	±20%
Miscellaneous				
Operating temperature range	-20 to 80	-20 to 80	°C	
Material casing	Titanium	Titanium		
Mass	0.065	0.065	kg	±5%
Cable length	2	2	m	±10 mm
Sensor / voltage connection	LEMO connector / 25-pin sub-D connector	LEMO connector / 25-pin sub-D connector		

Figure 29 – *FSM specification table from PI*

Figure 30 *– Fast steering mirror from PI*

2.3.6 Infrared Mirror Coatings

Infrared mirror coatings are available from various companies. Below are a few resources and the products that they offer.

[27] http://www.lbp.co.uk/Coatings/Gold.html – Gold coated copper mirrors for high reflectivity in the infra red and good reflectivity in visible spectrum. Electroplated coating that doesn't peel, flake or delaminate. 97%-99% reflection over 0.7 to >12.5 μm range.

[28] http://www.evaporatedcoatings.com/dielectric-mirror-infrared-optical-materials.html - Silicon, Germanium, Zinc Selenide, Zinc Sulfide, CaF_2, BaF_2, Gallium Arsenide, Sapphire, IR Fused Silica and other IR coatings that give reflection values typically > 99%.

[29] http://www.reynardcorp.com/infrared_technology.php – Work with many different infrared materials. Alon , Amtir 1, 2 & 3 , Barium Flouride (BaF2) , Borosilicate Crown Glass (BK-7), Calcium Fluoride (CaF2), Cleartran (multi-spectral), Fused Silica (SiO2), Gallium Arsenide (GaAs), Germanium (GE), Indium Arsenide (InAs), Magnesium Fluoride (MgF2), Mercury Cadmium Telluride (MCT), Sapphire (Al203), Silicon (Si), Thanllium Bromo-lodide (KRS5), Zinc Selenide (ZnSe), Zinc Sulfide (ZnS).

Protective Gold Coating: The bare gold coating is a broadband high reflector in the near infrared (NIR) and far infrared (FIR). It has an average reflection of over 98% in the infrared.

2.3.7 Beam Splitters

Beam splitters reflect a portion of the incident radiation, absorb a portion of the incident radiation and transmit a portion of the incident radiation, resulting in multiple beams present in a system. Used in Interferometry to determine wavelengths and other features of visible radiation. Also used in FSM systems to determine position of a beam at a particular point in the device.

[30] http://www.thorlabs.com/NewGroupPage9.cfm?ObjectGroup_ID=4805 – ZnSe Broadband Plate Beamsplitters (7 – 14 µm range).Beamsplitter Coating on Front Surface: 7 – 14 µm, AR Coating on Back Surface: 7 – 14µm, Optimized for 50:50 Beamsplitting.

[31] http://www.edmundoptics.com/onlinecatalog/displayproduct.cfm?productid=3035 - ZnSe Plate Beamsplitter, (7 – 14 µm range). Designed for a 45° angle of incidence. Reflection values vary between 40% - 60% over the wavelength range.

2.3.8 Summary of Beam Steering

Various beam steering products are of high TRL and can be purchased from different websites.

Risley prisms have the potential for large steering angles and quick response times dependent on the type of actuation used to move them. Although large FOR values have been achieved and the ability to function in the mid wave infrared (MWIR), the beam divergence may be too large for the requirements of this project.

Risley gratings have the advantage of being slim and light. Also large apertures are possible. The system can be designed to work over the visible spectrum and also up to the MWIR. Circular and linear scans have been achieved over a FOR of 62°, however the response time of the liquid crystal layer of the gratings are too slow to satisfy the project needs. Also although a product has been fabricated, the TRL is only medium as the system is more of a laboratory project than an available product.

Decentred lenses have the ability to steer MWIR radiation through angles of up to ±22.5°, and with careful consideration to materials shows promise to work in the long wave infrared (LWIR) part of the spectrum. Low values of beam divergence have been made possible with doublet lens designs and speeds of response are dependent on the type of actuation. These systems are promising and could be considered to implement in to this project.

Fast steering mirror (FSM) systems also show good qualities relative to the requirements of this project. With the ability to apply thin reflection coatings to mirror faces the dispersion values are kept minimal. Steering angles and speeds are determined by the actuators used . The ability to add beam splitters to the device gives the

advantage of being able to determine the need to move each reflecting component individually. These systems show the potential to be used to scan the projects required FOR.

2.4 Micro Electro-Mechanical Systems (MEMS)

MEMS technology is the combination of mechanical functions and electrical functions on the same chip using micro-fabrication technologies. Most MEMS are based on Silicon or glass wafers. Some examples of MEMS devices are accelerometers for airbag deployment, digital mirrors, and pressure sensors. A lot of attention has been paid to developing MEMS based micro-mirror systems in recent years. There are a few differences in current system designs mainly involving actuator types. The main types of actuation are Electrostatic and Electro-thermal. In this section the current state of the art MEMS micro-mirror technologies are outlined.

2.4.1 Electro-Thermal Based MEMS Micro-Mirrors

Lei Wu *et al.* [32] have designed a large aperture scanning MEMS micro-mirror for free-space optical communications. With aperture sizes up to 10mm the divergence angles are around 0.5mrad. Voltages as low as 7V can be used to drive the device to scan angles greater than 10° (***Figure 31***) and also move the mirror in the z direction as well as tilting in the x and y planes (***Figure 32***). The response time of the device is around 30ms, and a collimating lens is needed to compensate for the curvature of the mirror, which has a radius of curvature of 0.7m.

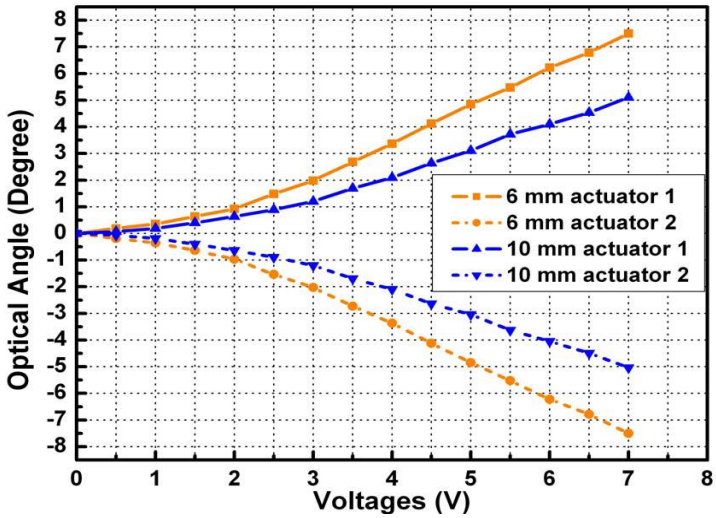

Figure 31– *Graph to show the variation of optical angle of the Lei Wu et al Rapid Scanning MEMS Micromirror with varying voltage.*

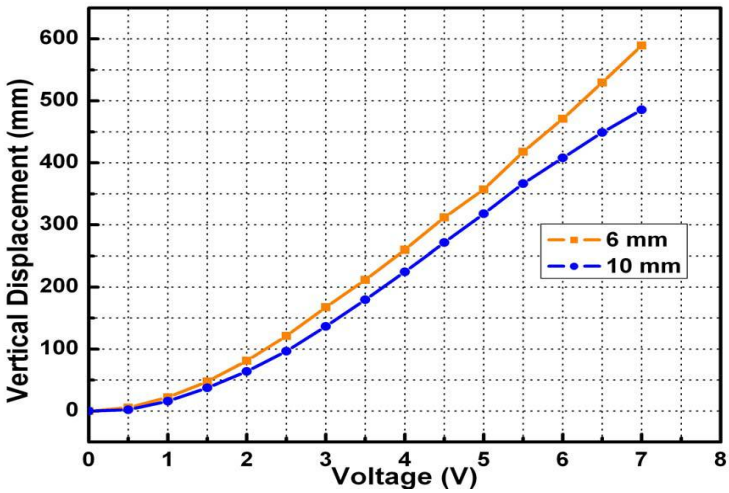

Figure 32 – *Graph to show the variation of vertical displacement of the Lei Wu et al Rapid Scanning MEMS Micro-mirror with varying voltage.*

This system uses bimorph actuators to control the x and y plane tilt, and the z plane displacement. Bimorph actuators are rods of two materials with different thermal expansion coefficients (TEC). When the temperature of the device is changed the two materials expand and contract at different rates giving rise to bends in the rods. This allows for the possibilities of the steering angles and mirror displacements shown. ***Figure 33*** shows the electro-thermal bimorph design used in this particular system.

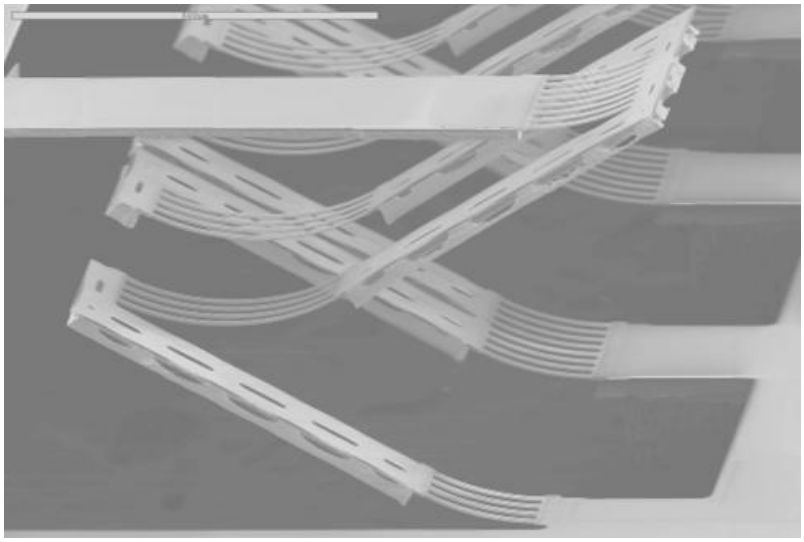

Figure 33 – *Bimorph Actuators in the Lei Wu et al Rapid Scanning MEMS Micromirror.*

Huikai Xie [33] has shown various single-crystal silicon based, large-aperture-size MEMS mirrors based on electrothermal bimorph actuation. Scanning MEMS mirror systems in 1D and 2D have been shown. Scan angles of over 100° in one dimension are achieved at low voltages **(*Figure 34*),** however this is achieved by mounting a mirror on the end of one bimorph length, which also gives large translational movement of the mirror at the same time as rotational scanning **(*Figure 35*).**

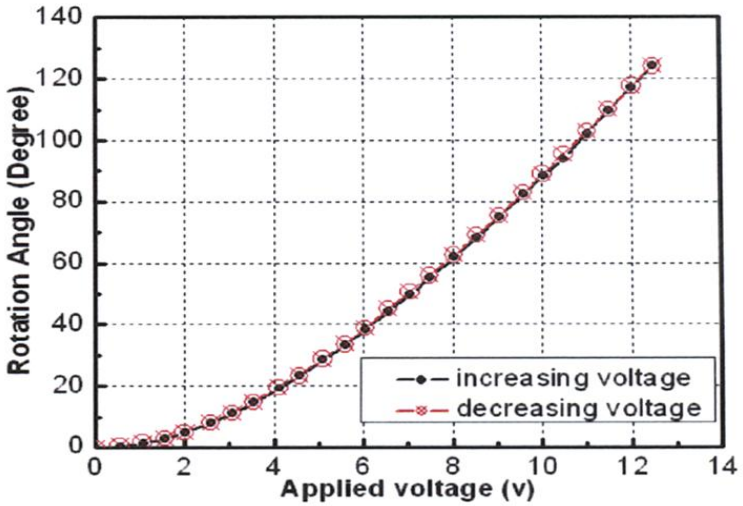

***Figure 34** – Graph to show the variation of rotation angle with varied applied voltage in the one-dimensional MEMS micromirror system.*

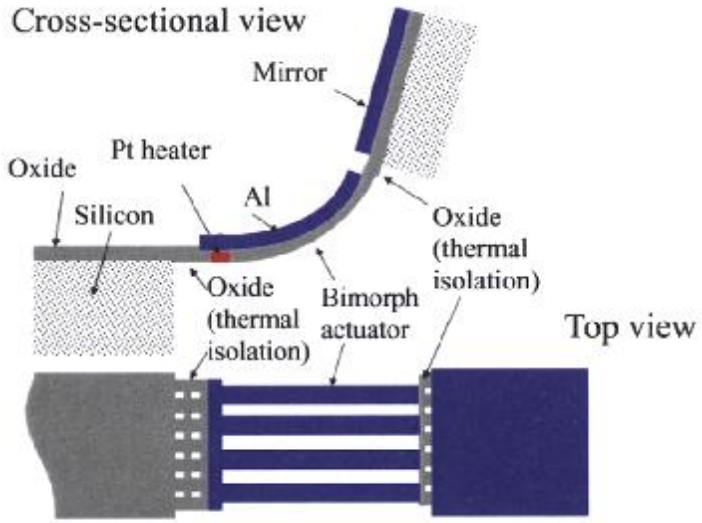

***Figure 35** – Cross-sectional and top views of the one-dimensional MEMS micro-mirror system*

The mirror plate in the system is 1mm by 1mm. A 0.141mm piston stroke and 12° of 2D non-resonant optical scan range is achieved. This Electro-thermal Bimorph system consists of two material layers, one with a higher thermal expansion coefficient than the other, so that when a voltage is applied, the systems heats up and the bimorph beam bends. Typically the high TEC materials are a metal such as aluminium, and the low TEC material is a dielectric such as SiO_2. In the one-dimensional scanning system the mirror is attached to the end of the bimorph beam and scans through the field of regard as the beam bends. To allow for piston stroke without any lateral shift a design has been made with two 'S' shaped bimorph actuators doubled back on each other (ISC Bimorph) so that each of the beams lateral shifts cancel each other out (***Figure 36***). Two sets of these actuators are fitted to all four sides of the mirror plate (***Figure 37***). By applying different voltages to the actuators on the different sides the tip and tilt operations can be achieved as seen in ***Figure 34***. These mirror systems have been applied to medical imaging such as OCT and nonlinear optical imaging for early cancer detection. With the correct mirror coatings and large enough apertures they could potentially be used for beam steering in IR countermeasure systems.

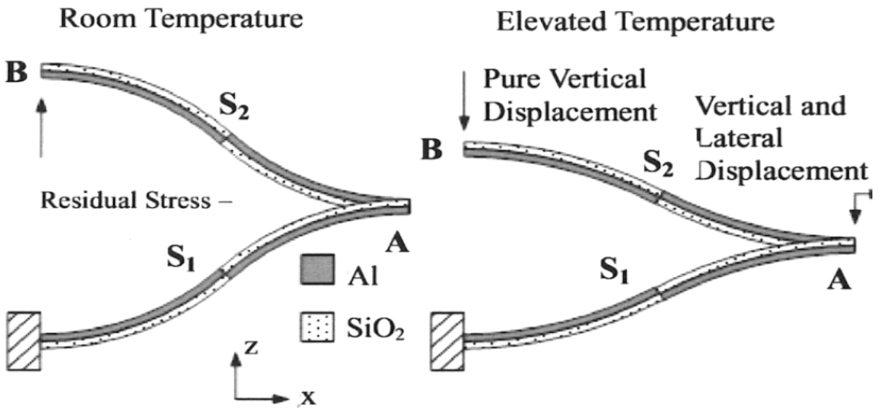

Figure 36 - *Four bimorph actuators forming opposing 's' shapes to limit lateral shift.*

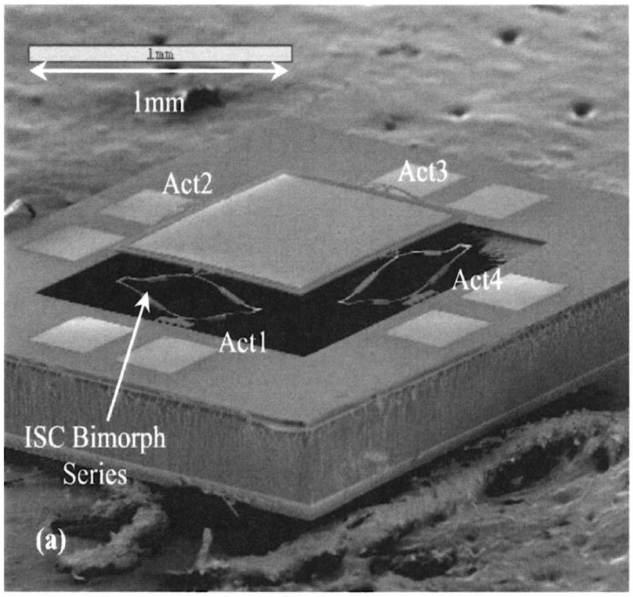

Figure 37 – Final ISC Bimorph two-dimensional MEMS micromirror system

Kemiao Jia *et al. [34]* have also developed an electrothermal Tip-Tilt-Piston Micromirror based on folded dual s-shaped bimorphs that counteract lateral shift. The bimorphs consist of an Aluminium layer that runs the whole distance of the bimorph arm, and two sections of SiO_2 that overlap to give strength to the system (***Figure 38***). A Pt heater is buried between the Al and SiO_2 layers. It is a resistor that when current is passed through heats up and changes the physical shape of the bimorph arms.

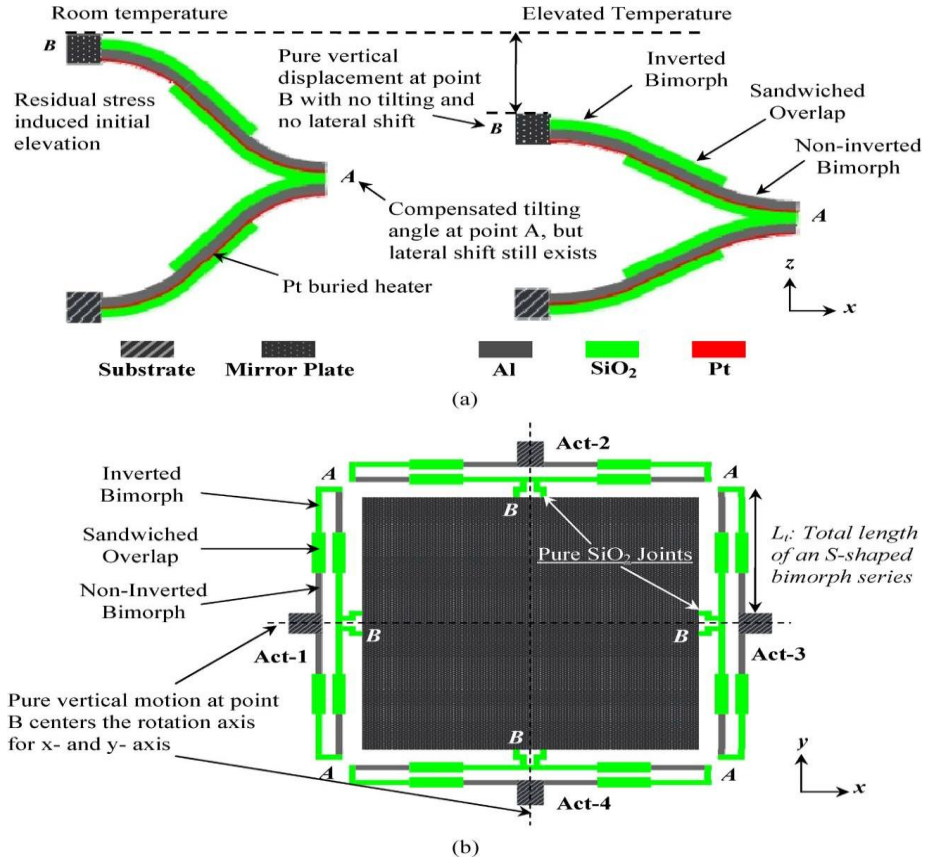

Figure 38 – a) *Structure of the individual folded dual 'S' shaped bimorph actuator,* ***b)*** *Top view of the mirror and placements of the actuators*

With four 'S' shaped bimorph arms attached to each side of the square mirror the mirror can be tilted in x and y planes, and also have translational motion in the z direction. At room temperature the bimorph arms are extended and the mirror plate is elevated 528.6μm above the Silicon substrate. Increasing the voltage in the bimorph arms at the same rate causes the mirror to move towards the Silicon wafer substrate. At 450K the mirror plate moves down by 265.3μm. To obtain tip-tilt effects the voltages applied through the different sets of actuators must be different, causing a differential temperature change to one of the two opposing actuators. With one opposing pair of actuators both set at 450K, while the other pair are set at 300K and 600K, respectively, a mirror tilt of 12.1° is obtained. The mirror can be mounted on the actuators either way so that it is either above or below the Silicon substrate as shown in ***Figure 39***. Graphs showing the variation in z-plane height and x and y plane rotation are shown in ***Figure 40*** and ***Figure 41*** respectively. ***Figure 42*** shows some scans achieved with this MEMS system.

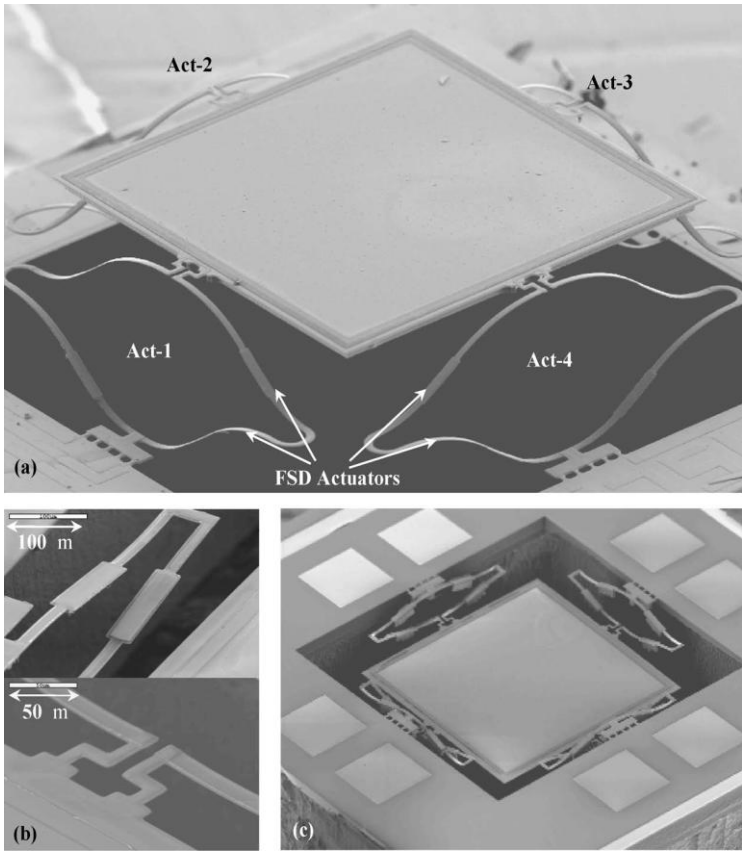

Figure 39 – a) *MEMS micro-mirror system mounted above the substrate base,* ***b)*** *Bimorph actuators,* ***c)*** *MEMS micro-mirror system mounted below the substrate base.*

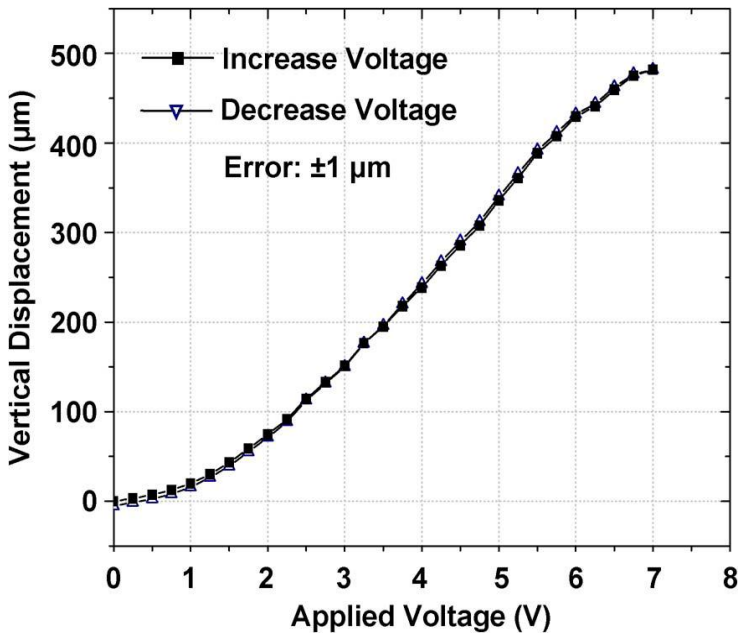

Figure 40 – *Graph to show the variation in vertical displacement with varying applied voltage*

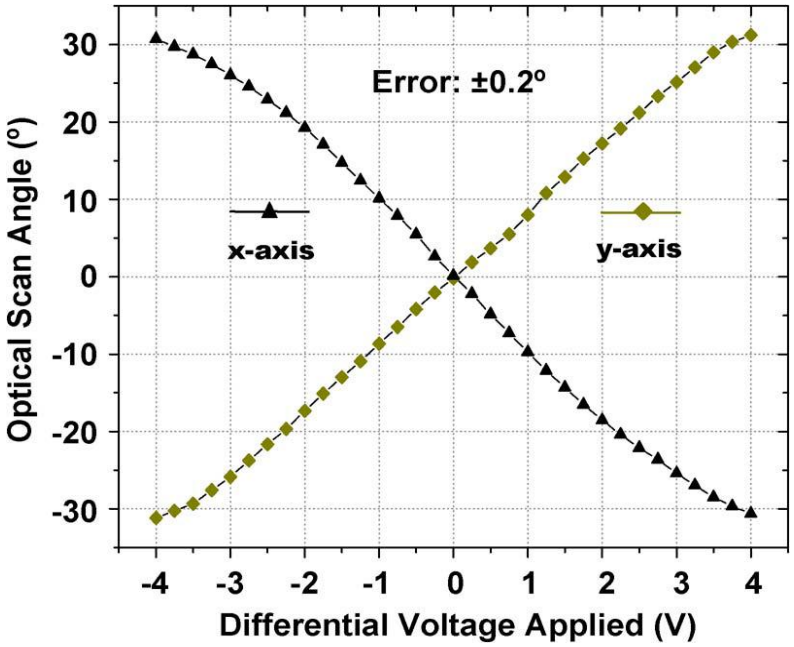

Figure 41– *Variation in optical scan angle with varying differential applied voltage*

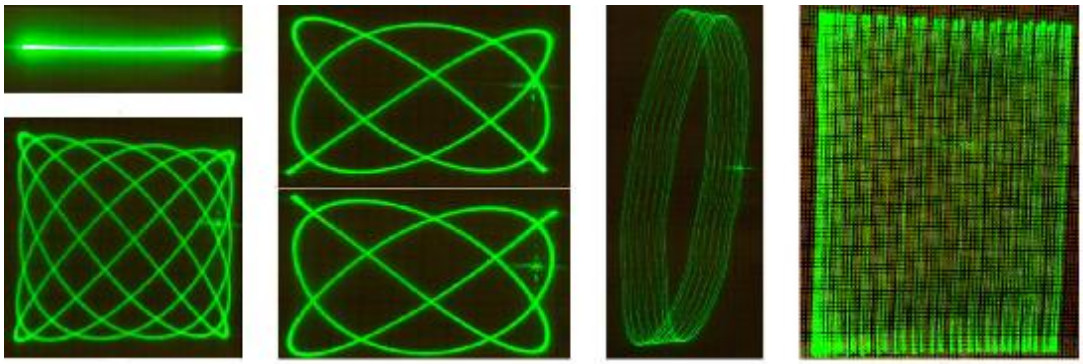

Figure 42 – *Some scans achieved with the electro-thermal tip-tilt-piston micro mirror from Kemiao Jia et al*

In conclusion this tip-tilt-piston mirror has a 1mm x 1mm aperture, can achieve a maximum of 480μm piston stroke, ±30° field of regard in 2D, and all at about 8V dc. The response time of the device is relatively slow at around 10ms.

L.Wu *et al. [35]* have also developed a piston-tip-tilt micromirror based on electrothermal bimorph actuation. They have designed actuators using three bimorph beams attached to each edge of a square mirror. The bimorph beams have solid frame sections separating them as shown in ***Figure 43*****.** A four by four optical phase array has been made from these MEMS micro mirrors (***Figure 44*****).** Scans of up to ±34° both x

and y planes have been achieved with only 4.3Vdc. Piston displacement of 215μm has been achieved at 4Vdc. The response time of the device is about 25ms.

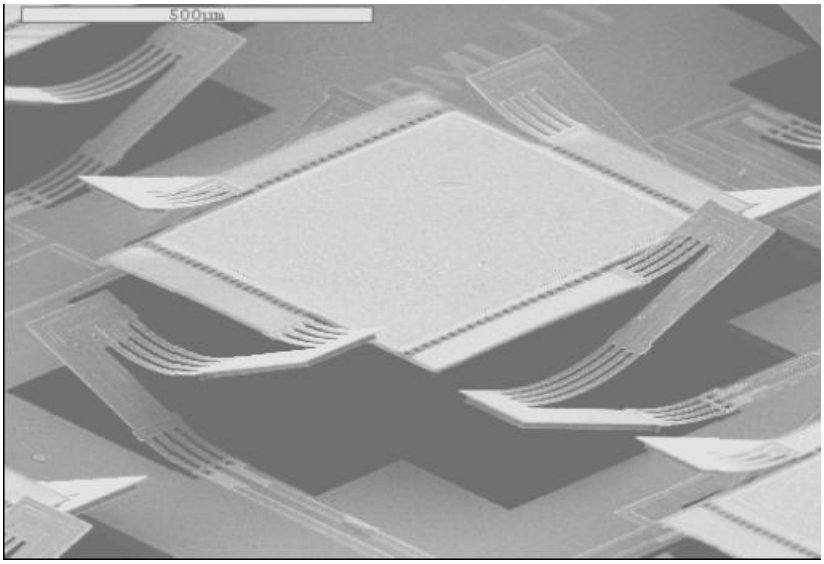

Figure 43 *– MEMS micro-mirror with three bimorph actuators on each mirror edge*

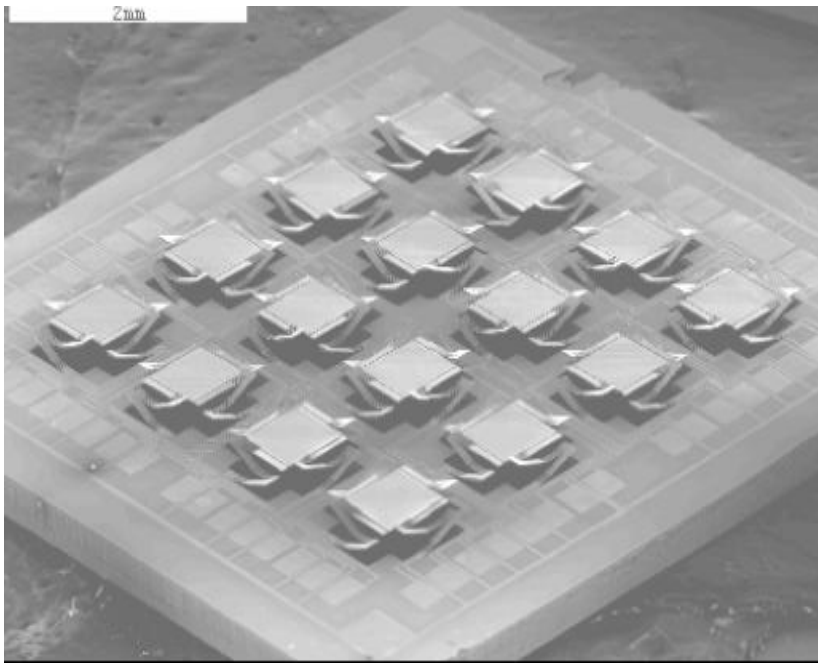

Figure 44 *– 4 X 4 Array of MEMS micro-mirrors*

2.4.2 Electrostatic Based MEMS Micro-Mirrors

Lixia Zhou *et al. [36]* have developed an SOI/SOI wafer-bonding process to fabricate scanning mirrors actuated by lateral comb drive actuators. Their fabricated one-axis micro mirror with rectangular cross section torsional beams (***Figure 45***) can scan up to 21.8° under a dc actuation voltage of 75.0V.

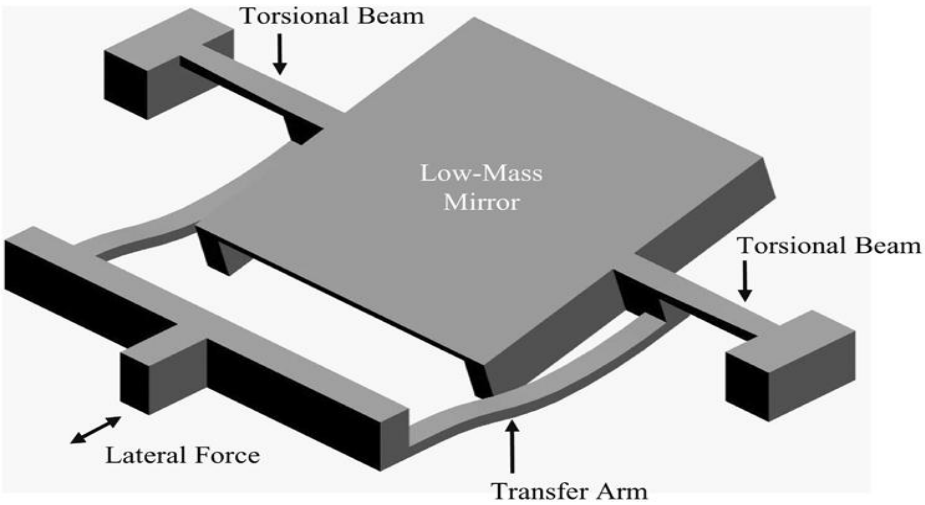

***Figure 45** – Low mass mirror with one-dimensional tilt on rectangular cross-section torsional beams*

The mirror has a rotational mode at 3.6kHz, an out of plane lateral mode at 4.1kHz and a left to right twisting mode at 6.8kHz. Their fabricated two-axis micro-mirror scans up to 15.9° under actuation voltage 71.8V around the inner axis and 13.2° under actuation voltage 71.2V around the outer axis. The inner and outer axis rotational mode resonant frequencies are 2.2kHz and 1.3kHz respectively. The rectangular torsion bars in the 1D scanner have been replaced by T-bar torsional beams in the 2D scanner. The end two-axis scanner is a gimballed scanner (***Figure 46***) and so it would not be useful for our requirements.

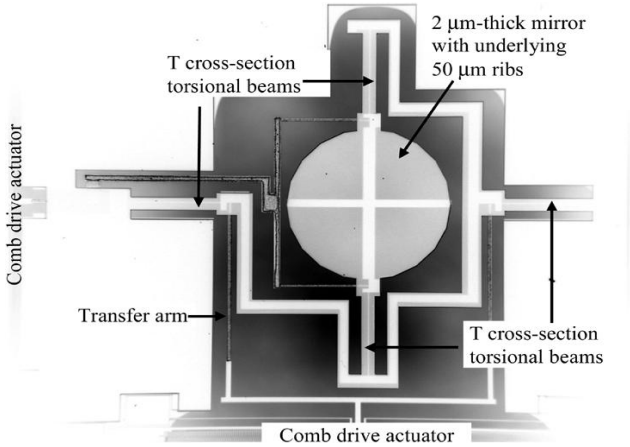

Figure 46 – *Two-dimensional gimballed mirror tilt system*

Hongjun Zeng *et al.* [37] have developed a Tilting Micro-mirror with a liquid-metal pivot. The design consists of a LMD (liquid-metal drop) held between two substrates. There is one electrode directly underneath the LMD and one on either side of the LMD **(*Figure 47*).** A pyramid design is also discussed as shown in ***Figure 47*** but has not yet been implemented. When a voltage is applied between electrode 1 and 3 the micro-mirror rotates clockwise about the Mercury pivot drop, when a voltage is applied between electrodes 1 and 2 the micro-mirror rotates counter clockwise about the Mercury pivot drop.

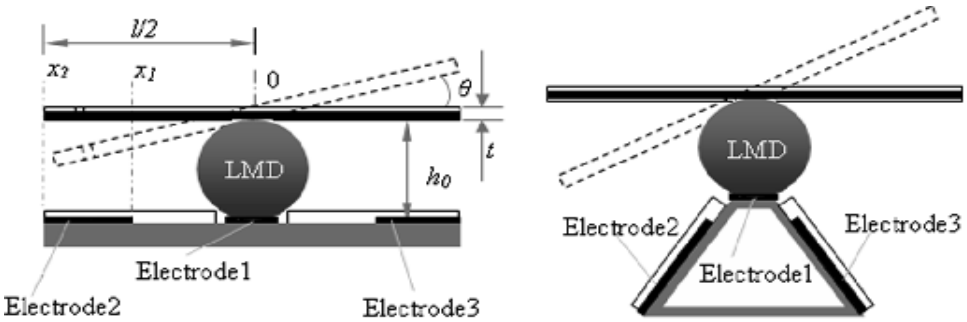

Figure 47 – Tilting micromirror utilizing a liquid-metal Mercury drop

The method for creating the mirror and the electrodes are shown in ***Figure 48.***

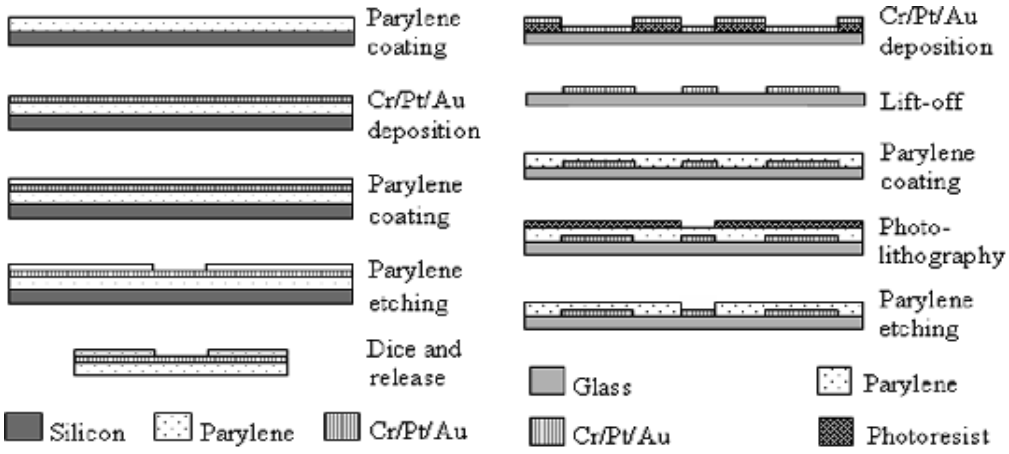

Figure 48 – *Methods for creating the mirror base and electrodes in the LMD mirror tilting system*

The micro mirror systems are able to scan through angles smoothly to around 2.5° with applied voltages up to around 79V. Once the voltage applied is increased to over 79 ± 4V the mirror snaps to an angle of 11.2°, resting against the bottom substrate. The voltage then needs to drop below 40V for the mirror to start to return to its original position parallel to the bottom substrate. This is shown in ***Figure 49***. This system has the potential to be used as a digital micro mirror and in optical switching. This particular MEMS system has the ability to withstand shaking with accelerations of up to 56g. This system can only be used to beam steer in one dimension, however advancements are being made to make it work in 2 dimensions.

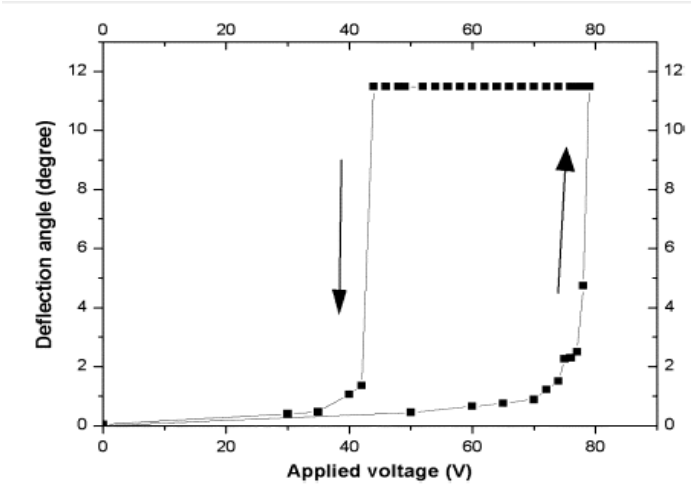

Figure 49 – *The variation of deflection angle of the LMD mirror tilting system with varying applied voltage*

Flavio Pardo *et al.* [38] have developed a tip-tilt-piston mirror based on four dual in-plane comb drives. A horizontal tilt of 4.3°, diagonal tilt of 3.5° and a piston displacement of 5.4μm has been achieved all under an applied voltage of 110V. The response time of the horizontal tilt is currently 20μs, and the response time of the piston displacement is under 10μs. The design consists of four in-plane comb drives, each attached to an arm that rotates out of plane (***Figure 50***). A flexible joint at the end of each arm is attached to the mirror, allowing 3 independent degrees of freedom, tip, tilt, and upward piston movement.

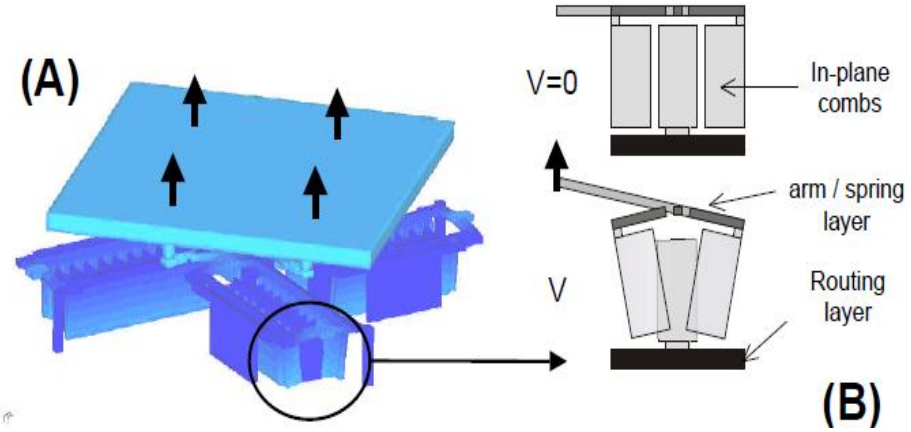

Figure 50 *– **a)** Electrostatic comb drive MEMS micro-mirror, **b)** Mirror tilt with applied voltage*

Veljko Milanovic *et al.* [39] have also designed an electrostatic comb drive micro-mirror system in a 2 X 2 array. The mirror has three degrees of freedom also, tip,tilt and piston motions. Slightly larger tip-tilt angles have been achieved at up to ±5°. A piston displacement of ±12μm has been realised. The overall fill factor is 95% chosen so that each mirror has sufficient space to move without interacting with neighbouring mirrors. The lowest resonant frequencies for rotation modes are >440Hz, while for piston motion the lowest resonant frequencies are >1520Hz. In this design each mirror can be individually controlled to achieve various scans. ***Figure 51, Figure 52*** and ***Figure 53*** show the setup of the 2 X 2 array, including an optical micrograph of the arrays tip-tilt-piston actuators.

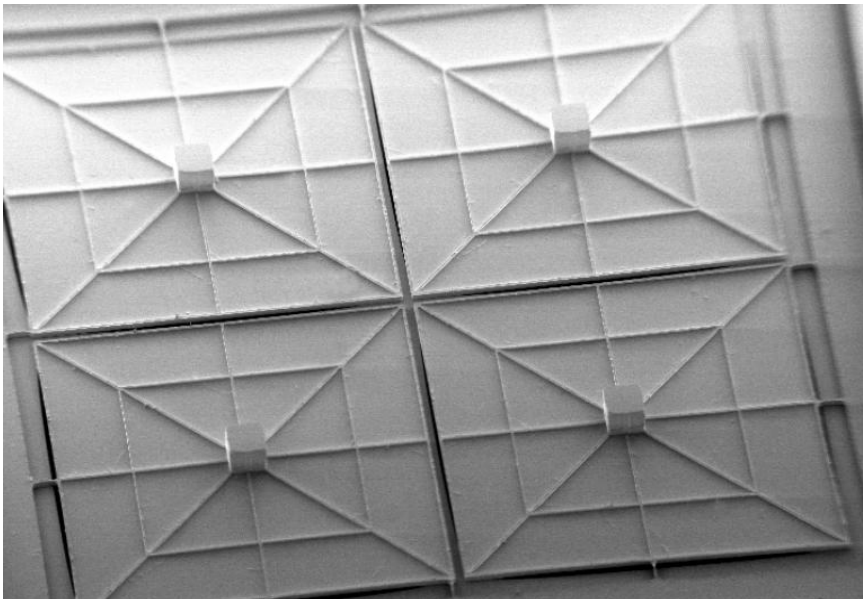

Figure 51 *– SEM micrograph of the backside of a 2x2 array of low-inertia silicon micro-mirrors; both sides of the mirrors are metalized; mirrors are ready for transfer/bonding into a 2x2 array of actuators*

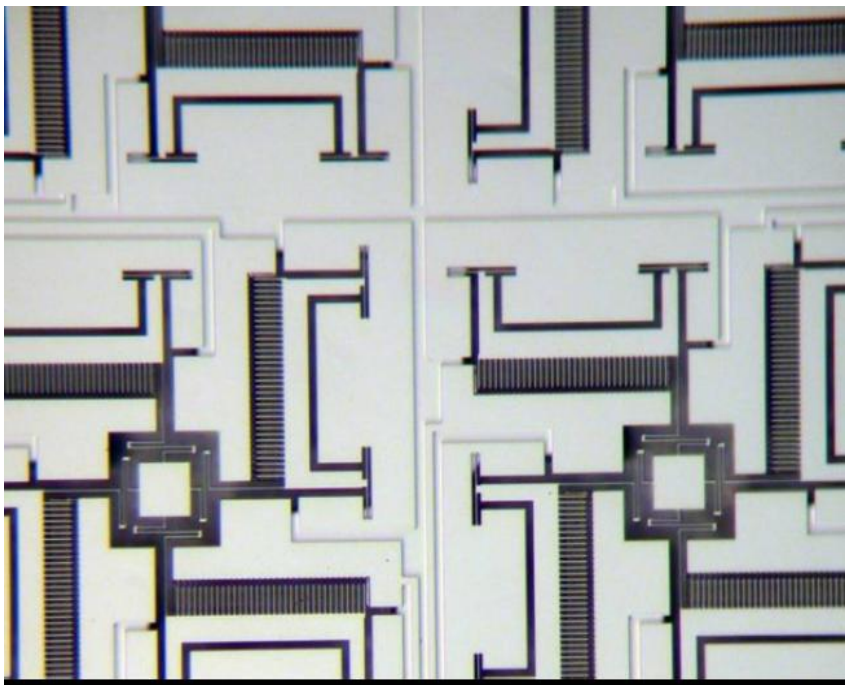

Figure 52 *– Optical micrograph of an array of tip-tilt-piston actuators; each actuator has four vertical combdrive rotators surrounding a 100 μm x100 μm stage for bonding of micromirror pedestals*

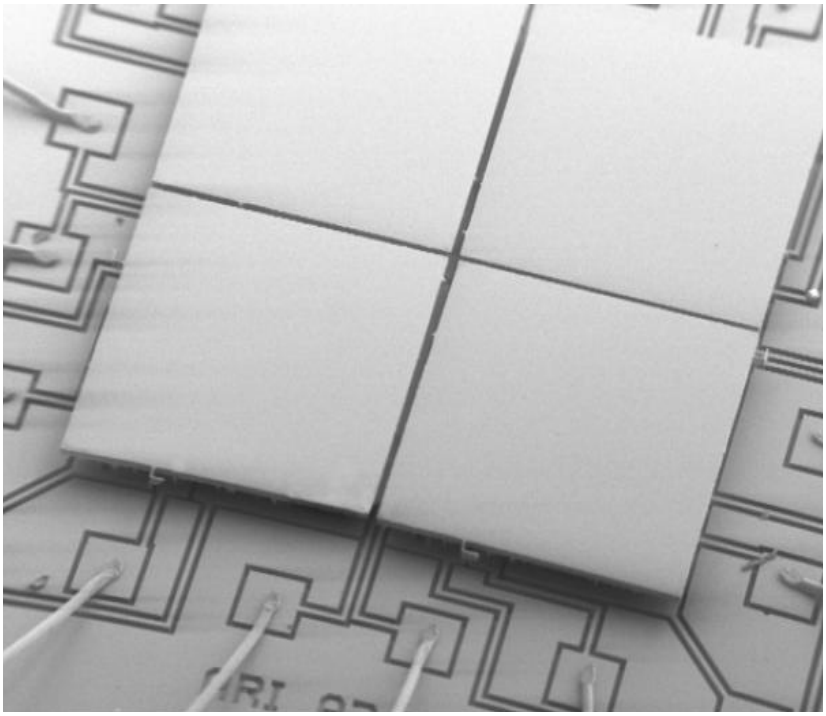

Figure 53 *– SEM micrograph of a fully assembled, functional 2x2 element array of 1.0mm x 1.0mm mirrors. Each actuator is bi-directional tip-tilt and piston type.*

Figures 54 – 58 show the 2 X 2 array in action and some achieved scans using the device.

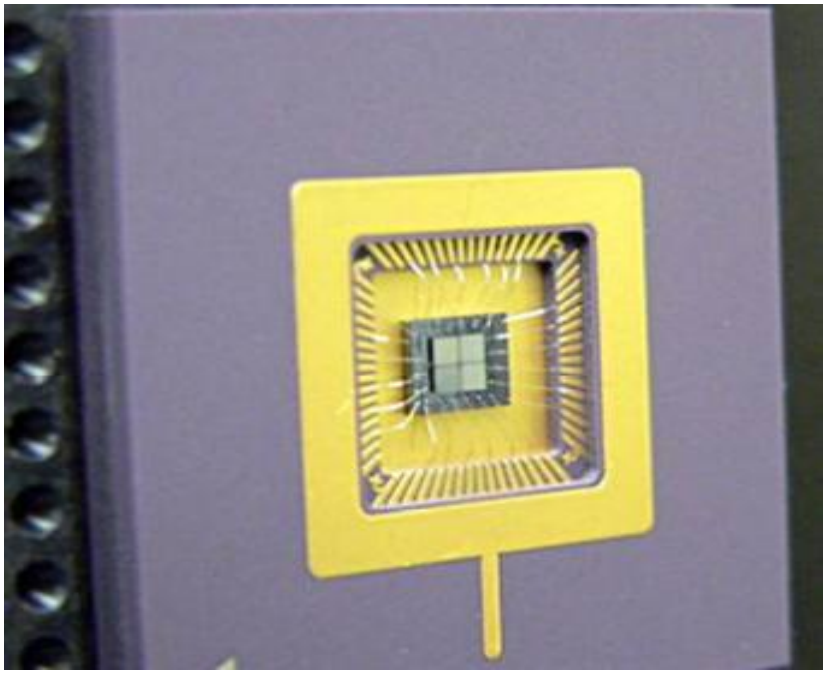

Figure 54 *– Photograph of an array in a 64-pin PGA package placed in the demonstration system board with a ZIF socket*

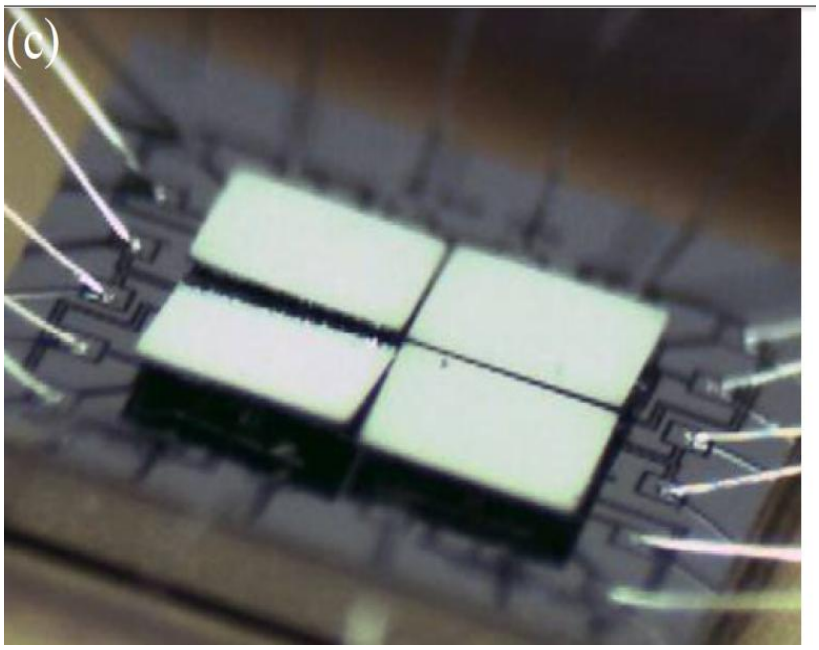

Figure 55 *– stereo microscope image of the actuated array with each of the four elements being driven by the software to act independently, some mirrors rotating in one or both axes, and one mirror pistoning.*

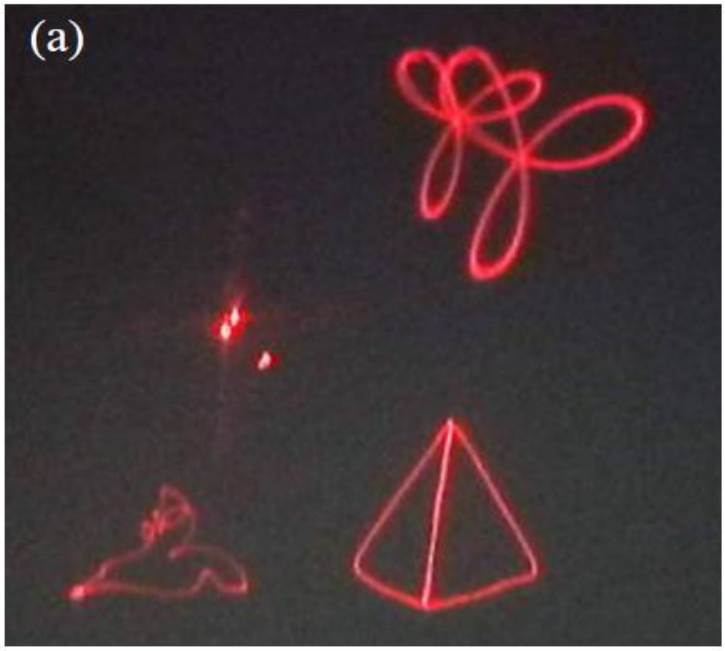

Figure 56 *– each element is being driven to trace out a different vector drawing or animation on the wall. One laser is illuminating all four elements, and their animations are offset to arrive to different areas on the wall*

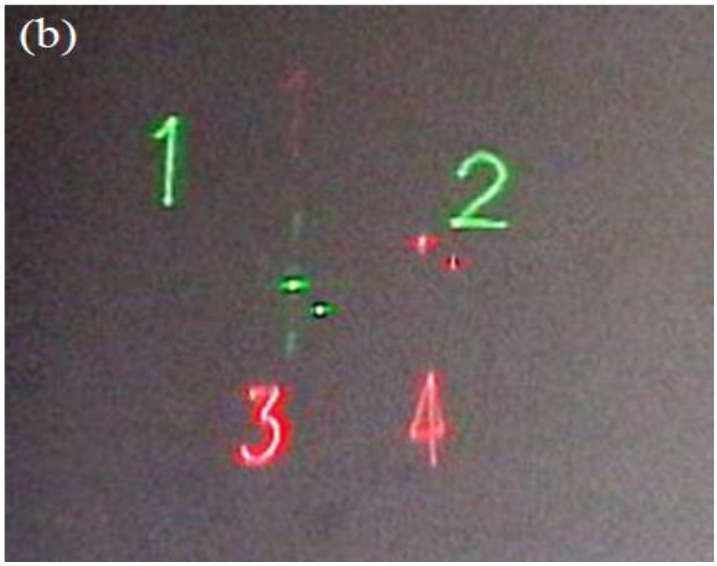

Figure 57 *– Two different lasers are collinearly illuminating the array such that the 532nm laser illuminates first row of elements and the 630nm laser the 2nd row. Each element is drawing a number representing its number for identification.*

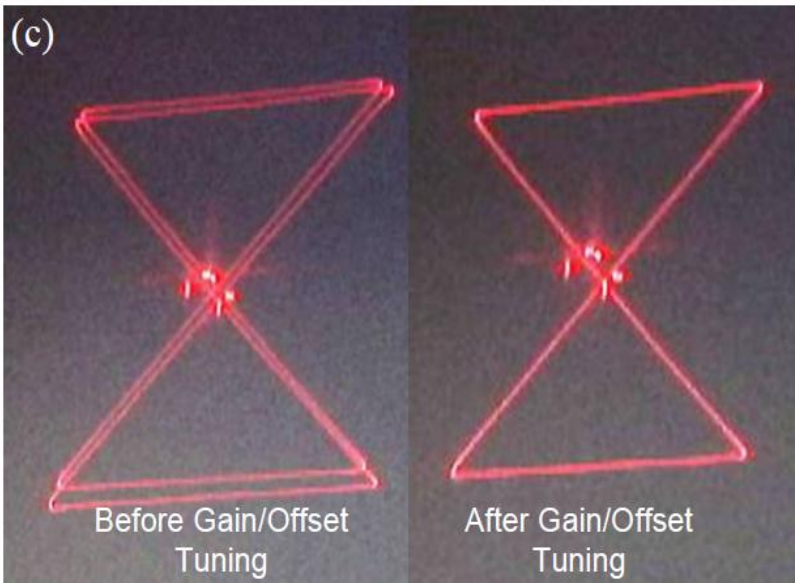

Figure 58 *– As fabricated, devices have small variations in voltage vs. Angle characteristics. Veljko Milanovic et al show a demonstration of two devices having their look-up-tables calibrated to trace out equal tip-tilt angles.*

2.4.3 Summary of MEMS

MEMS micro-mirrors have been designed and fabricated to achieve tip, tilt and piston movement abilities. Various actuation types have been tested and provide different characteristics for promise in different technological areas.

Electro-thermal bimorph actuators are a popular choice for moving micro-mirrors since large tip-tilt angles and piston displacements can and have been achieved. The main drawback with these types of system is the response time. The response time of bimorph based MEMS micro-mirrors is of the order 10ms.

Although less tip-tilt-piston displacements have been realised with electrostatic actuators the response times of the comb drive actuator designs are much quicker, to the order of 20μs. The achieved tip-tilt qualities of these systems are around ±5°, which although would only cover two thirds of our desired FOR, could potentially be used as a solution for micro-stabilisation. With the combination of a larger mirror system to scan the required 30° FOR and a comb driven MEMS mirror for micro-stabilisation there may be a solution to the requirements of this project.

The tilting micro-mirror with a liquid-metal pivot is a novel design. The problem with this system is its inability to smoothly scan the FOR. This particular design shows more promise as an optical switch due to its ability to 'snap down' when a large enough voltage is applied. Also this system only rotates on a pivot about one axis, making it very difficult to implement in to the project requirements.

2.5 Non-Linear Materials

When an intense light source such as a tightly focused laser is incident on a material it can access non-linearities in the material. Changes can be seen in the transmission of light values through the material and the materials refractive index.

Esmaeil Shahriari *et al.* [40] from the Universiti Putra Malaysia, have carried out experiments to investigate the effects of particle size on the non-linear refractive index of Au nano-fluid. They have found that by passing green laser light of 532nm through a converging lens, they could introduce a sample of Au nano-fluid around the focal point and measure the transmittance of light through the sample with a sensor **(*Figure 59*).** By moving the sample through the focussed laser light they found a non-linear change in the samples transmittance and refractive index. Plotting a theoretical fits to the closed aperture using standard equations they found that the equation fit the gathered data very well. The theoretical line was plotted with the following equation;

$$T(z,\Delta\phi) \models 1 + \frac{4\Delta\phi_o x}{(x^2+1)(x^2+9)}$$

Equation 16

where x = z/z0, z0 is the Rayleigh length (3.52 mm), ΔΦ0 = *kn2 I0 Leff* , is the phase change due to the non-linear refraction, *n*2 is the non-linear refractive index, *k* =

$2\pi/\lambda$ is the wave vector, *I0*= 4.27×10^3 W/cm^2 is the on-axis irradiance at focus (i.e., z = 0), and *Leff* = [1-exp(-α0 *L*)]/α0 is the effective length of non-linear medium, α0 is the linear absorption coefficient of the samples and L denotes the sample thickness (2 mm).

The theoretical curves show perfect symmetry indicating that the non-linearity absorption coefficients are very small. The non-linear refractive index n_2 was calculated from the change in normalized transmittance from the peak to the valley between -3mm and 3mm in the z scan displacement (***Figure 60***)**.**

$$\Delta T_{p-v} \approx 0.406\,(1-s)^{0.25}\,|\Delta\phi_o| \qquad \textbf{\textit{Equation 17}}$$

Where *s* is the linear transmittance of the aperture. It was found that the non-linear refraction coefficient tends to increase linearly with increase in particle size.

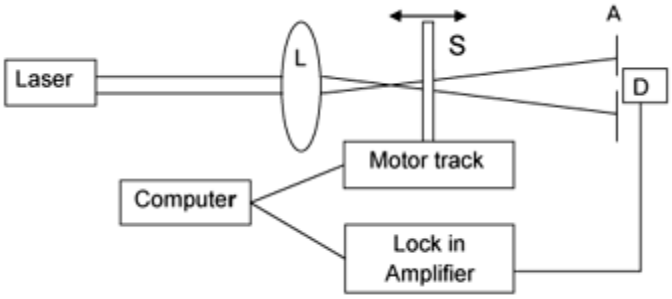

Figure 59 – Schematic diagram of the Z-scan experiment setup by Esmaeil Shahriari et al

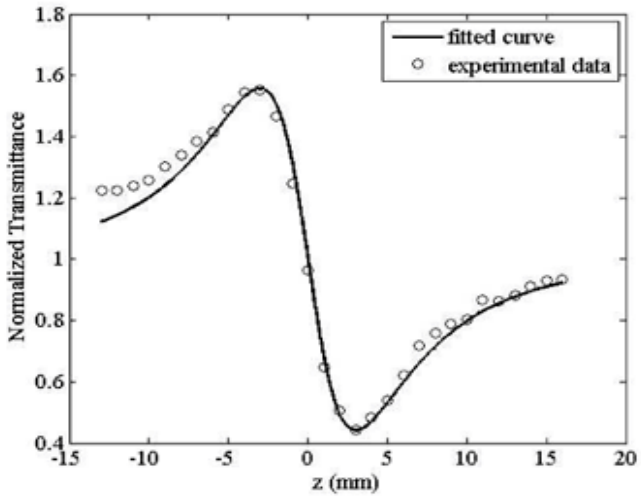

Figure 60– Experimental data of Normalized transmittance against the z scan displacement with theoretical curve fitted.

In conclusion it was found that the third order non-linearity refractive index of Au nano-fluid prepared at different particle sizes but with a fixed concentration could be measured. The Au nano-fluid showed a good third order non-linear response. The non-linear refractive index was found to be of negative sign and with a magnitude of around 10^{-8} cm^2/W. The non-linear effect was found to increase linearly with the change in particle size that ranged from 7.0nm to 18.7nm (***Figure 61***).

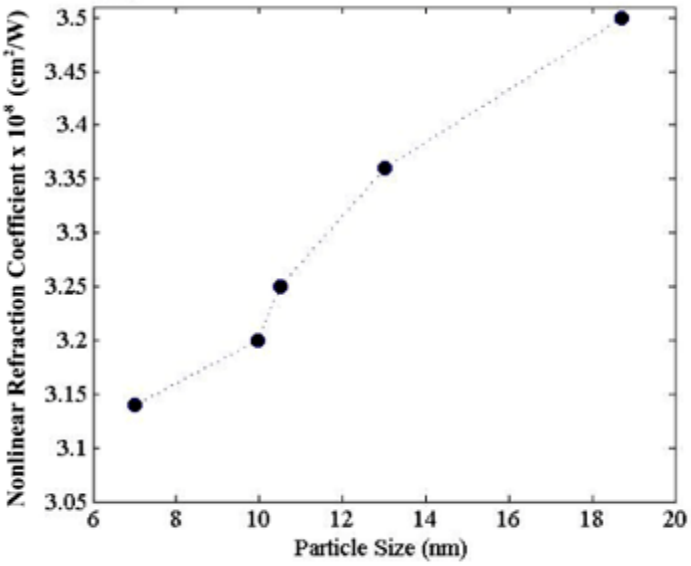

Figure 61– The linear relationship between non-linear refraction coefficient and particle size for Au nano-fluid

2.5.1 Summary of Non-Linear Materials

Although non-linear materials show promise for lens applications there is little in the way of development. It has been shown that refractive indices can vary with methods such as changing particle size. Variable focal lengths have been achieved but the ability to change the shape and direction of incident wave fronts is still yet to be addressed with this type of technology. Because of its lack of maturity in development this type of technology does not fulfil the requirements outlined by the project aims.

2.6 State of the Art Electro Optics Conclusion

Technology	Wavelength, λ	Diameter of Aperture	Time Constant	Angular Response / Physical Range	Price	Pay Load Mass	Device Size	TRL	Where can you get it?
Liquid Lens	Visible – Near Infrared	~ 2-5mm	2-20ms	Possible tilt - ±0.6° Focal Range – 15mm to infinity			~6mm	High	Various websites
Liquid Crystal Lens	Visible	60mm	Typically ~ms 1 case claims <µs	Focal Range: (-)0.164m - (+)0.217m Focal Range: 60µm – 450µm No steering effects			60mm by 10mm	Medium	Systems fabricated but not available to buy
Beam Steering Risley Prisms	Visible and MWIR (2.0 µm – 4.7µm) (appropriate material choices should yield far IR capability)	10mm – 120mm	Depends on mechanism	FOR – 90° - 120° Pointing Accuracy: 1.0mrad – 1.78mrad		1.04kg	For 25mm diameter aperture Diameter – 58mm Length - 89mm	High	Opnus – Electro-optical products
Beam steering Risley Grating	Visible to MWIR			FOR - 62° (Determined by grating period) 0% dispersion (in theory)				Low	
Beam steering Decentered Lens System	Visible and MWIR (2.0µm – 5.0µm) (appropriate material choices should yield far IR capability)	~70mm	Depends on Mechanism	FOR - 45° Range - 6 km Throughput – 98% for 2 µm, 63% for 5 µm Accuracy <1mrad dispersion				High	Various websites (see report)
Beam Steering Mirror Sytems	Visible and Infrared	12.5mm	sub-milliseconds	≈6.8° in currently available products. Depends on actuation Angular resolution -sub-µrad			Height – 33mm Width – 25mm Depth – 34.5mm	High	Various websites (see report)
MEMS Array - Bimorph Actuated	Visible and Infrared	1mmx1mm per mirror 4x4 Arrays available	10ms	Tip-Tilt: ±30° Piston displacement:480µm			~16-20mm^2	Medium	Systems fabricated but not available to buy
MEMS Array - Comb Drive Actuated	Visible and Infrared	1mmx1mm per mirror 2x2 Arrays	20µs	Tip-Tilt: ±5° Piston displacement:±1.2µm			~4-9mm^2	Medium	Systems fabricated but not available to buy

Table 2 *– Characteristics of current state of the art opto-electric technologies*

Table 2 concludes the characteristics of each of the technologies outlined in this report. A traffic light system has been utilized to show how the characteristics of the materials match the requirements in this particular project. Red indicates that this characteristic is not fitting to the project requirements, and so any technology containing at least one red will be dismissed from this point onwards. Amber indicates that the

technology is in an intermediate state, where currently does not fit the requirements but shows promise with adjustments or current developments. Green indicates that the technology is ready in this particular area for the project requirements.

From ***Table 2*** it is clear that there are four different technologies that only consist of green or amber rated characteristics. The most promising of these four technologies for this project appears to be the de-centred lens technology. Another possibility would be to utilize a macroscopic FSM to scan the required FOR and employing a MEMS micro-mirror system for micro-stabilization. The Newport FSM-300 and PI S334 specifications suggest that a macroscopic FSM may be able to cope with the larger FOR requirements and the micro-stabilisation required alone.

To proceed with the de-centred lens option the optical design software Zemax will be used in attempt to satisfy the project requirements. Zemax can also be used to incorporate mirror systems in to the design if needed.

3. Zemax Optical Design 1

3.1 Subsystem Specification

The objective of this section of the project is to design a decentred lens system that meets the requirements of the CPS provided by the sponsor. The Optical Specification is outlined in ***Table 1*** and ***Figure 62***.

Focal length	**48 mm**
F-number	1 - 1.2
Field-Of-View (full)	30° x 22.5°
Field-Of-View at sensor level	25.2 mm x 18.9 mm
Total length (including focal plane)	≤ 150 mm (TBC)
Optical MTF at 2 cy/mrad (42 cy/mm)	> 20% (TBC)
Required field values of MTF (radius at focal plan level)	0 mm
	13 mm
Mass of the moving lens	≤ 50 grams (TBC)
Stroke	Cf. Actuator and Sensor CPS
Temperature range	[-40°C; +70°C]

Table 1 *- Optical Specification taken from the CPS from the sponsor.*

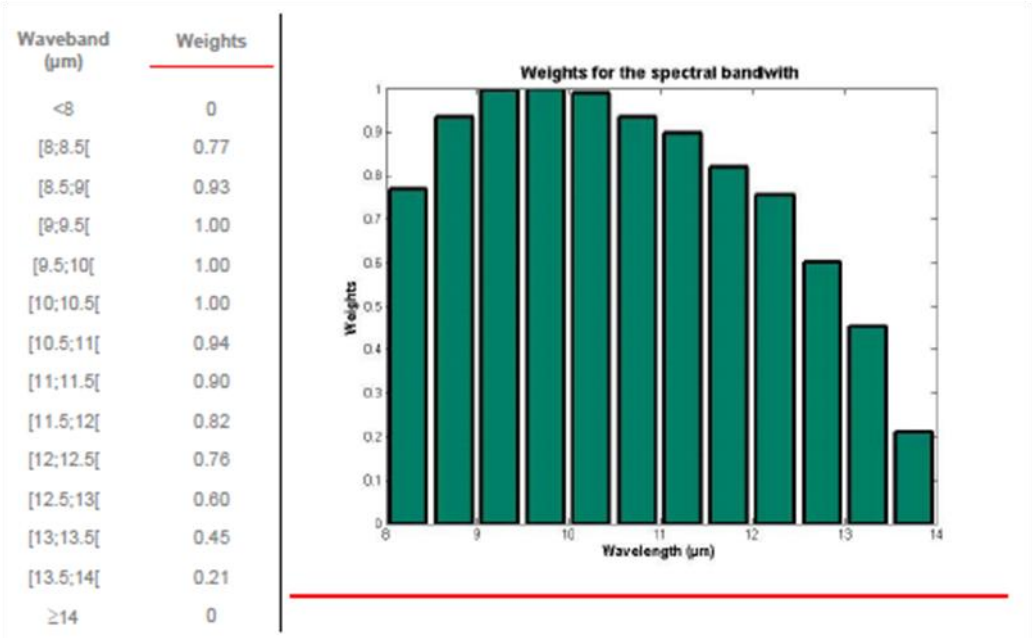

Figure 62 *– Typical spectral weighting for an uncooled detector.*

3.2 Lens Materials

The first action to take was to make a choice of suitable lens materials for the spectral weighting provided, covering the 8µm to 14µm wavelength range, with most emphasis on the 9µm to 10.5µm range. There are far less materials available over the infrared wave band than the visible part of the spectrum, however by studying designs in the Zebase Zemax database it is clear that there are recurring choices in materials for the 8-12µm and 8-14µm wavelength ranges. From this it has been chosen to take a closer look at using Germanium, AMTIR-1 and ZnSe as the IR lens materials in this design. ***Figure 63***, ***Figure 64*** and ***Figure 65*** show some typical transmission spectrums for these materials.

- Germanium

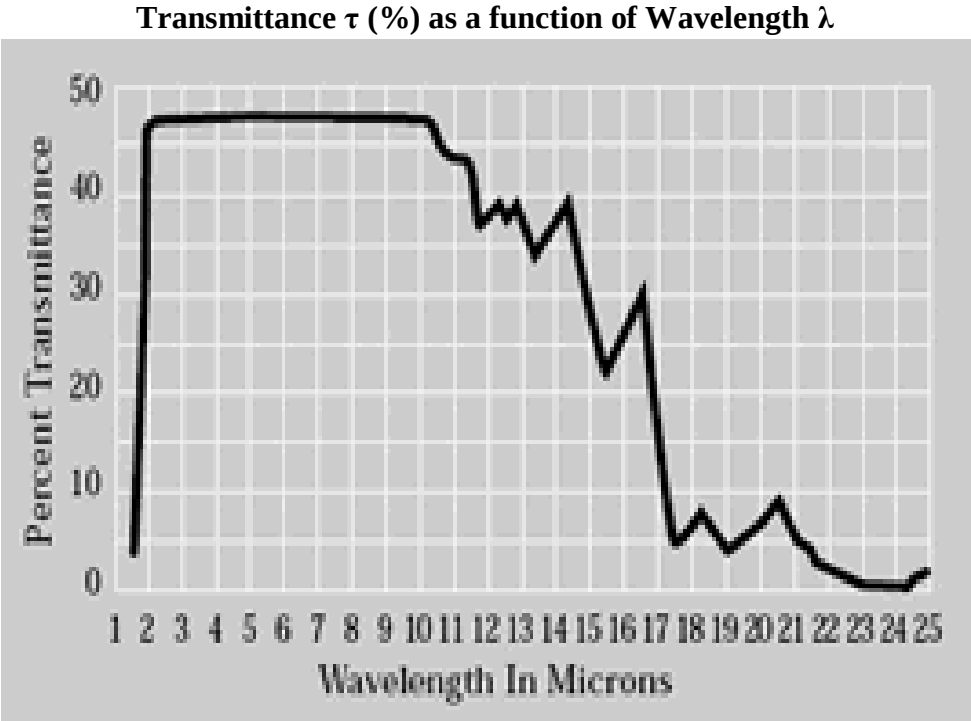

Figure 63 – *Transmission spectrum of Ge.[41]*

- Zinc Selenide

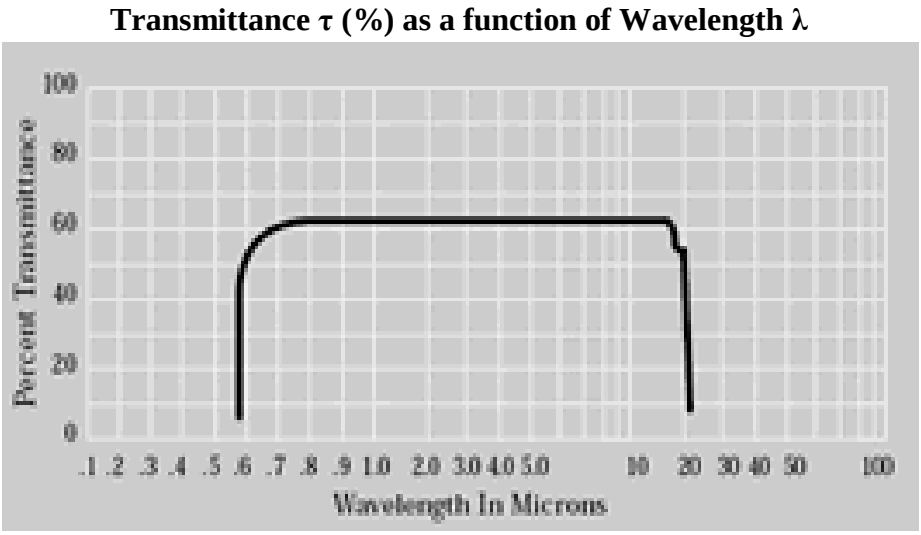

Figure 64 *– Transmission spectrum of ZnSe.[41]*

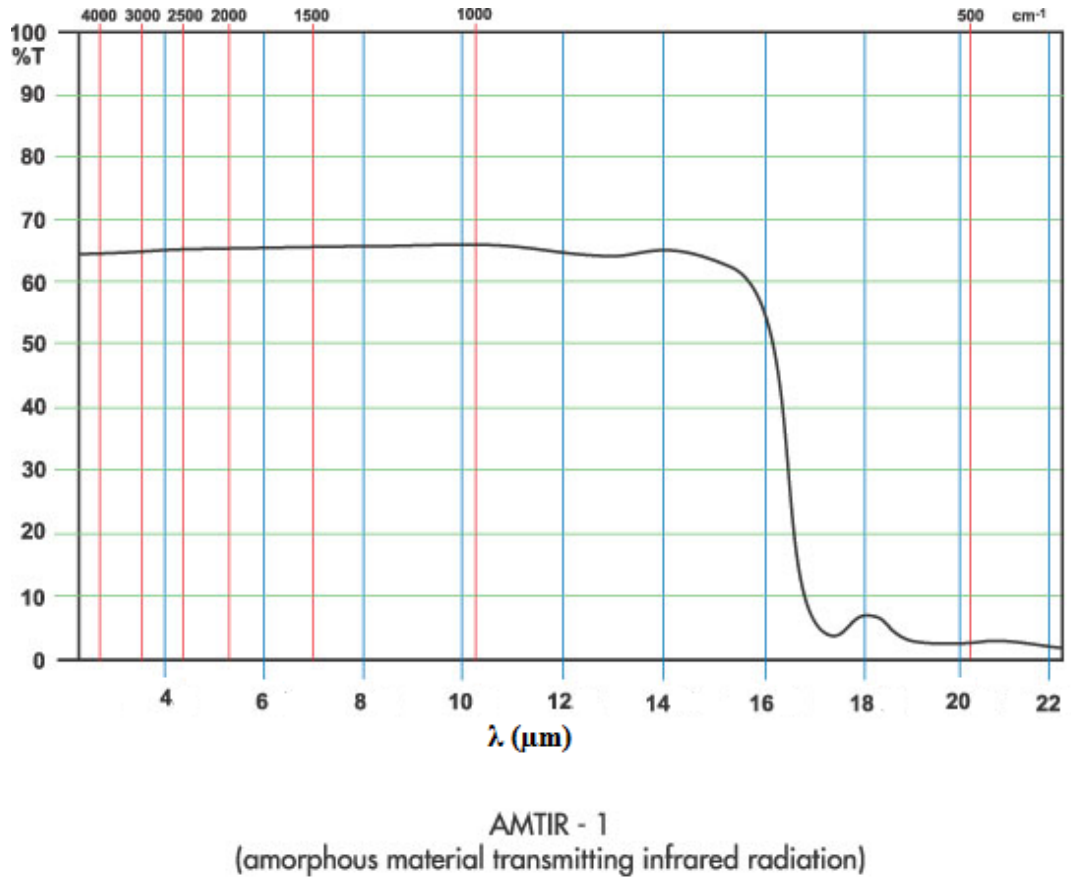

Figure 65 *– Transmission spectrum of AMTIR-1.[42]*

Materials	Refractive Index	Transmission Range(um)	Thermal Expansion Coefficient (10^{-6}/K)	Density(g/cm^3)
BK7	1.5164 (588nm)	0.330 - 2.1	7.5	2.52
Fused Silica	1.4858 (308nm)	0.185 - 2.5	0.58	2.20
Quartz	n_o=1.5427 n_e=1.5518 (633nm)	0.200 - 2.3	13.2||a;7.1||c	2.65
CaF_2	1.399 (5000nm)	0.170 - 7.8	18.85	3.18
MgF_2	n_o=1.3836 n_e=1.3957 (405nm)	0.120 - 7.0	13.7||a;8.48||c	3.17
Sapphire	1.755 (1000nm)	0.180 - 4.5	8.4	3.98
Silicon	3.426 (5000nm)	1.2 - 7.0	2.55	2.33
Germanium	4.004 (10000nm)	2.0 - 14.0	5.5	5.33
ZnSe	2.4028 (10600nm)	0.55-20.0	7.6	5.27
YVO_4	n_o=1.9500 n_e=2.1554 (1300nm)	0.400 - 5.0	4.43||a; 11.37||c	4.22
Calcite	n_o=1.6557 n_e=1.4852 (633nm)	0.210 - 2.3	5.68||a; 24.39||c	2.7
a-BBO	n_o=1.6749 n_e=1.5555 (532nm)	0.190 - 3.5	4.0||a; 36.0||c	3.85
$LiNbO_3$	n_o=2.2863 n_e=2.2027 (633nm)	0.370 - 4.5	14.8||a;4.1||c	4.64

Table 3 *– Properties of various IR materials.[41]*

Table 3 contains information on the refractive indices, transmission ranges, thermal expansion coefficient and density of many infrared materials. Highlighted are the rows containing information on Germanium and Zinc Selenide. Out of the IR materials in the table these are the only two that cater for the transmission range that is required. ***Table 4*** shows the general properties of AMTIR-1 (amorphous material transmitting Infrared radiation).

Composition	$Ge_{33}As_{12}Se_{55}$ Glass
Density	4.4 gms/cm^3
Thermal Expansion	12 X $10^{-6}/^{\circ}C$
Hardness (Knoop)	170Kgf/mm^2
Rupture Modulus	2700 psi
Young's Modulus	3.2 X 10^6 psi
Shear Modulus	1.3 X 10^6 psi
Poisson's Ratio	0.27
Thermal Conductivity	6 cal / cm sec$^{\circ}$K X 10^{-4}
Specific Heat	0.07 cal / gm $^{\circ}$K
Upper Use Temperature	300°C
Resistivity	2 X 10^{12} Ω cm @ 100Hz
Glass Transition Temperature	362°C
Annealing Temperature	370°C

***Table 4**– General Properties of AMTIR-1 [43]*

3.3 Design Basis

To begin the optical design a file from the Zebase 6 optical design database was chosen to use as a basis on which to build. The chosen design is shown in ***Figure 66***, it contains similar features to those required in this project, in particular the total track length being less than 150mm, and a reasonable F/# to work with at ~1.5.

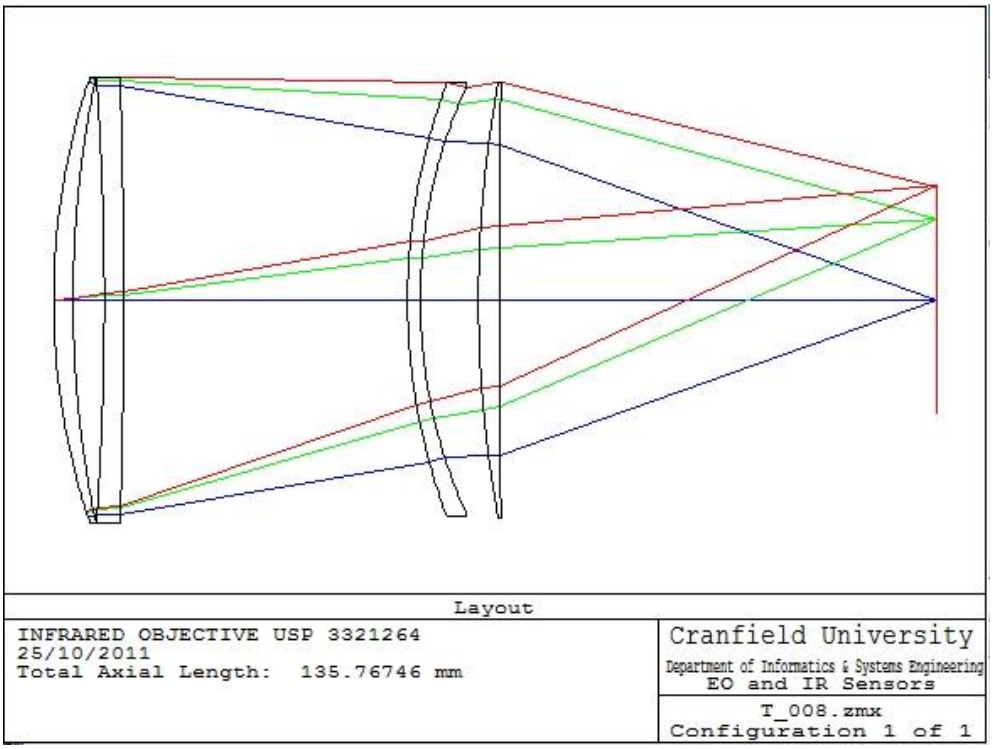

Figure 66 *– Zebase design T_008.zmx system layout.*

3.3.1 Setting System Characteristics

The lens materials in this particular design are Si, Ge, Ge, Si respectively. The incident wavelengths are 2µm, 3µm and 4µm. To allow for the transmission range required the first and last lens materials were replaced by AMTIR-1. Next the curvature of the last lens was defined by specifying the system to be that of an F/1 nature. Any change in the system such as the distances between each component and the curvature of the other surfaces now causes an automatic change in curvature of the last lens to ensure an F/1 system is maintained. The next feature to be defined was the focal length, f, of the system. In order to accomplish the desired focal length the entrance pupil diameter was changed considering ***Equation 18***.

$$\mathbf{F} = \frac{\mathbf{f}}{\mathbf{D}} \qquad \textit{Equation 18}$$

Where **D** *is the entrance pupil diameter of the system,*
F *is the system F-number and,*
f *is the focal length*

The CPS states that the required focal length is 48mm, and that an F/1 system is desired, however an F-number of up to 1.2 would be acceptable. Equation 1 can be re-arranged to find the required entrance pupil diameter, D. With an F/1 system the diameter of aperture is equal to the focal length, and so the entrance pupil diameter was set to be 48mm.

3.4 Initial Design Development

Figure 67 shows the 2D layout of the initial design, optimised for the RMS spot size at the focal plane. As an estimate to focal plane dimensions at this stage each pixel was taken to have a diameter of 20µm. Therefore a sensor of 1024pixels by 768pixels would be 20.48mm by 15.36mm. Taking this in to account the spot diagrams were taken at the centre of the focal plane, the edges of the focal plane and at the corner of the focal plane. As the system at this point was symmetric in both x and y planes the direction from the origin was not as important as the distance from the origin. Therefore spots diagrams were taken from 0mm, 7.68mm, 10.24mm and 12.80mm to analyse the performance of the system (***Figure 68***).

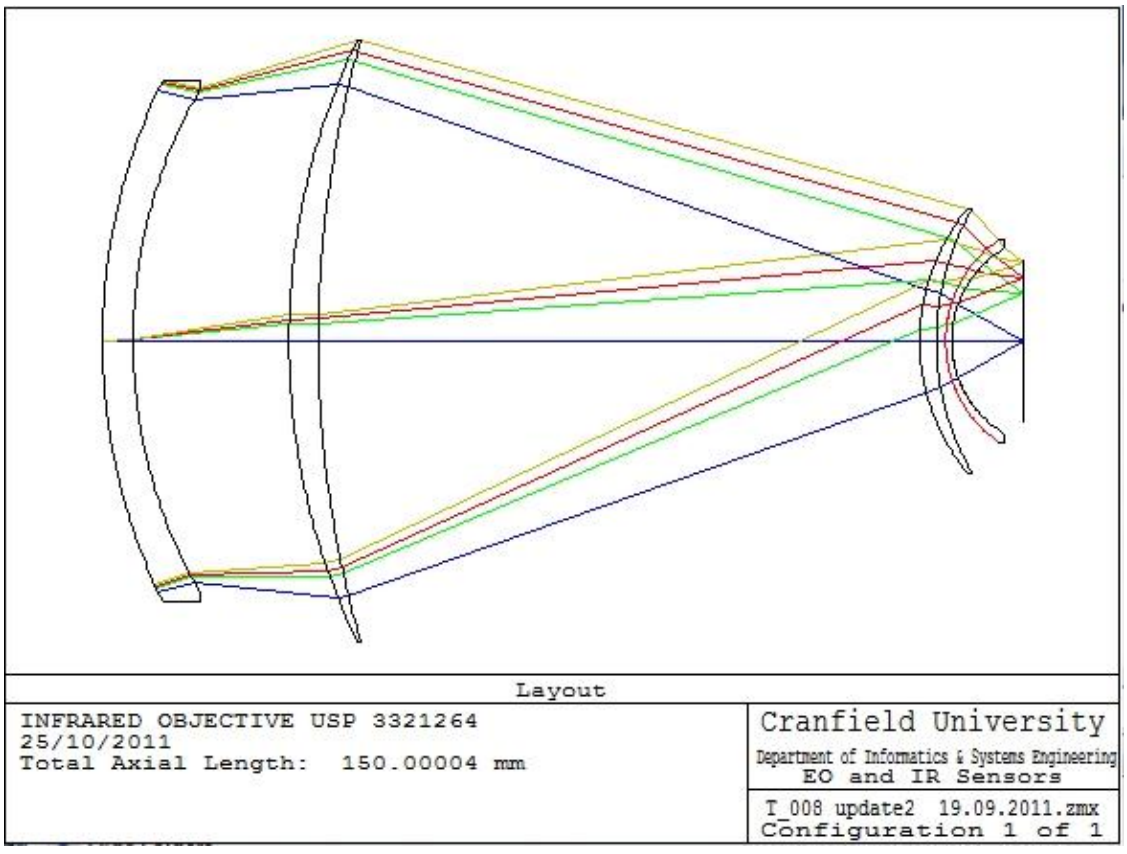

Figure 67 *– Initial design 2D layout.*

3.4.1 System Analysis

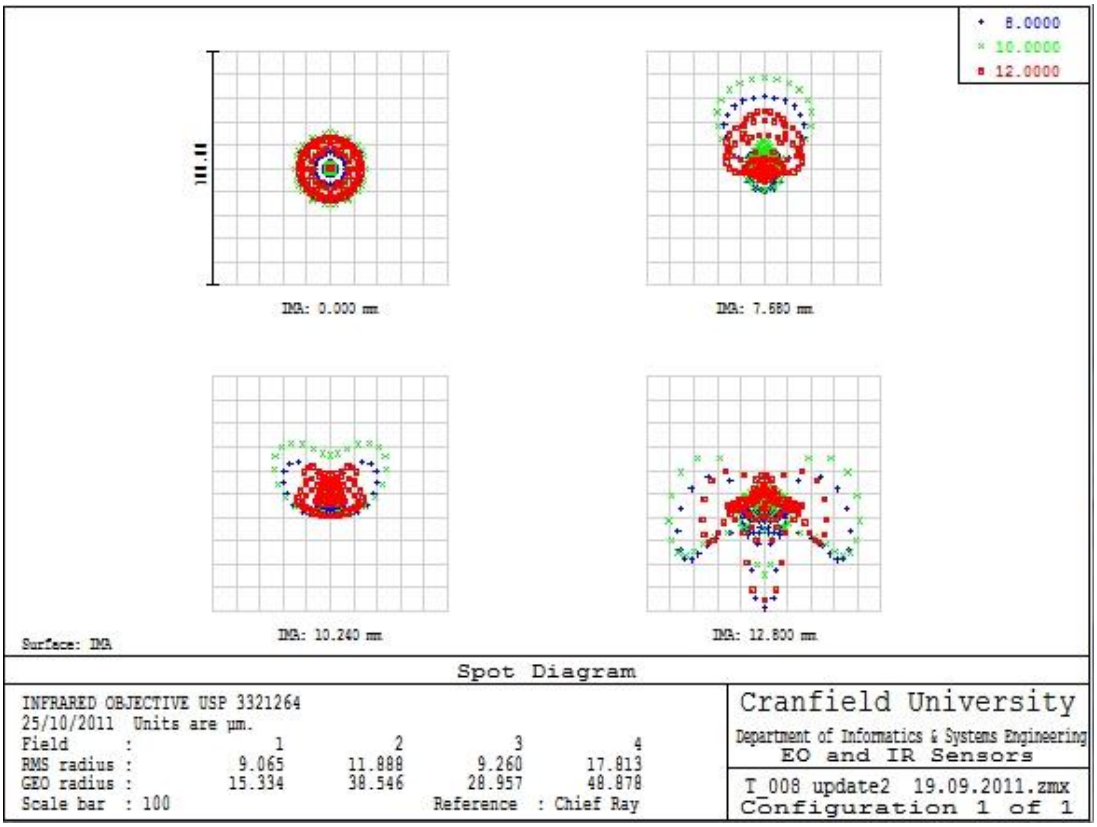

Figure 68 *– Initial design spot diagrams.*

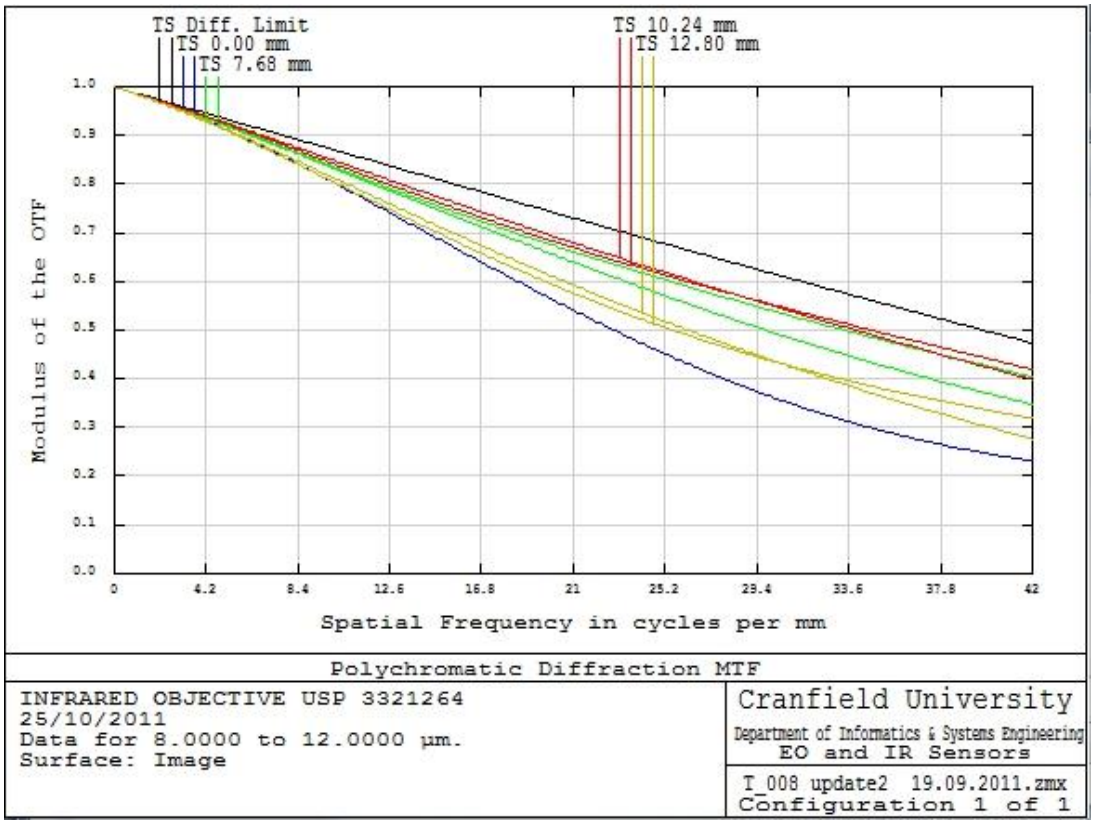

Figure 69 *– Initial design FFT MTF.*

Figure 68 contains the spot diagrams at the centre of the focal plane and the three specified off axis points. The on axis spot has an RMS radius of 9.065µm and this becomes progressively larger moving away from the centre of the focal plane. Ideally the spot diameter should be ~ a pixel (~12µm) and so these spot sizes need to be improved. ***Figure 69*** shows the MTF plots at these specified distances from the centre of the focal plane. These all meet the requirement that the optical MTF must be greater than 20% at 42cycles per mm as outlined in the required specification ***(Table 2)***, however to allow for tolerancing and athermalisation the nominal MTF is desired to be greater than 30% at 42 cycles per mm.

3.4.2 Conclusion

The initial design shows some potential in terms of achievable spot sizes and MTF values. The main problems with the initial design are as follows:

- Spot sizes need to be reduced to the size of a pixel, therefore around 12µm.
- MTF values are acceptable (>20% at 42 cycles per mm) however have potential to be better compared to the diffraction limit (shown by the black line).
- Lenses in the design are thin giving the potential to be expensive to manufacture.
- Lenses 3 and 4 are largely curved and therefore would also be an added factor to the expense of the manufacturing process.
- Large diameters of lenses giving cause for concern of system mass being large.

3.5 Stage 2 Design Development

3.5.1System Design

Taking in to account the points made in the conclusion above the next step of the optical design was made. The two dimensional layout is shown in ***Figure 70***.

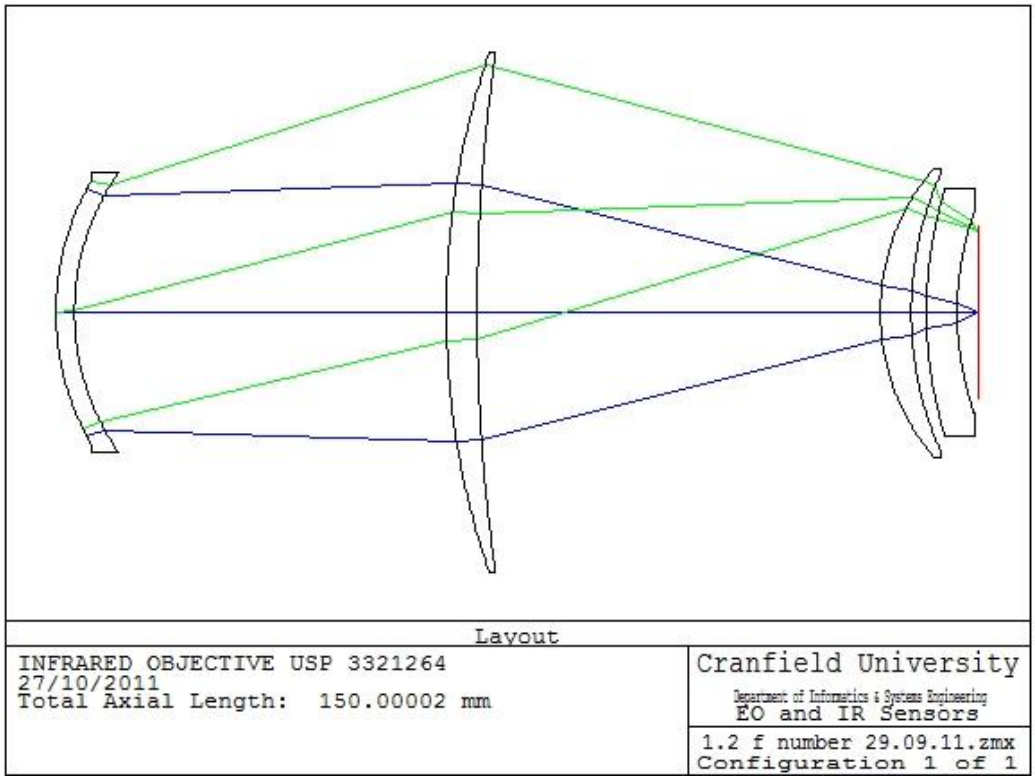

Figure 70 *–2D Optical design layout.*

From ***Figure 70*** it is clear that improvements have been made to the curvatures of the third and fourth lenses in the system. The diameter of the second lens still needed to be addressed at this point. The large diameter of the second lens results in the lens edges being thin. This could result in the manufacturing of the lens being expensive. The improvement in curvature of lens three and four is at the expense of performance at this point in the design. This is shown in ***Figure 71*** and ***Figure 72***.

3.5.2 System Analysis

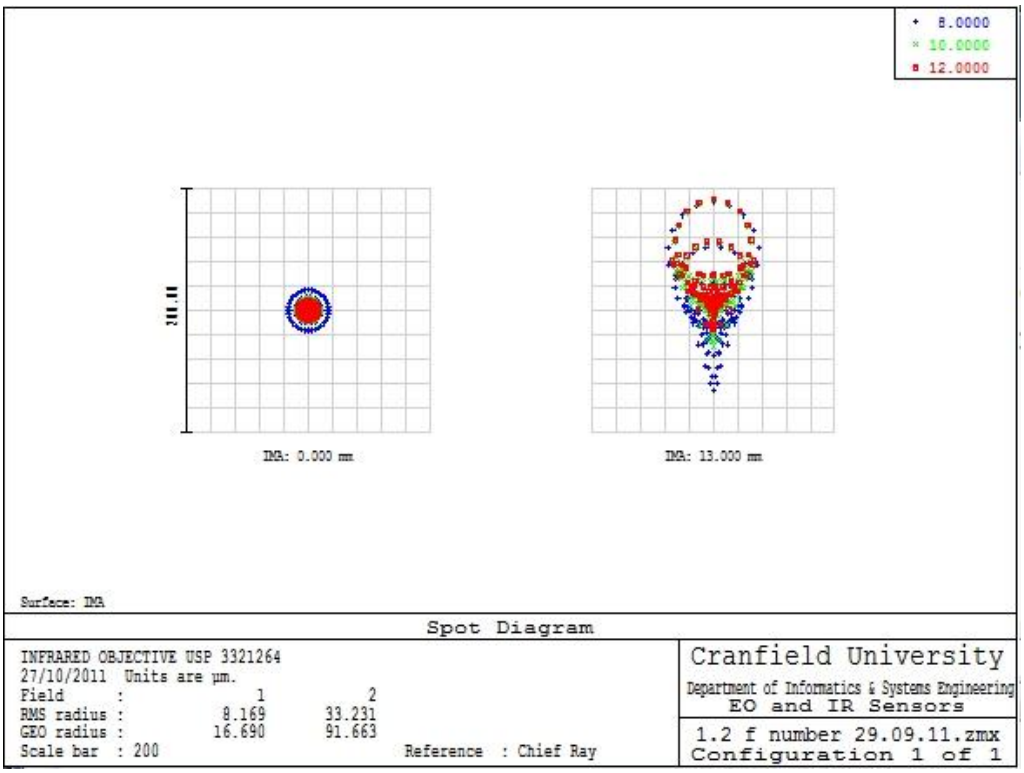

Figure 71 *– First updated design spot diagrams.*

The RMS radius of the spot at the centre of the focal plane is 8.169 microns. The RMS radius of the spot at 13mm from the centre of the focal plane is 33.231 microns and so needs to be improved.

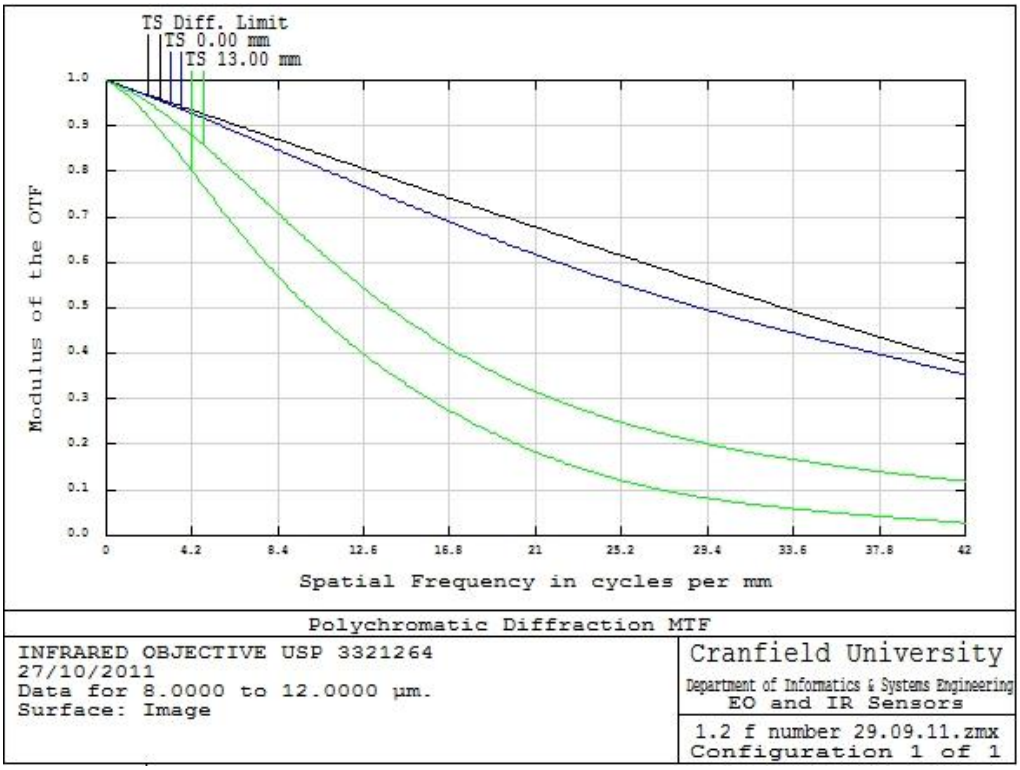

Figure 72 *– First updated design FFT MTF.*

The On axis beam shows results close to the diffraction limit however the tangential and sagittal curves of the beam at 13mm quickly fall away from the diffraction limit showing room for improvement.

3.5.3 Conclusion

- Spot radius of the off axis spot needs to be dramatically reduced. This could be achieved by addressing the angle of incidence at each interface, making sure that there is not too much refraction at each lens surface.
- The off axis MTF is lower than the required 20% at 42 cycles per mm. The black line on the graph is the diffraction limit representing the maximum achievable values due to diffraction effects. The on axis performance is acceptable however the off axis performance needs to improve.
- The edges of the second lens are thin giving ineffective potential to low costs in manufacturing. The first lens in the system is also thin and so also needs to be addressed. By reducing the total length of the system the diameter of the individual lenses should be able to be reduced, making the lens edges thicker and the mass of the individual lenses less.
- The distance between the last lens surface and the focal plane needs to be addressed to allow for any housing in which the sensor may be contained. The distance between the centre of the rear surface of the last lens and the focal plane is 3.5mm; however the positive curvature of the rear surface means the edges of the lens are closer to the focal plane than this point.

3.6 Stage 3 Design Development

3.6.1 System Design

To improve the performance of the system in terms of spot size and MTF an additional lens has been added to the system. The F-number has been increased slightly to 1.2, and so the entrance pupil diameter has been decreased to 40mm to maintain a 48mm focal length. The length of the system has been reduced ~100mm allowing for smaller lens diameters. The back focal length of the system has been increased to allow space for the image sensor housing. ***Figure 74*** shows the 2D layout of the optical system at this point, including rays traced to focus at the centre of the focal plane and at a distance of 13mm from the origin. The performance in terms of spot size worsens as the focal point is moved away from the centre of the focal plane. For this reason there are only two focal points taken in to account, the one at the centre of the focal plane (0mm) and one furthest from the centre of the focal plane (13mm).

The curvature of the lenses are much more acceptable at this point, however the edges of the fourth lens are still thin and so this may need to be improved. The angle of incidence of the top ray hitting the front surface of the last lens in the system appears to be large. This could cause problems in transmission values when applying coatings to the lens surfaces. ***Figure 73*** shows the optical interface of the image sensor. From this it has been deduced that the minimum back focal length is 1.37mm.

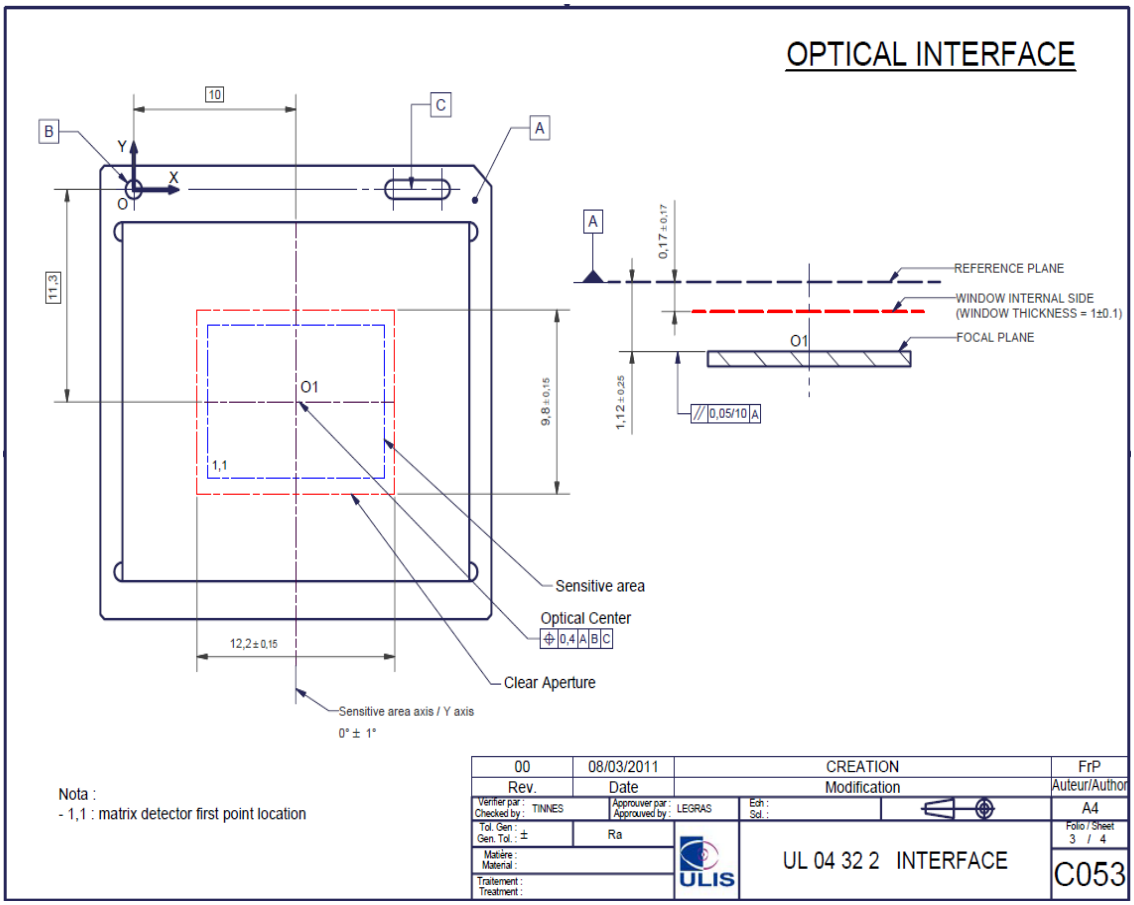

Figure 73 *– Optical interface of the image sensor.*

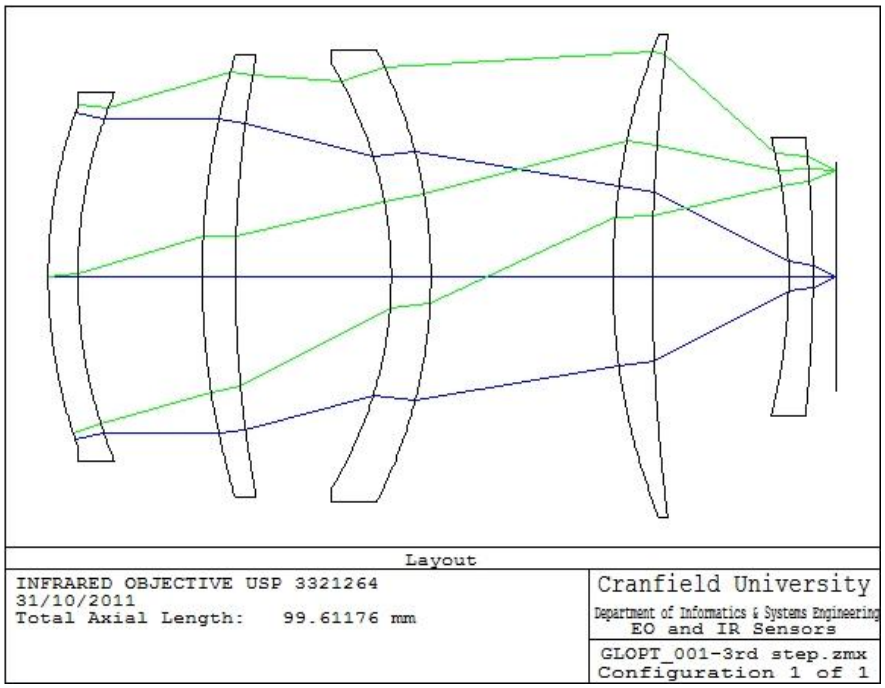

Figure 74*- 2D optical design layout.*

3.6.2 System Analysis

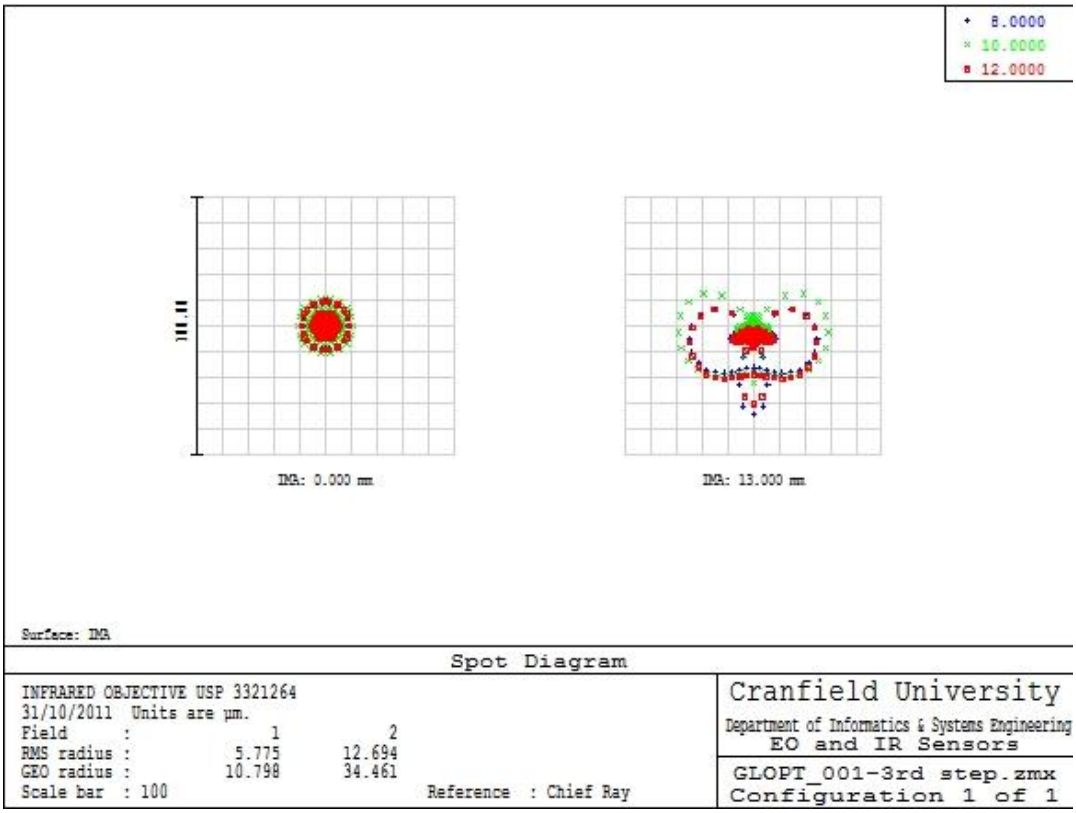

Figure 75 *– Spot diagrams at the z plane origin and at 13mm from the origin.*

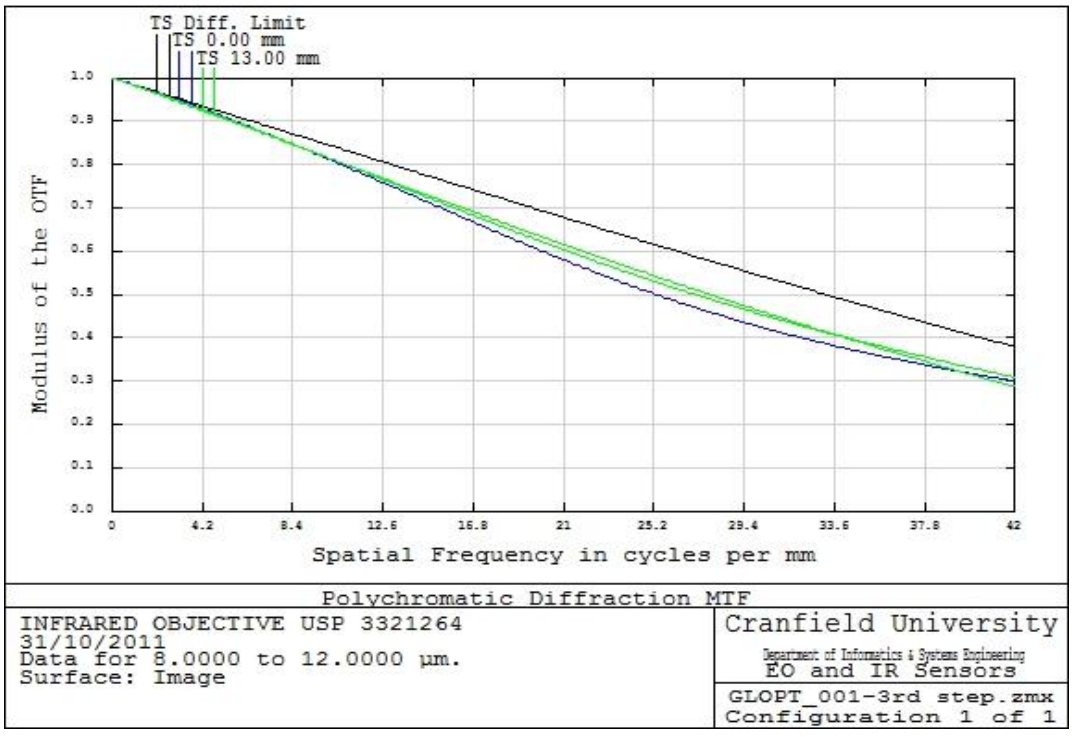

Figure 76 *– Optical MTF at 0mm and 13mm from the focal plane centre.*

From ***Figure 75*** it is clear that the spot sizes have been improved from the last step in the design. The on axis spot has an RMS radius of 5.775µm however the RMS spot radius at 13mm is 12.694µm and still needs to be reduced.

Figure 76 shows the MTF's for 0mm and 13mm from the centre of the focal plane. It is clear from this that the 0mm MTF has decreased by around 5% however the MTF at 13mm has improved and is now acceptable. Both cases show results of ~30% at 42 cycles per mm. There is room for some improvement in MTF values however the diffraction limit shows that the maximum MTF at 42 cycles per mm is <40%.

3.6.3 Conclusion

- Lens curvature and thicknesses are much more manageable with potential to be more cost effective.
- The back focal length is long enough to allow space for the image sensor casing.
- Optical performance of the system has been improved. Satisfactory MTF values have been achieved meeting the requirement of ~30% at 42 cycles per mm.
- Spot diagrams show that although progress has been made there is still need for reduction in the radius of the 13mm spot.
- Angles of incidence at air to glass interfaces need to be less than 45° as large angles of incidence could result in lower transmission values and loss in optical quality. This may need to be addressed in the final lens of the system.

3.7 Stage 4 Design Development

3.7.1 System Design

To improve the performance of the system the single lenses in the previous designs have been changed for Ge/ZnSe doublets. The system has again been optimised for RMS spot size, resulting in much improved GEO spot sizes and improved MTF data. ***Figure 77*** shows the two dimensional layout of the system.

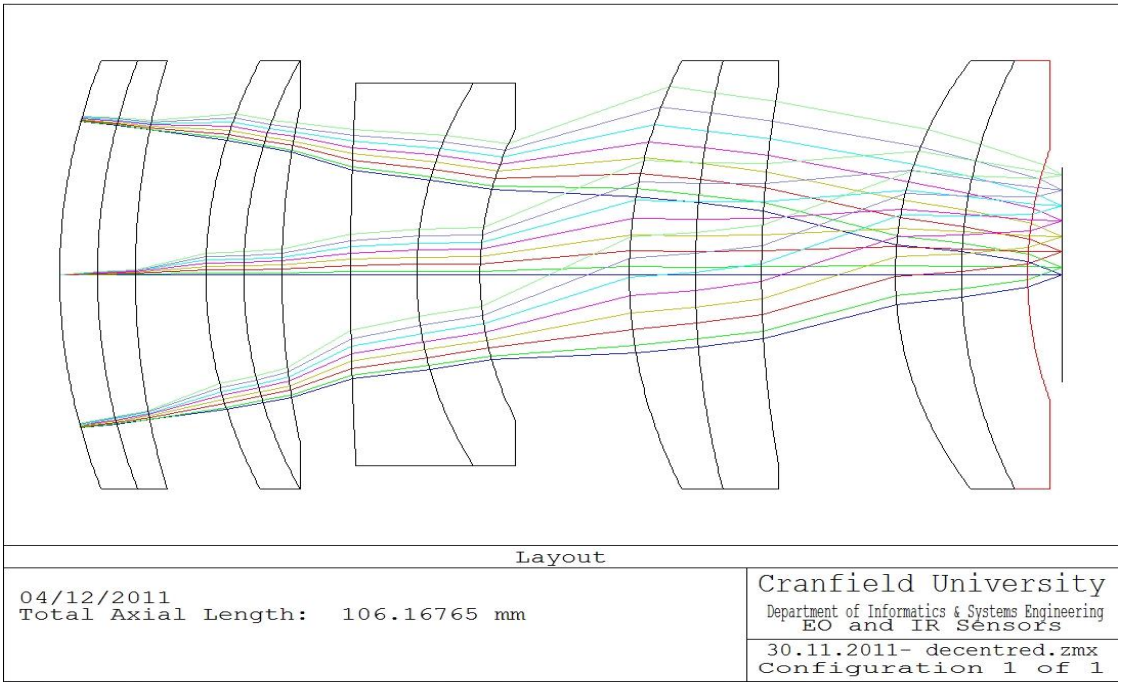

Figure 77 *– 2D design layout.*

3.7.2 System Analysis

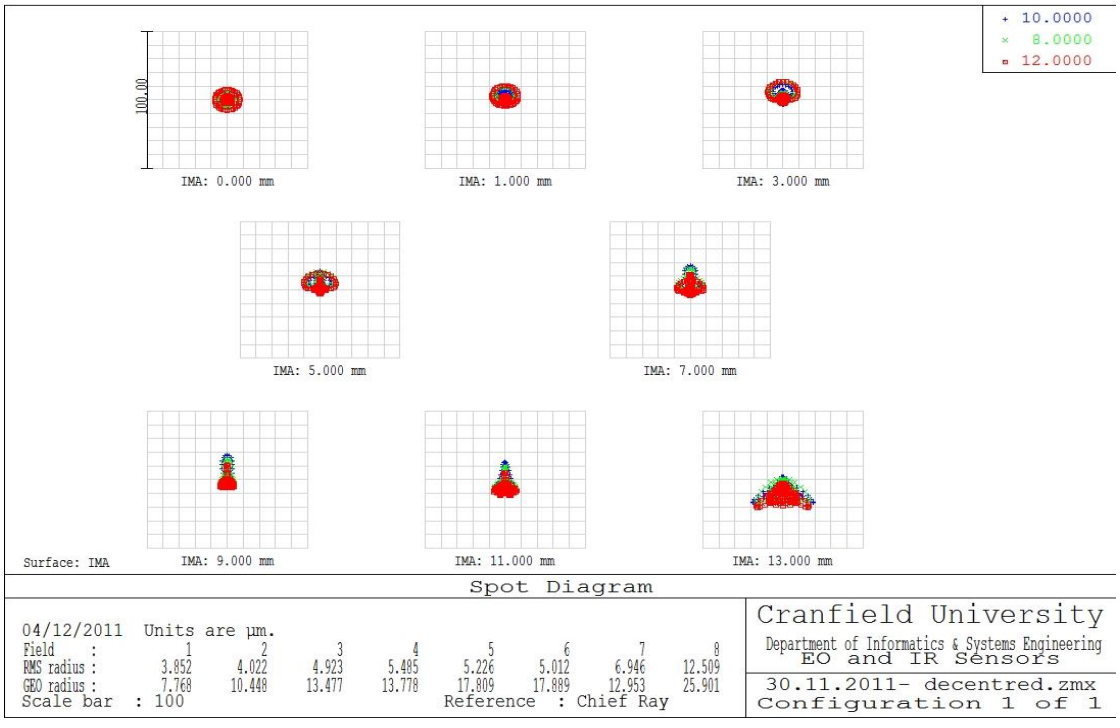

Figure 78 *– Spot diagrams on axis, 8µm-12 µm wavelength*

Figure 78 shows that the spot sizes between 0mm and at 13mm from the centre of the focal plane have been improved. The primary wavelength has been set to 10µm to

satisfy the weightings set by Sagem in the CPS. All spots have an RMS radius of less than 12.51µm.

Figure 79 contains the MTF data for the system at this stage. For all spots between 0mm and 13mm the requirement of >20% at 42 cycles per mm is satisfied in both Sagittal and Tangential planes. The MTF curves fit closely to the diffraction limit shown on the plot. This suggests that the performance is optimum as it cannot exceed the diffraction limit.

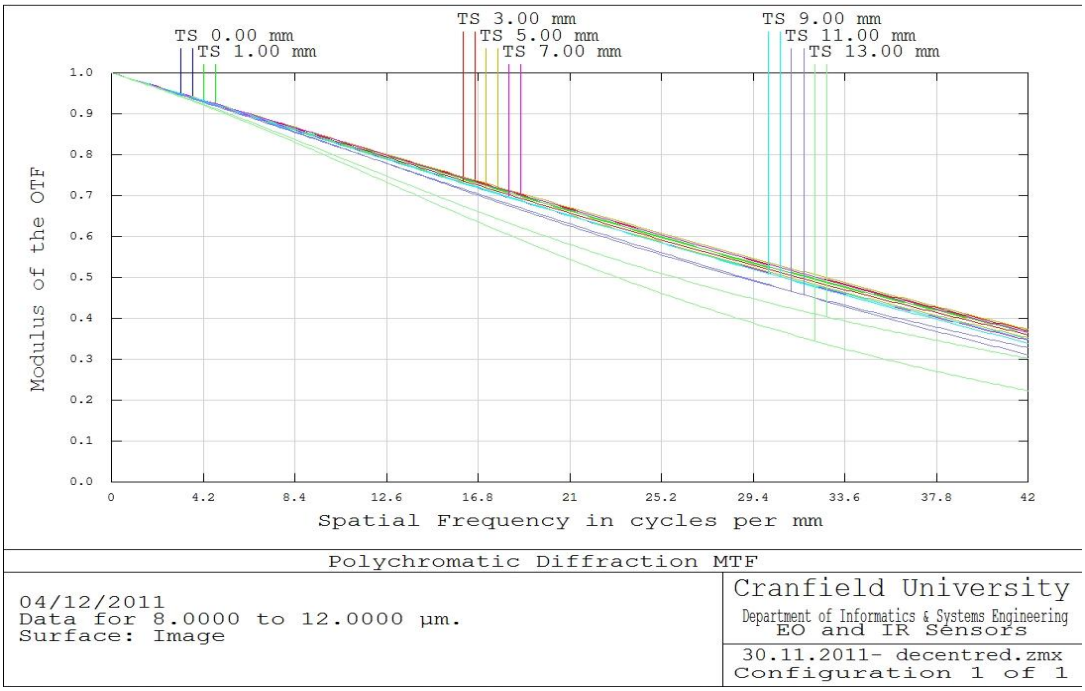

Figure 79 *– Optical MTF at 0mm and 13mm from origin, 8µm wavelength*

Figure 80 shows the relationship between angle of incidence with respect to the optical axis at the front surface of the system with the position of the spot it produces on the focal plane. This was determined by setting the field to be a particular image height from the centre of the focal plane and using the ray trace function in Zemax to find the angle of incidence at the first surface.

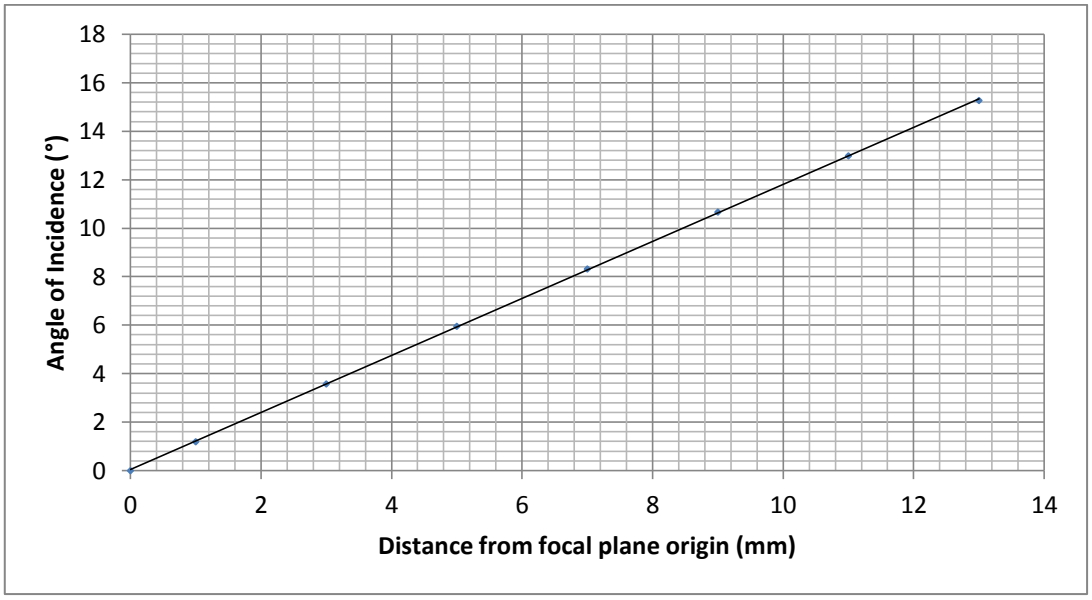

Figure 80 *– Graph showing the linear relationship between image height and angle of incidence*

3.7.3 Conclusion

- The performance of the on axis system is satisfactory in terms of optical MTF and spot radius according to the CPS issued by Sagem.
- Image height changes linearly with angle of incidence of radiation from the target.
- The curvatures and thicknesses of the lenses are realistic but may need to be altered slightly when taking in to account the tool sizes available from the manufacturer.
- All of the lenses in the system at this stage have spherical surfaces. By utilizing aspherical surfaces it may be possible to reduce the number of doublets in the system. This could make the design more cost effective.
- Thermal effects need to be taken in to account. Varying the temperature changes the back focal length of the system and so by analysing the changes in back focal length when there is change in temperature, it should be possible to move the focal plane along the z-axis to account for these thermal effects.

3.8 Athermalisation

Varying temperature has effects on the refractive properties of the lens materials in the system. The designs above were made at a temperature of 20°C. To analyse the effects of varying temperature the extreme temperature values have been chosen and the system has been re-optimised to change the back focal length only. This will ensure that lenses stay the same and only the distance between the back surface of the last lens and the focal plane can be changed, simulating the sensor moving in the z-plane to account for thermal effects. The spot diagrams and MTF data of the 0mm and 13mm fields are shown in ***Figure 81(a)-(c)*** and ***Figure 82(a)-(c)*** respectively. The original back focal length of the system at 20°C is 3.706378501 mm.

3.8.1 System Analysis 70°C

- Back focal length – 3.523467035mm

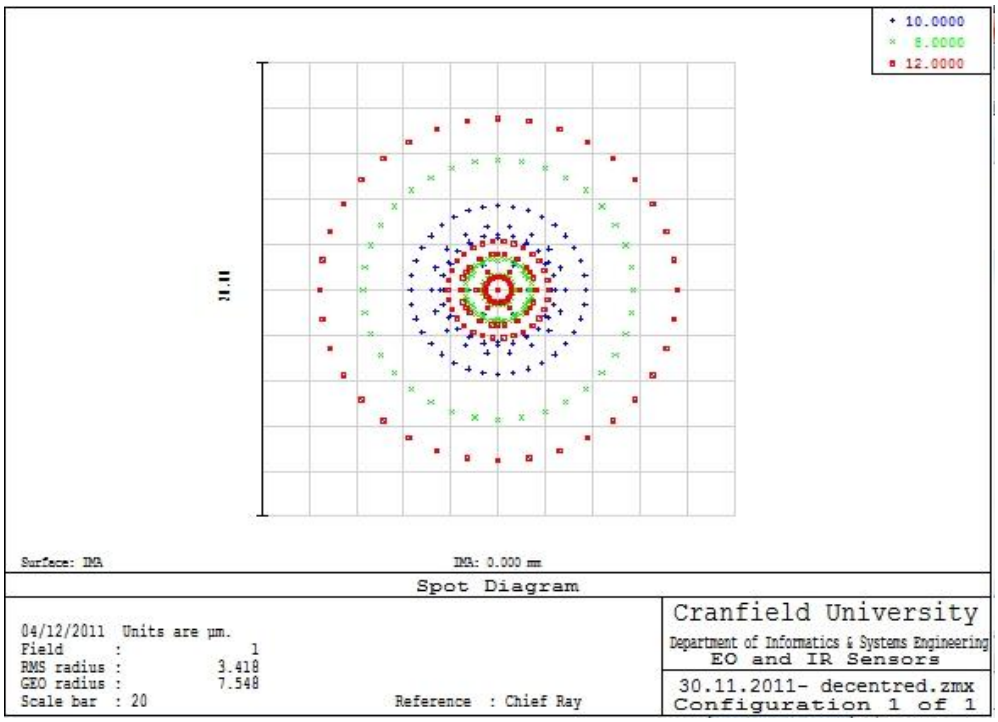

Figure 81(a) *– On axis spot diagram, 8-12 µm wavelength range, 70°C*

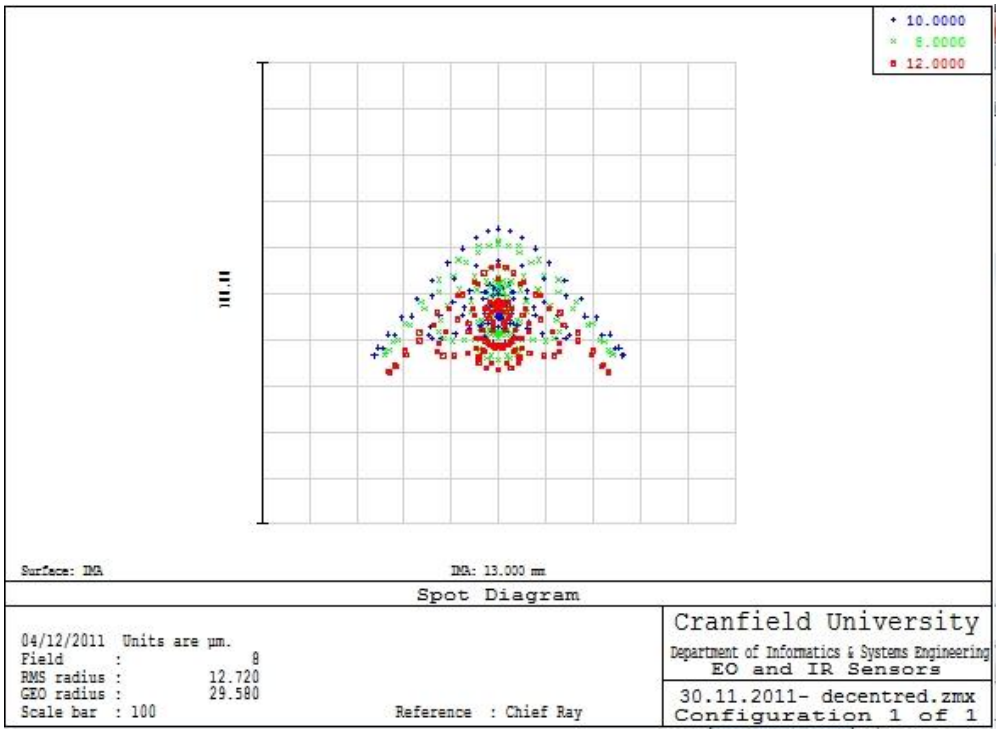

Figure 81(b) *– Spot at 13mm, 8-12 µm wavelength range, 70°C.*

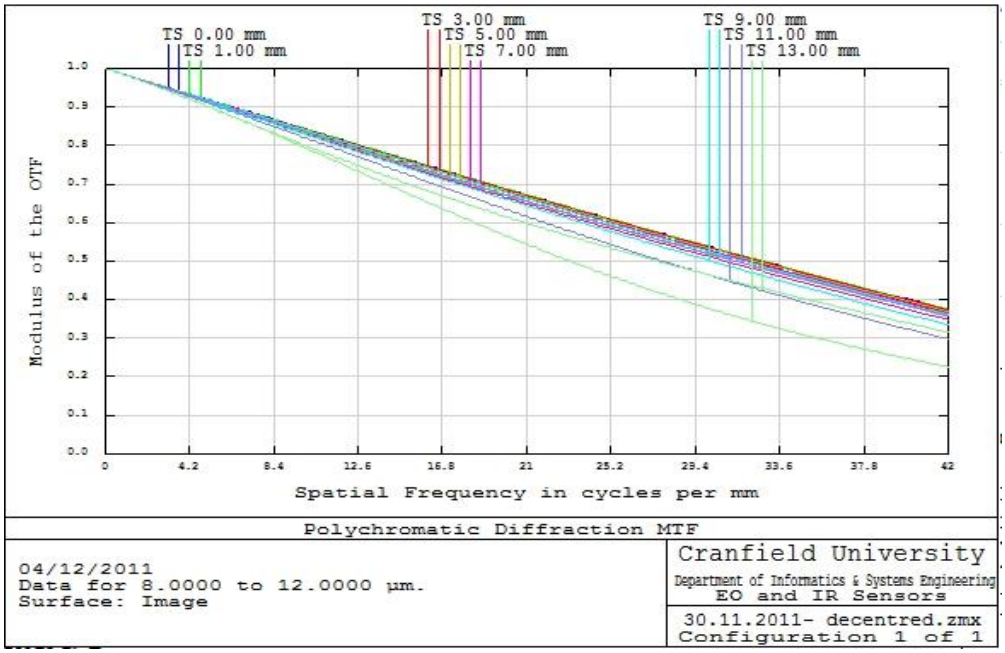

Figure 81(c) *– Optical MTF, 8-12µm wavelength, 70°C.*

3.8.2 System Analysis -40°C

- Back focal length – 3.928075231mm

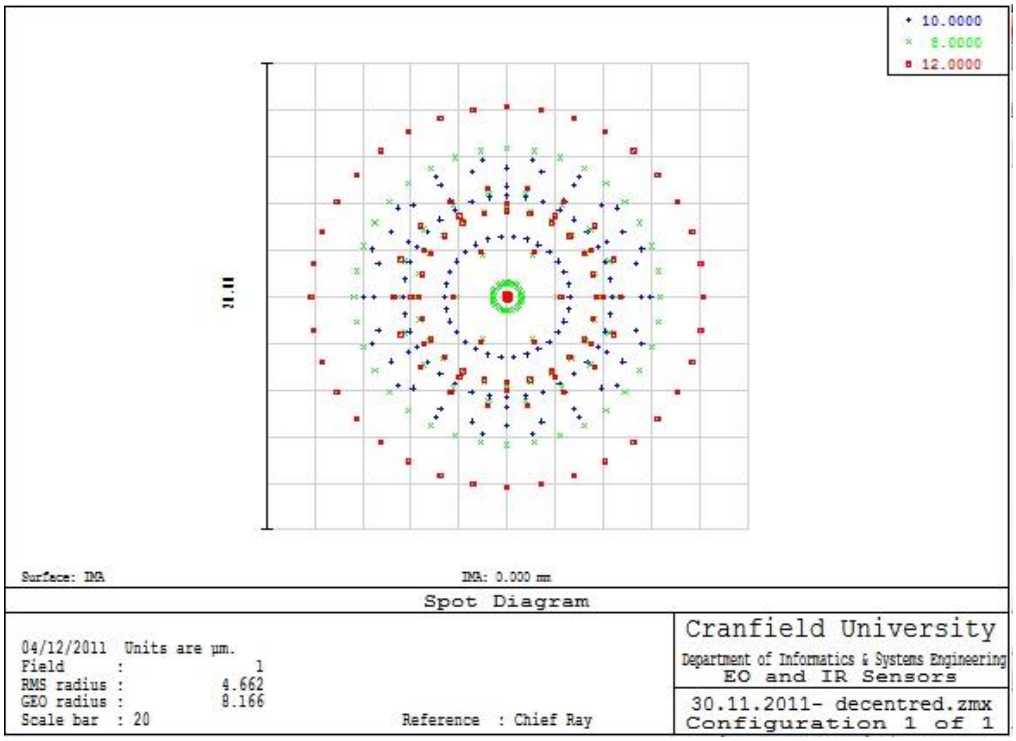

Figure 82(a) *– On axis spot diagram, 8-12 µm wavelength range, -40°C*

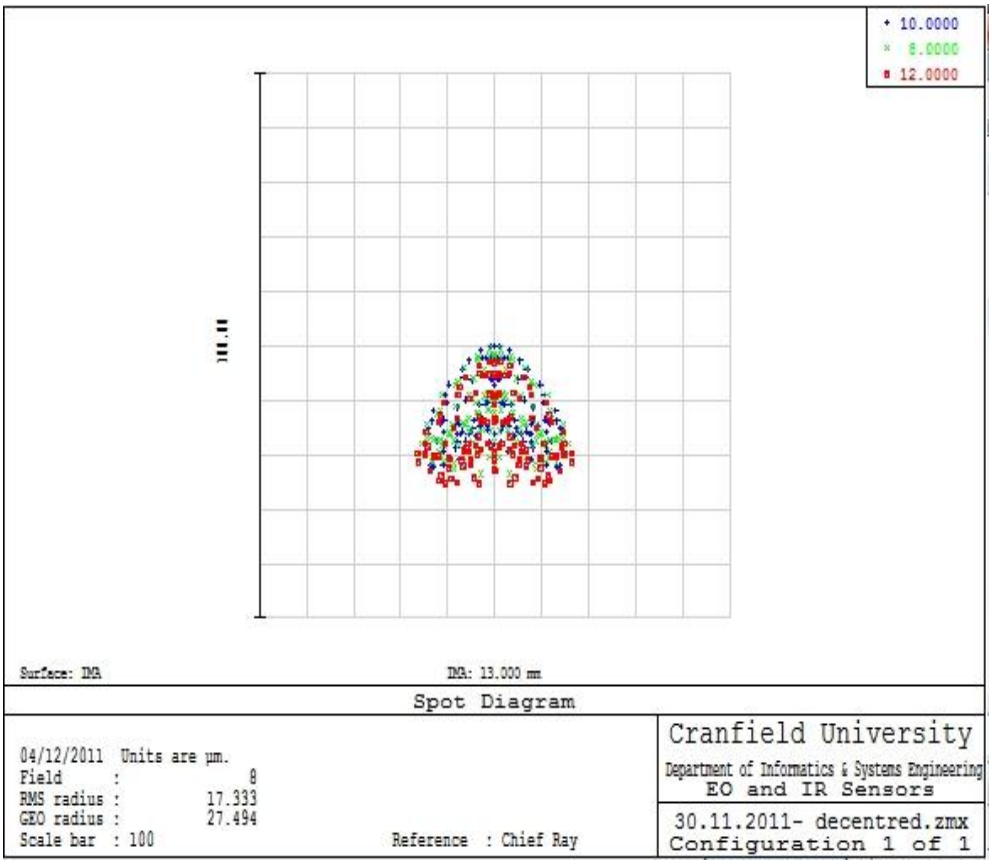

Figure 82(b) *– Spot at 13mm, 8-12 µm wavelength range, -40°C.*

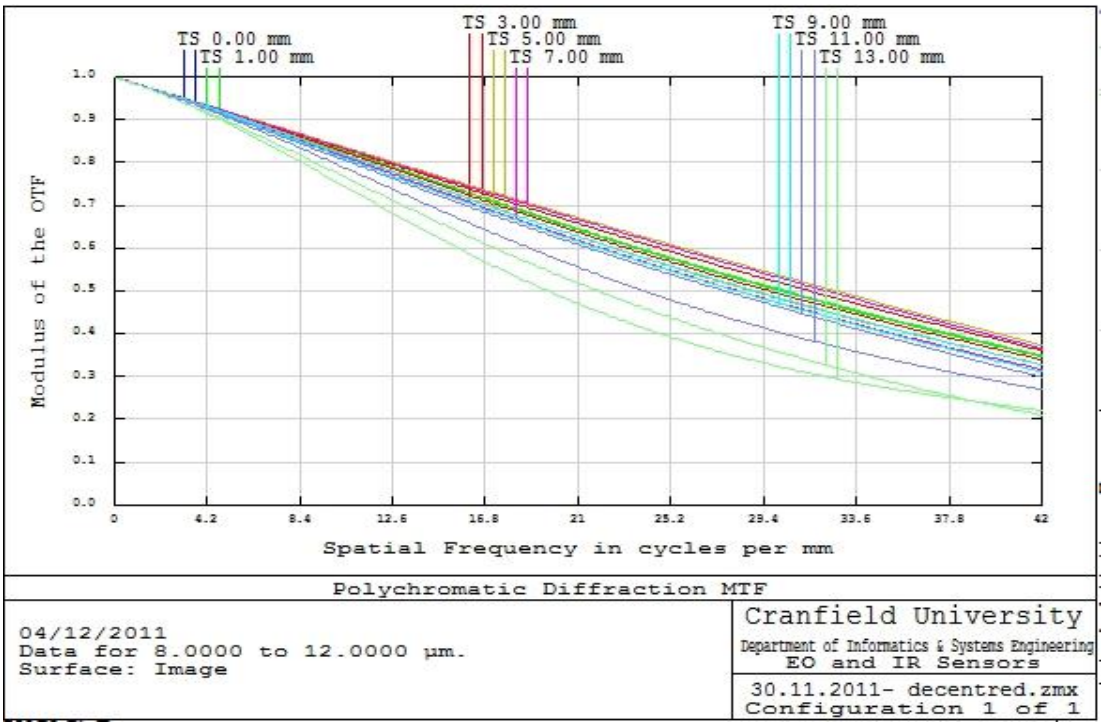

Figure 82(c) *– Optical MTF, 8-12µm wavelength, -40°C.*

By changing the temperature in 10^0 increments between the two extremes shown above a linear relationship is shown between the surrounding temperature and the back focal length of the system ***(Figure 83)***.

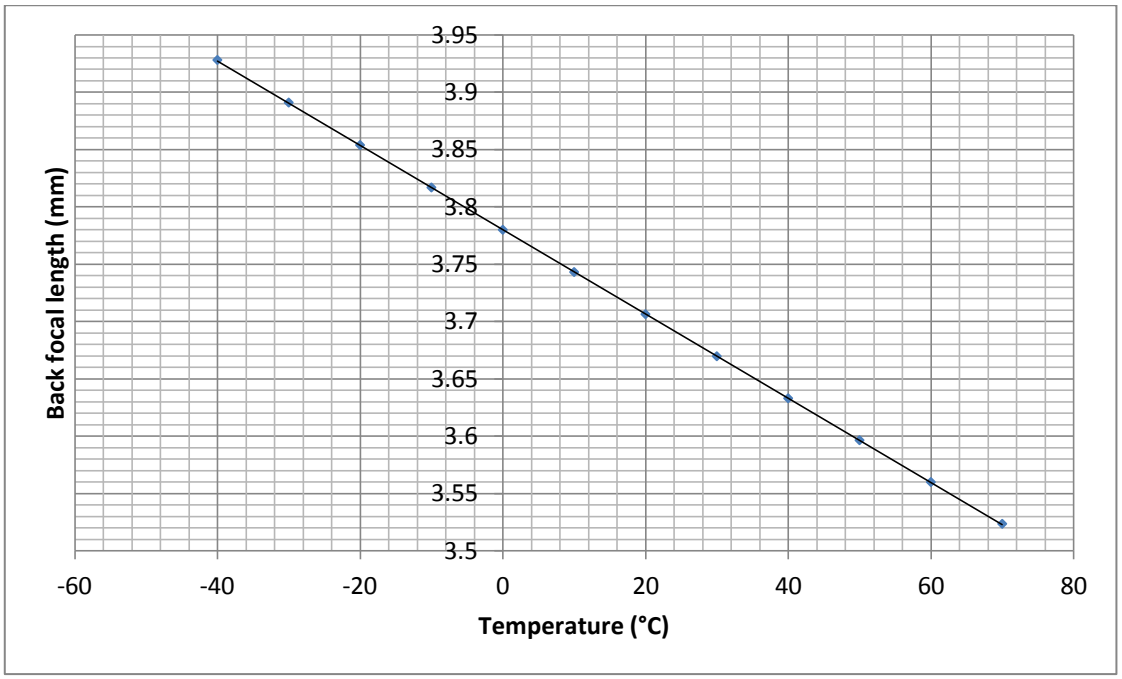

Figure 83 *– Graph to show the linear relationship between Back focal length and Temperature.*

3.8.3 Conclusion

- Changing the surrounding temperature of the system changes the refractive properties of the system and therefore the back focal distance of the system.
- The focal plane alone can be moved to the distance at which the lens system focuses. This distance varies linearly over the temperature range outlined in the CPS by ~0.5mm.
- The system is optimised for 20°C and so performs best at this temperature. **Figures 81** and **82** show that the performance in terms of optical MTF remains satisfactory however **Figures 81 (b)** and **82 (b**) show that the diameters of the spots at 13mm from the centre of the focal plane are larger than the desired 6µm RMS radius. The centre spots have slightly larger diameters than the desired diameter but indicate better performance than the edge performance as is expected.

3.9 Decentred Capabilities

It has been shown in the previous sections that a 30° field of view has been achieved. There are two main ways in which this field of view can be stabilised when imaging a moving target. One way to achieve this would be to move the image sensor itself to counteract the movement of the target as shown by current sensor based image stabilisation in photography. The other option is to keep the image sensor fixed and counteract the movement of the target by steering the incident light with other moving components such as lens groups. This may be advantageous over sensor based stabilisation in this project as there are electrical connections to the image sensor that may be affected by moving the sensor. In this section the lens based stabilisation capabilities of the above design will be determined by analysing the performance of the system when each lens is moved.

Figures 84(a) and ***84(b)*** show the effect of moving each lens on the RMS spot radius of the image at the centre of the focal plane. It is clear to see that as each lens is moved individually the performance quality of the system in terms of RMS spot size declines rapidly. At small distances it may be acceptable to determine the relationship to be linear but as shown in ***Figure 84(b)*** it is better described by a polynomial.

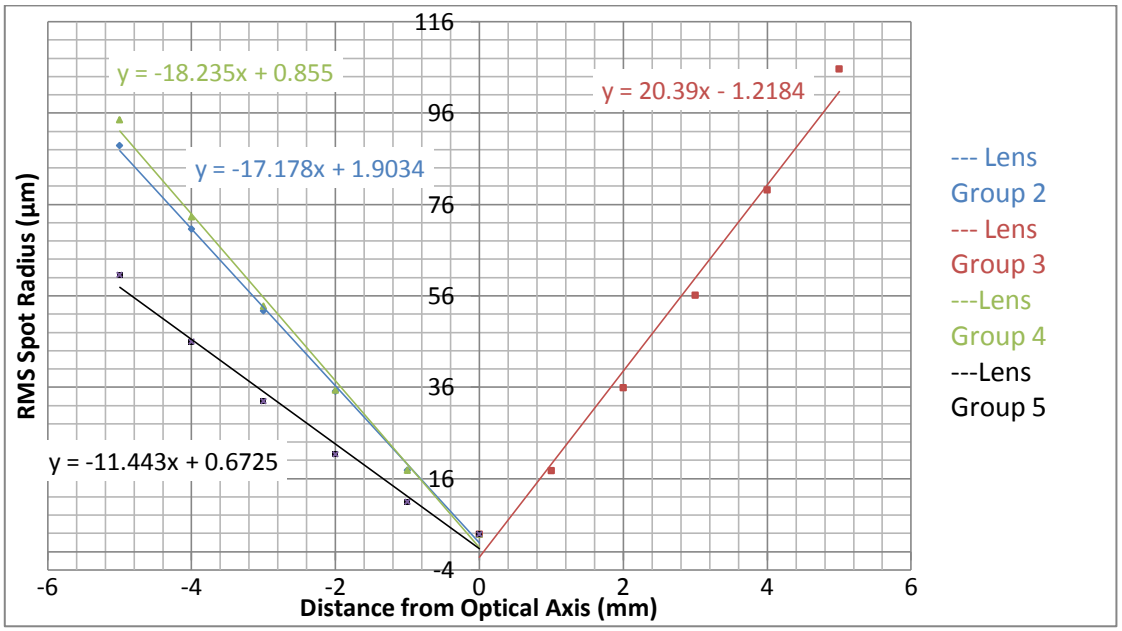

Figure 84(a) – *Graph to show the effects of moving each lens on the RMS spot radius with straight line fits*

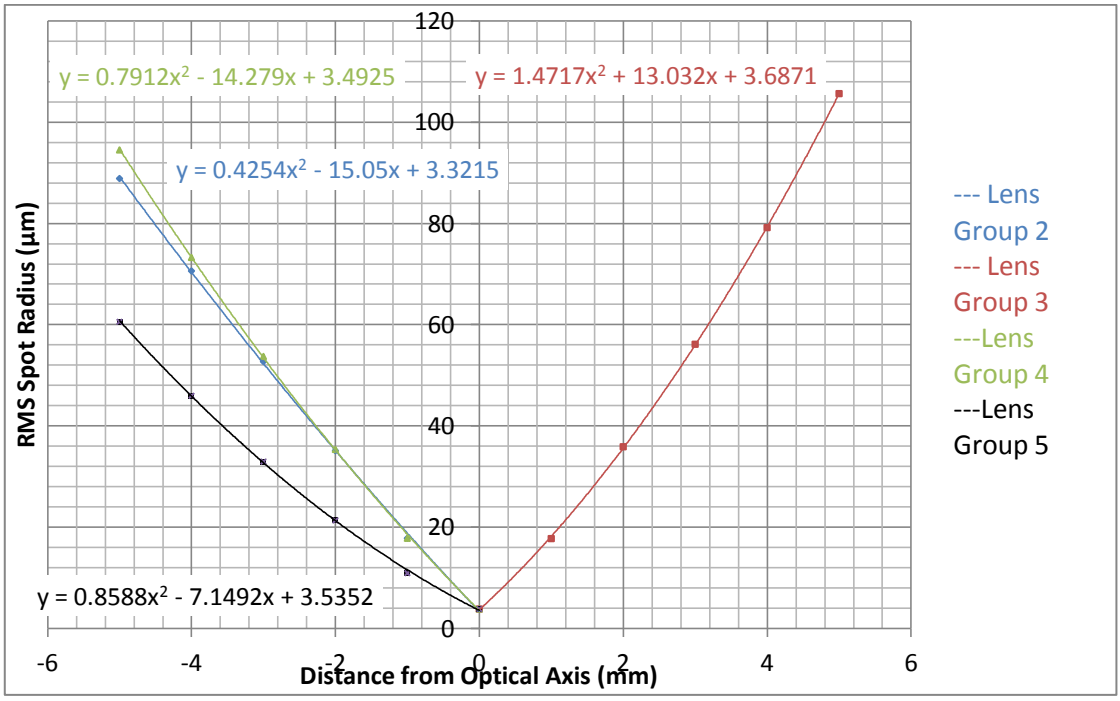

Figure 84(b) *– Graph to show the effects of moving each lens on the RMS spot radius with polynomial fits*

By setting the definition of 'field' to be image height and setting the image height as 0mm, ray traces have been used to determine the required movement of each lens group to achieve 7° correction. ***Table 5*** gives this information.

Lens Group	Distance from Optical Axis (mm)	Vignetting
2	12.5	YES
3	8.5	NO
4	10	NO
5	Can not achieve 7° correction by moving lens group 5	

Table 5 *–Magnitude of movement required by each lens group for required correction*

3.10 Conclusion

From the data shown in ***Table 5*** and by ***Figure 84(a)*** and ***Figure 84(b)*** it is clear that this design has no decentred capabilities. Therefore in order to achieve the required stabilisation for this project with this lens design the stabilisation would have to take place in the image sensor rather than the lens. The on axis design shows promise in terms of RMS spot sizes and MTF, however when considering the effects of temperature change on the back focal length there is a clear need to move the image sensor along the optical axis to maintain acceptable performance.

4. Zemax Optical Design 2

4.1 Design Basis

In this section the feasibility of achieving micro-stabilisation by adapting the decentred lens beam steering design developed by Jenifer L. Gibson *et al* has been further investigated**. [23]**. The initial design is intended as a steering system for an IR transmitter and receiver, with the second and third lenses moving from the optical axis providing the steering qualities (***Figure 24***). In this application the steering system would purely be used as a receiver. Since Zemax traces rays from left to right the geometry of the system has been reversed so that the first and second lenses move from the optical axis and the third lens stays fixed (***Figure 85***).

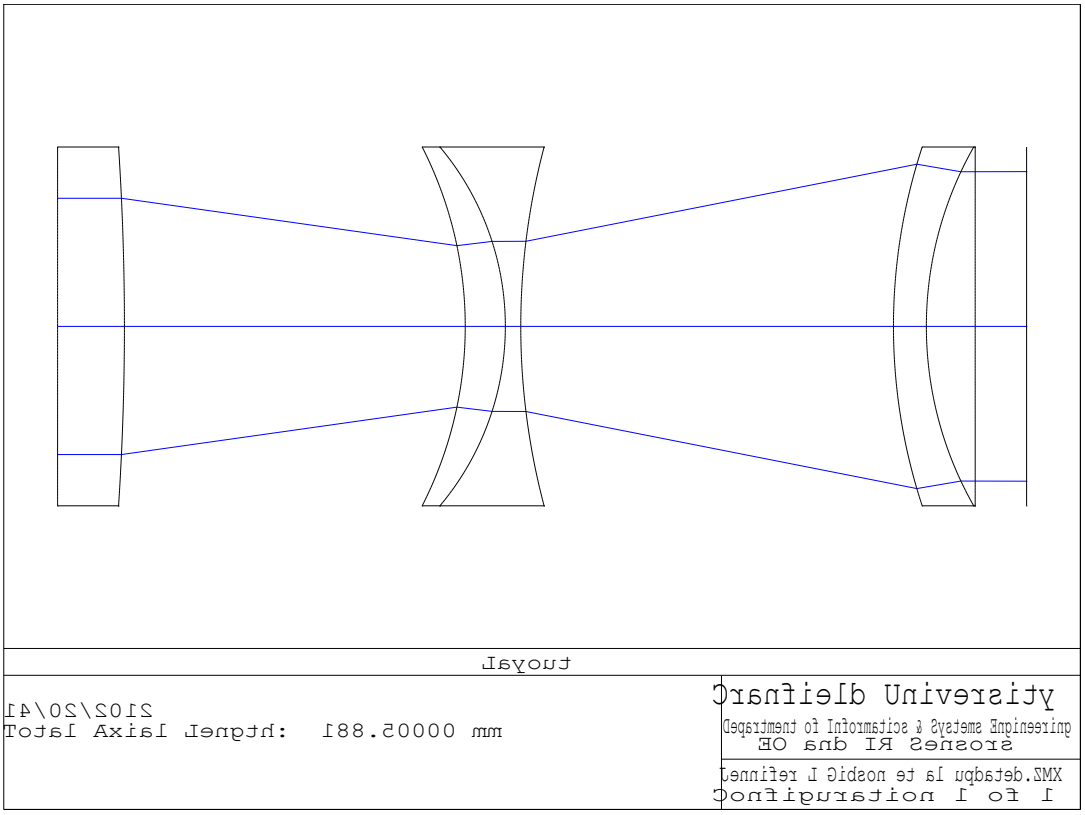

Figure 85 *– Reversed geometry development of the Jennifer L. Gibson et al beam steering system.*

4.1.1Things to be adjusted in this design

- Total length to be decreased to less than 150mm
- Fourth lens to be added to focus at the sensor
- Curvature of the rear surface of the complete system to be dictated by a 1.2 F-Number.
- Aperture dictated by the F-number and focal length. The focal length needs to be 48mm therefore aperture of 40mm is desired since:

$$\text{F-number} = f/d$$

- Optimise for multiple field points

4.2 Stage 1 Design Development

Figure 86 shows the layout of the beam steering device after it has been reduced in length to 120mm. The semi-diameter of the first lens has been increased to allow for a field of view of +/-5°. A plane surface has been added to the design in order to analyse the angle each ray leaves the rear surface of the exit lens. A value of 0 indicates that the ray lies 0° with respect to the normal of the surface. In this case with a plane surface it indicates that the ray lies 0° to the optical axis. In order to achieve this, the system has been optimised for angular radius at the plane surface behind the exiting surface of the beam steering device.

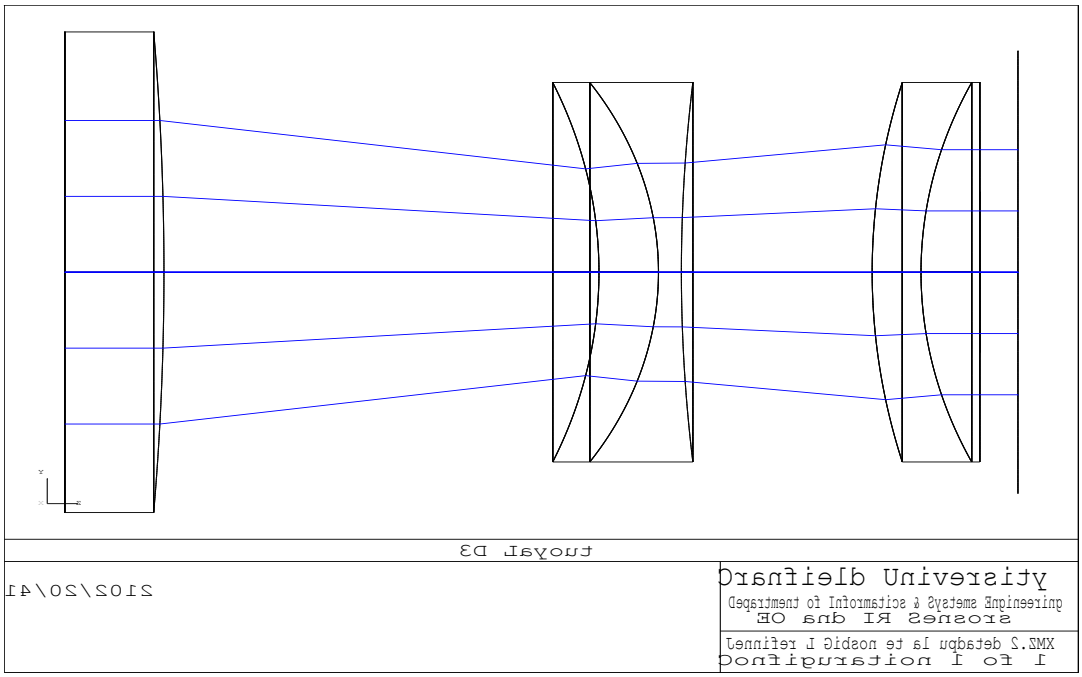

Figure 86 – *Updated design with track length of 120mm.*

4.2.1 On axis Analysis

The numbers listed in ***Figure 87 (a)-Figure 87 (e)*** represent the angle at which each of the 5 rays shown in ***Figure 86*** makes with the normal of each surface it is incident on. The bottom number each list is the angle that particular ray makes with the normal of the last surface in the design. The field in this scenario is determined by the angle between the object and the optical axis. In ***Figure 86*** above the field angle is 0°. In order for the on axis beam steering system to be satisfactory a target at 0° should give 0° exit rays. If this is the case then the bottom number in ***Figure 87 (a)-Figure 87 (e)*** should be zero.

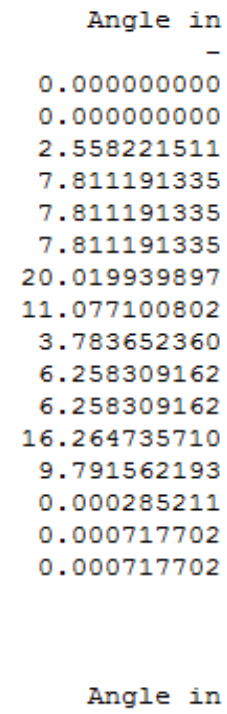

Figure 87(a) *- For Px=0, Py=1 (top ray) exit ray is 0.000717702° to the optical axis*

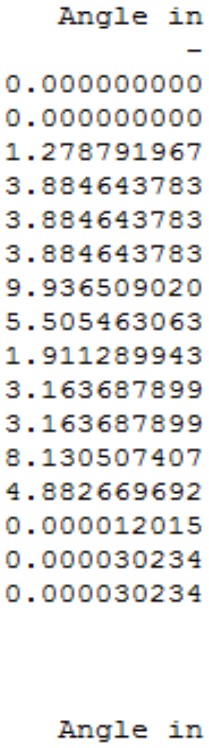

Figure 87(b) - For *Px=0, Py=0.5 (2nd Ray) exit ray is 0.000030234° to the optical axis*

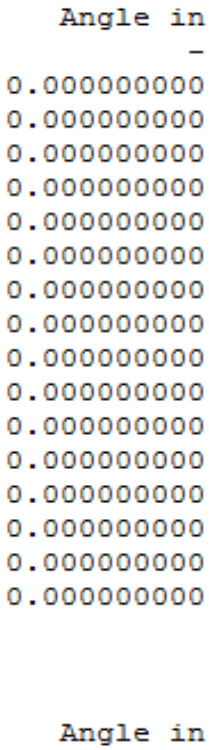

Figure 87(c) - *For Px=0, Py=0 (Central Ray) exit ray is 0° to the optical axis*

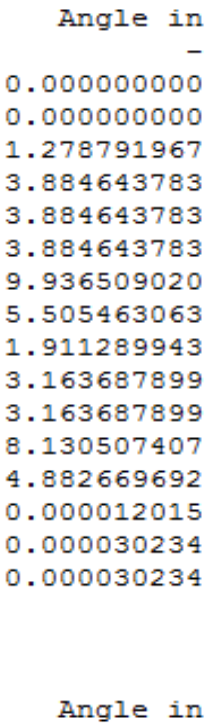

Figure 87(d) *- For Px=0, Py=-0.5 (3rd Ray) exit ray is 0.000030234° to the optical axis*

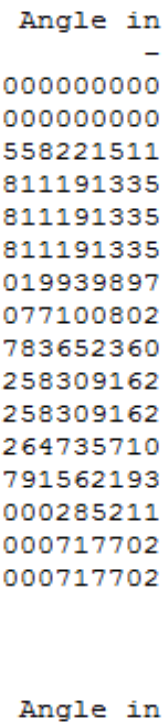

Figure 87(e) *- For Px=0, Py=-1 (bottom ray) exit ray is 0.000717702° to the optical axis*

The incident angles from the ray traces above show that the maximum angle between any of the rays and the rear plane surface for a 0° is 0.000717702°.

Figure 88 shows the layout of the beam steering device for a field of view of -5° in the y plane. Although only negative angles are shown here the positive angles would mirror the paths shown in ***Figure 88*** since the on axis system is symmetrical about the optical axis. Negative angles are shown here as Zemax chooses angles below the optical axis to be positive in the y plane, however lens displacement below the optical axis are negative. For this reason in this report it has been decided to label angles below the optical axis in the 'y' plane to be negative to maintain consistency in coordinates with respect to the displacement of lens elements.

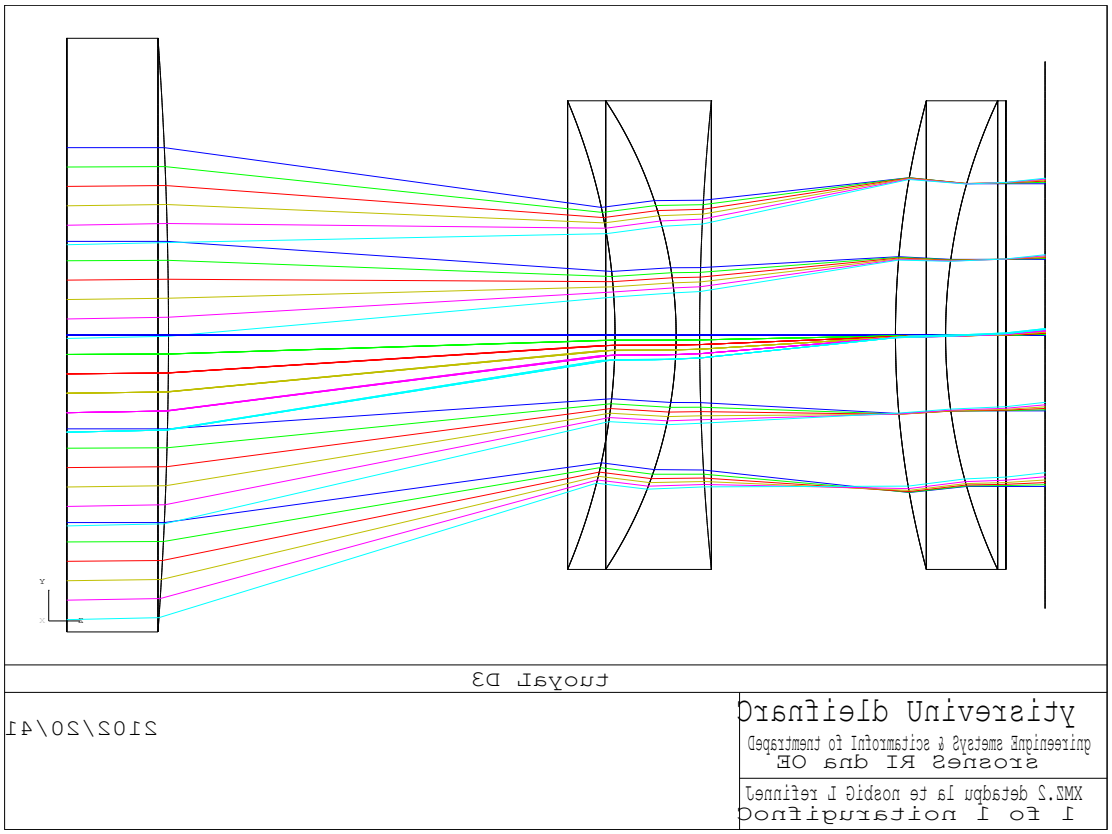

Figure 88 - On *axis beam steering device with -5° field of view in the y plane.*

Table 6 shows the field points in degrees and the corresponding angles that each ray makes with the normal of the plane surface at the rear of the beam steering device.

	Angle ray makes with optical axis when exiting the beam steering system in °					
Field (°)	**Py = 1**	**Py = 0.5**	**Py =0**	**Py = -0.5**	**Py = -1**	**Biggest difference in °**
0	-0.000187770	-0.000059573	0	0.000059573	0.000187770	0.00037554
-1	-1.234518577	-1.233908275	-1.235808803	-1.238633685	-1.244750215	0.01084194
-2	-2.462060619	-2.465744033	-2.474058744	-2.484428038	-2.502143513	0.040082894
-3	-3.684927262	-3.697848027	-3.717254635	-3.740271049	-3.775726340	0.090799078
-4	-4.905470239	-4.932607579	-4.968031711	-5.009293396	-5.069372434	0.163902195
-5	-6.125960004	-6.172455713	-6.229228695	-6.295034784	-6.387645316	0.261685312

Table 6 *– On axis field of view angles and the corresponding angles at which each ray exits the beam steering device*

The last column in ***Table 6*** shows that as the field angle increases, the exiting rays become less parallel. This indicates that when the plane surface at the rear of the beam steering device is replaced with a positive lens there will be a gradual decrease in image quality at points further from the centre of the focal plane.

4.2.2 Decentered Analysis

In order to stabilise an image as it moves relative to the x and y planes the lenses in the beam steering device move to keep the incident rays focused on the same point of the detector. If the target is at 0° to begin with and then moves through -5° the rays exiting the device are at 6.1° to 6.4° angles. To return these angles to approximately zero the first lens has been displaced by 8.25mm in the direction of movement of the target and the second lens by 4.125mm in the opposite direction (***Figure 89***).Since the on axis system is symmetrical in x and y planes the magnitude of these values would be the same for correction of 5° in any direction.

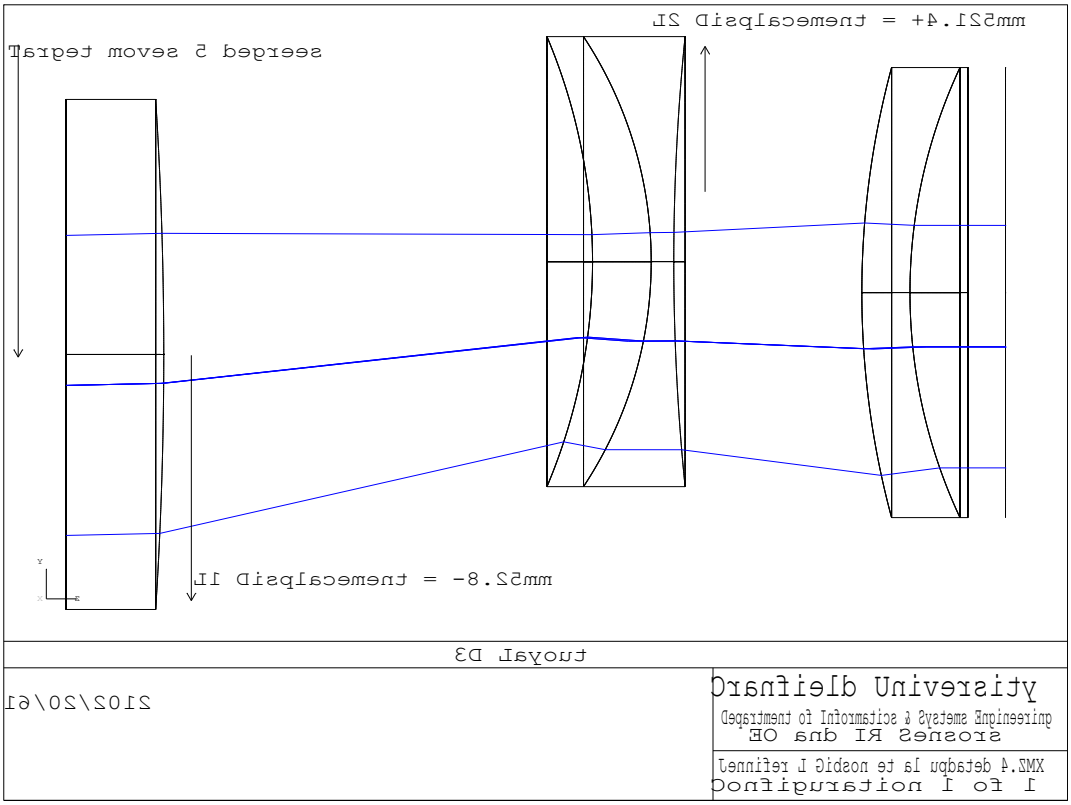

Figure 89 *– 2D layout showing movement of lenses 1 and 2 in order to correct 5° motion of the target.*

Table 7 shows the required displacements of lens 1 and lens 2 in order to achieve approximately 0° exit rays when the target is at increments of 1° with respect to the front surface of the beam steering device.

			Angle of incidence at plane surface°				
Field (°)	L1 Displacement (mm)	L2 Displacement (mm)	Py = 1	Py = 0.5	Py = 0	Py = -0.5	Py = -1
0		-	-0.000187770	-0.000059573	0	0.000059573	0.000187770
1	-1.640	0.820	0.000204763	0.001221548	0.001224194	0.001409148	0.001306381
2	-3.280	1.640	0.000985931	0.002552137	0.003092819	0.003490840	0.004459308
3	-4.920	2.460	0.002535621	0.004636168	0.006206170	0.006245524	0.011291396
4	-6.550	3.275	0.002418858	0.000578210	0.003528177	0.001844071	0.032008878
5	-8.250	4.125	0.046934683	0.051366312	0.055758095	0.049744346	0.011245350

***Table 7** - Lens displacements required for 0° exit rays*

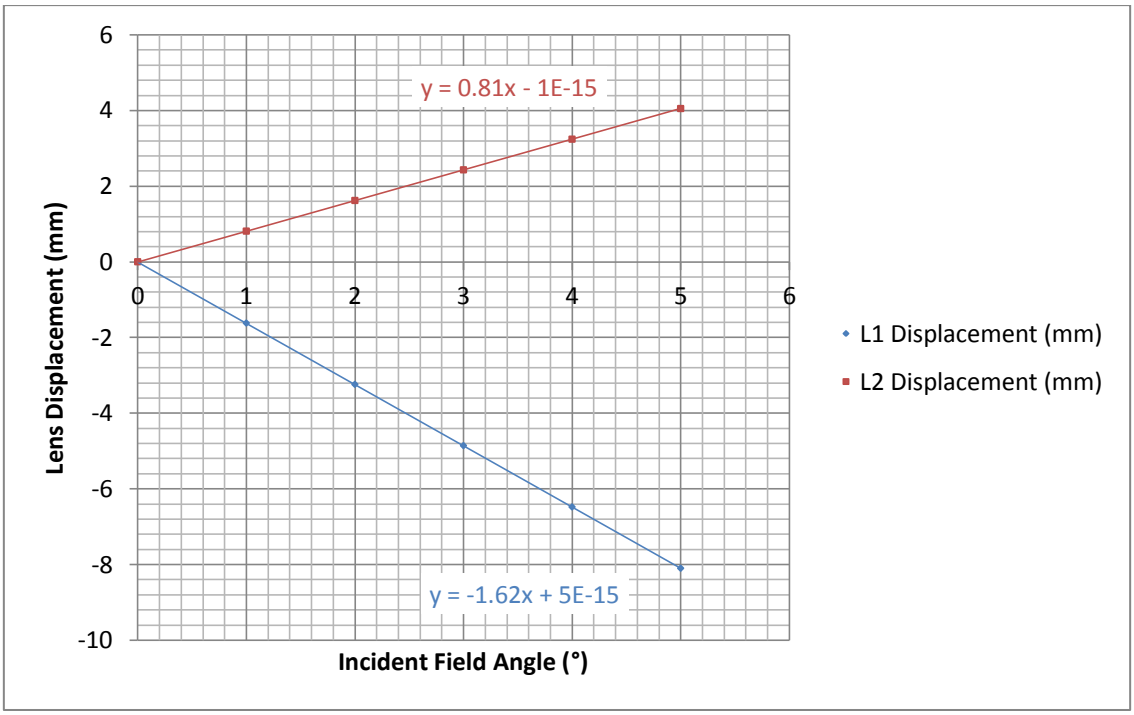

***Figure 90** – Graph showing the linear relationship between incident angle and the required lens displacements in order to achieve parallel light exiting the beam steering device parallel to the optical axis.*

4.3 Stage 2 Design Development

In order to focus the rays from the beam steering device on to the detector two more doublets have been added to the design. This has increased the overall length of the design making it longer than the desired maximum length, however with only one extra lens the performance of the system is poor, and so there is a trade off between dimensions of the system, the amount of lenses in the system and the quality of the performance. The on axis system is shown in ***Figure 91*.**

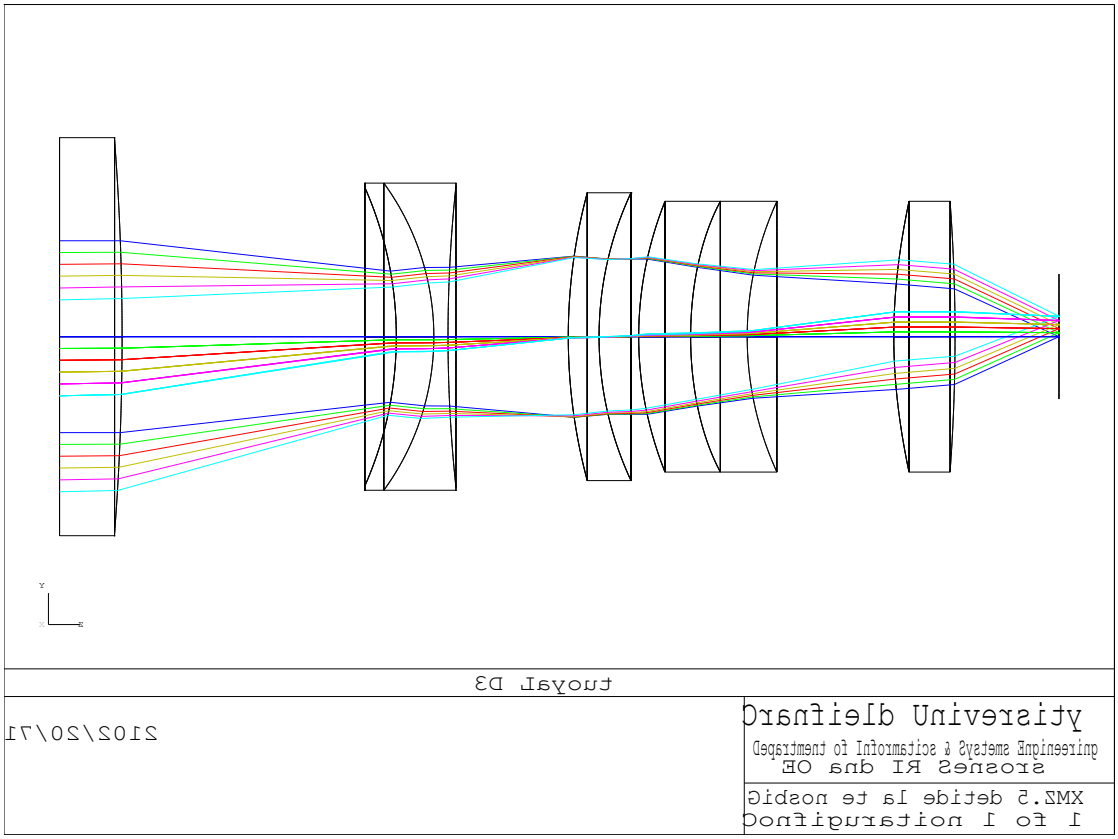

Figure 91 *– On axis system with ±5° field of view*

4.3.1On Axis System Analysis

Spot diagrams for the on axis field of view are shown in ***Figure 92***. Every different angle of incidence creates a different image at a different position on the focal plane. By defining the field as the angle of incidence with the first surface, and increasing this value from 0° to -5° in increments of -1°, the 5 images in ***Figure 92*** are formed at the distances specified under each image. ***Table 8*** shows the angles of incidence for the on axis system and the corresponding distances from the centre of the focal plane at which the images form.

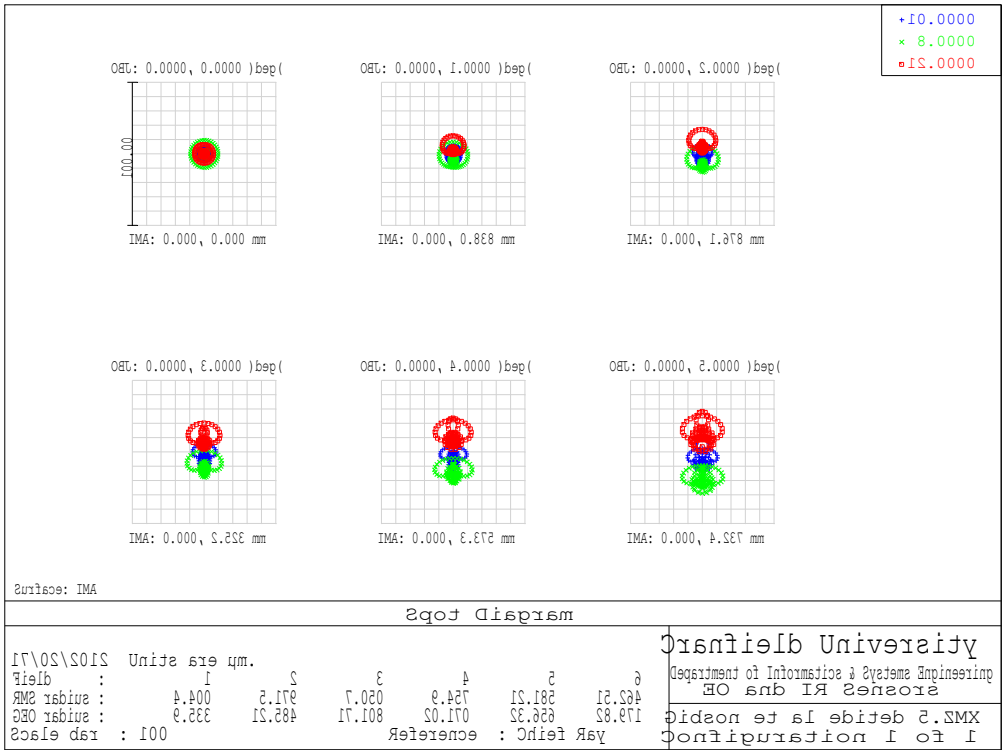

Figure 92 *– On axis spot diagrams*

Field (°)	Focal Plane Distance (mm)
-5	4.237
-4	3.375
-3	2.523
-2	1.678
-1	0.838
0	0
1	-0.838
2	-1.678
3	-2.523
4	-3.375
5	-4.237

Table 8 *– On axis field angles and corresponding distances of image formed from the centre of the sensor in the y plane.*

Figure 93 Is a graph showing the linear relationship between the on axis field angles and the image distances shown in ***Table 8***.

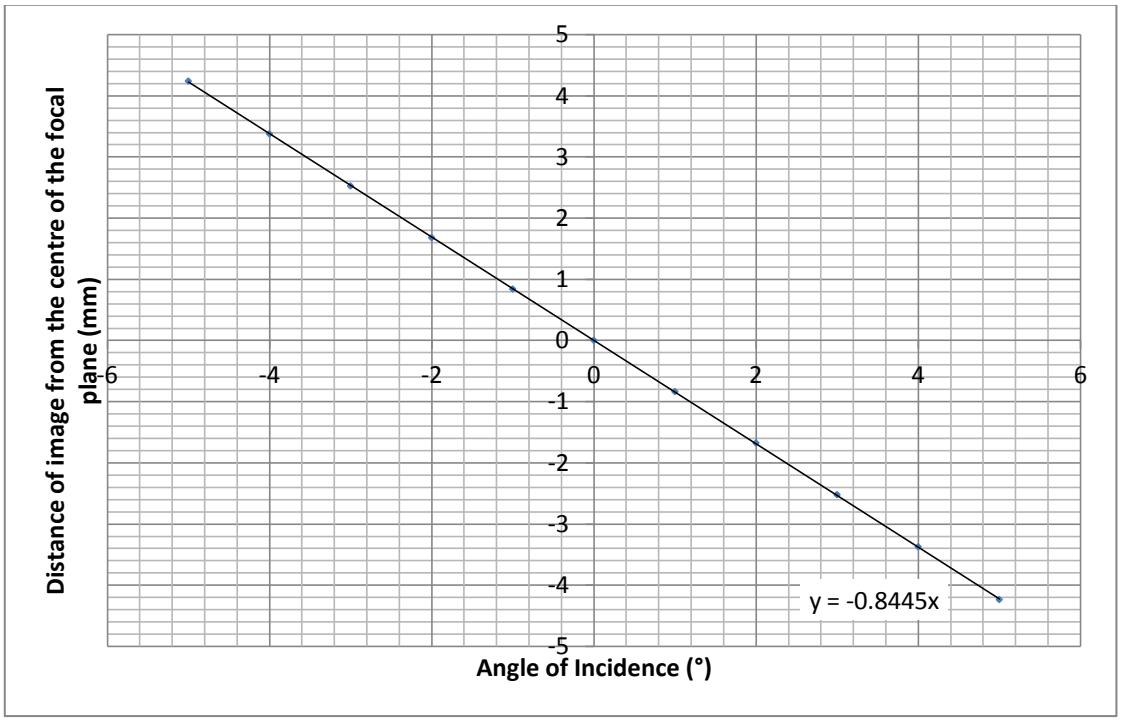

Figure 93*- Graph showing the linear relationship between on axis field angles and distance of image from the centre of the focal plane.*

The MTF's for the on axis design are shown in ***Figure 94***. It is clear from this that the sagittal responses are better than the tangential responses. The reasoning for this could be explained by the spot diagrams for these field points. As the field angle increases there becomes a larger spot radius in the tangential plane than the sagittal plane. The black line in ***Figure 94*** indicates the limit in performance due to the occurrence of diffraction. The sagittal responses all follow close to the diffraction limit indicating that the sagittal performance is close to the limit. All sagittal responses meet the requirement of 20% at 42 cycles per mm outlined in the subsystem specification.

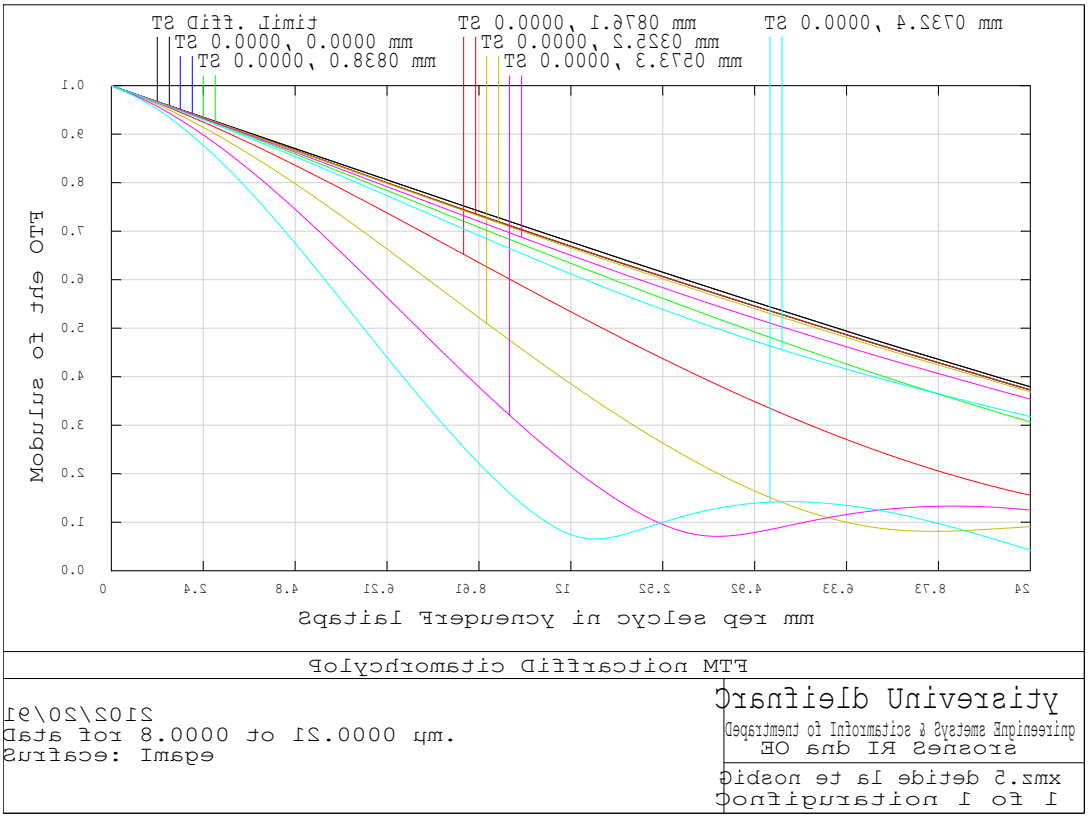

Figure 94 *– Diffraction MTF for on axis field of view*

4.3.2 Decentered System Analysis

By changing the definition of field to be the distance of image from the centre of the focal plane it has been made possible to move the front two lenses in the system while still analysing the images formed at the distances specified in ***Table 8.*** With the distance at which the image is formed from the centre of the focal plane fixed, moving the lenses in the system causes a change in angle of incidence at the front of the system. By using the ray trace function in Zemax the optimum distances of lens movement have been determined. These lens displacements achieve incident angles of 0°, -1°, -2°, -3°, -4° and-5° and form images at the centre of the focal plane. The magnitude of these lens movements are shown in ***Table 9***, and a graph showing the relationship between these values is shown in ***Figure 95***. In order to achieve positive incident angles the lens displacements would need to have the same magnitude but in the opposite direction. This is shown in by the graph in ***Figure 95***.

Angle of Incidence (°)	L1 Displacement (mm)	L2 Displacement (mm)
0	-	-
-1	-1.64	0.82
-2	-3.28	1.64
-3	-4.91	2.455
-4	-6.55	3.275
-5	-8.18	4.09

Table 9 *– Movements required by each lens to form an image at the centre of the focal plane with the specified angle of incidence*

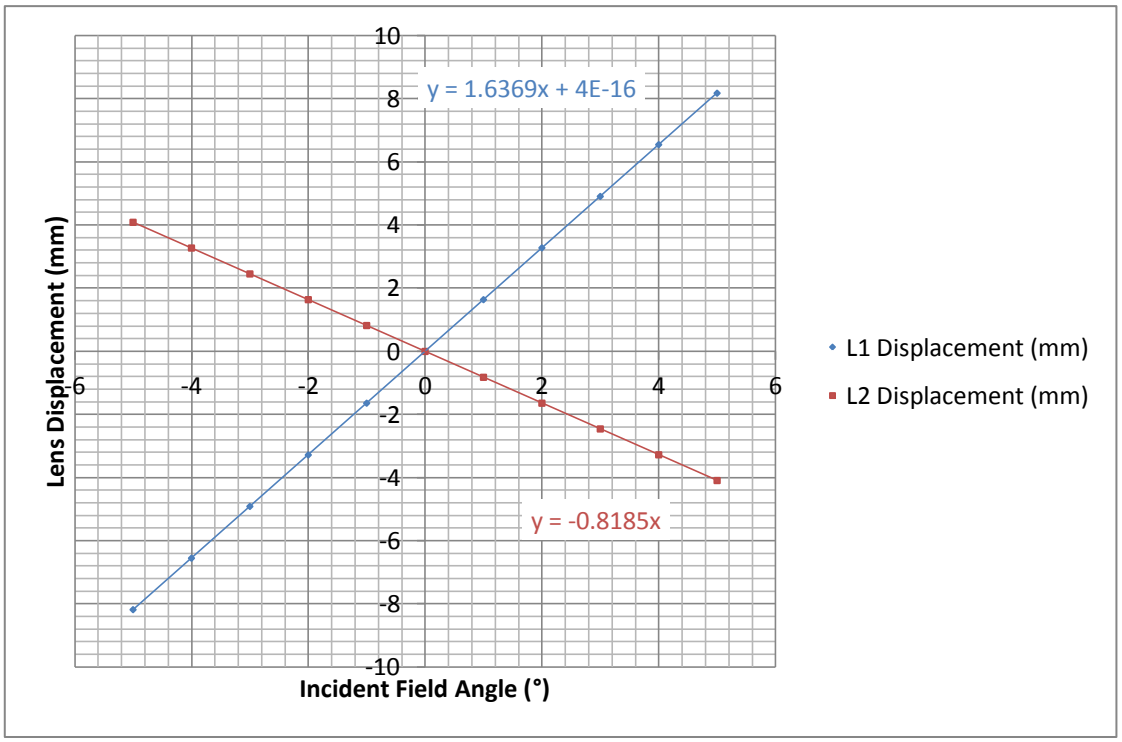

Figure 95 *- Graph showing the required displacements of lenses 1 and 2 to achieve ± 5° of image stabilisation in the y plane at the centre of the image sensor.*

Figure 96 shows the layout of the system with maximum decentre achieving maximum steering in the y plane. The spot diagrams and diffraction MTF's for the system at maximum decentre are shown in ***Figure 97*** and ***Figure 98*** respectively**.**

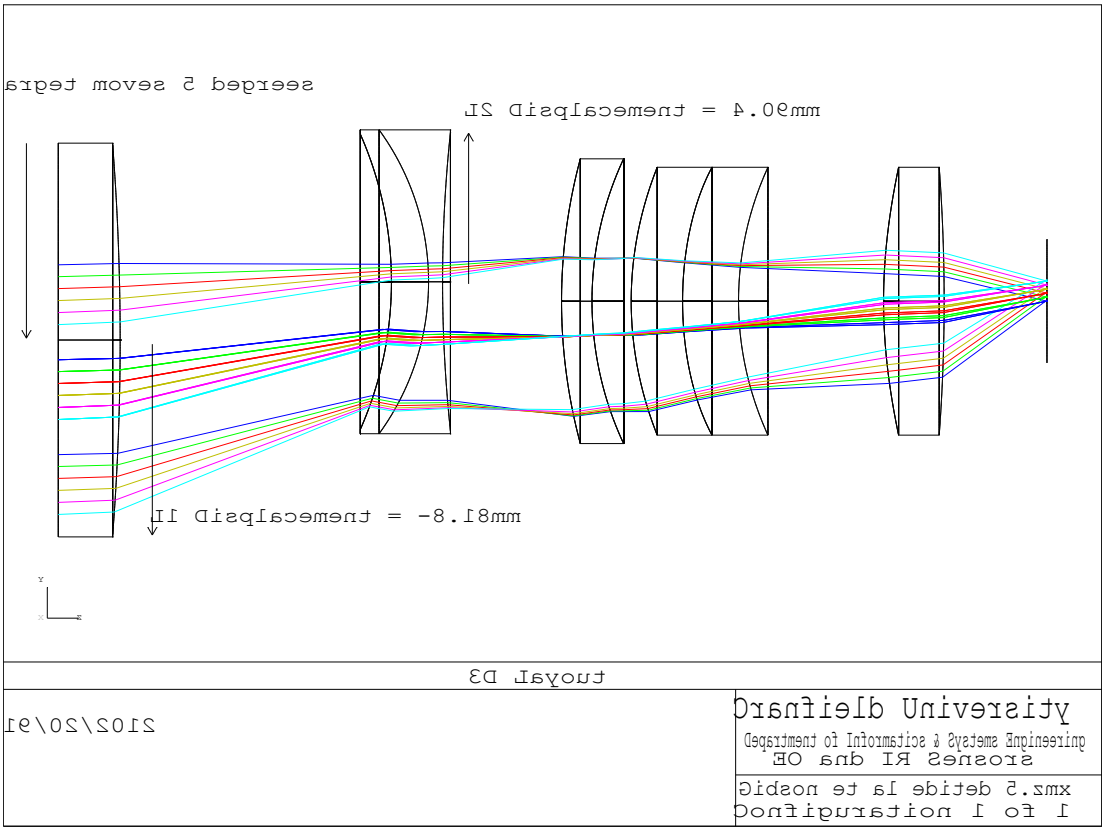

Figure 96 *– Design layout showing lens movements for 5° correction in the -y direction*

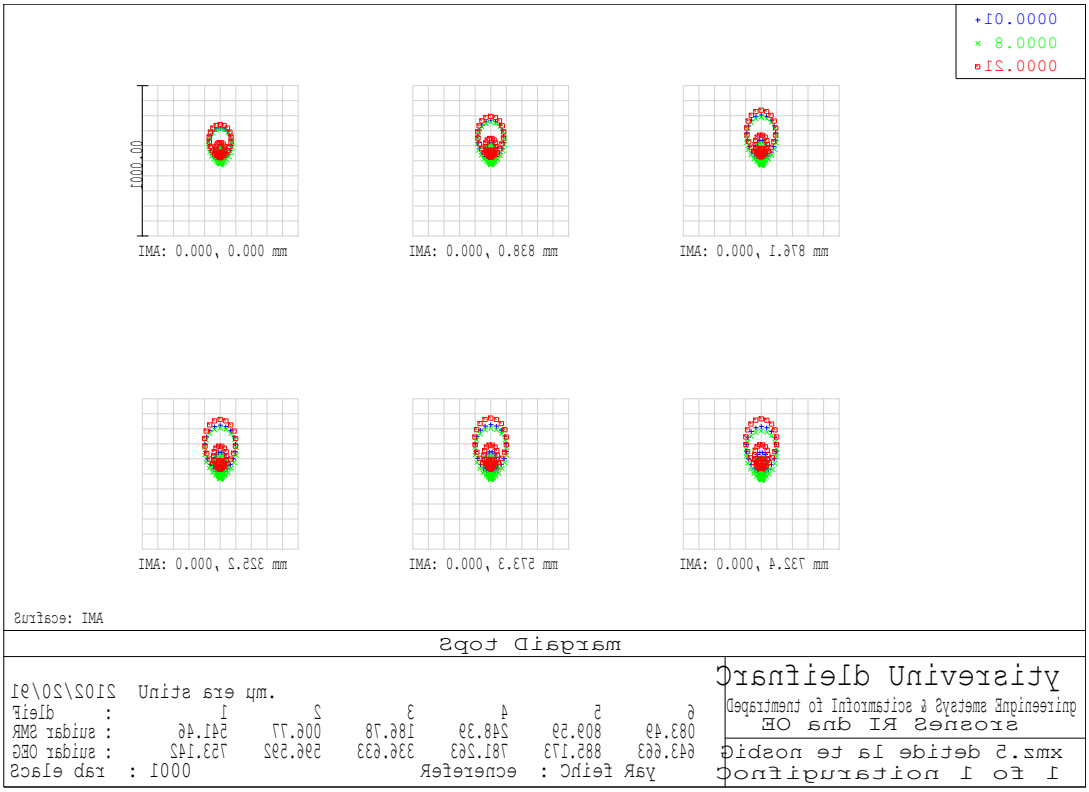

Figure 97 *– Spot diagrams for maximum decentred system*

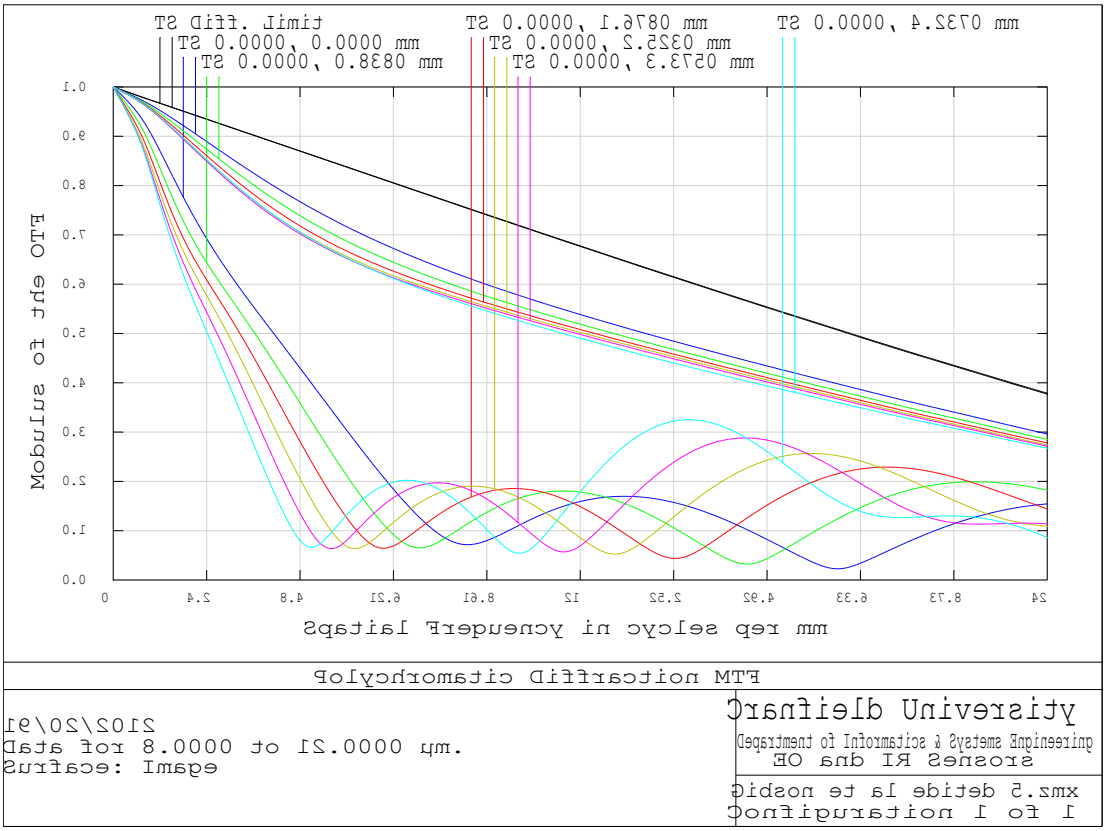

Figure 98 *– Diffraction MTF for maximum decentred field of view.*

The spot sizes shown in ***Figure 97*** and diffraction MTF's shown in ***Figure 98*** Show that the system performance does not meet the requirements of this project. The sagittal response of the diffraction MTF are still acceptable however the tangential response has become worse with increase in lens displacement. The performance with respect to spot radius and diffraction MTF may be improved with the addition of further lenses to the system, however this would result in a decrease of throughput and also would increase the length of the system.

Table 10(a) gives details on the RMS spot radius at different target positions in the y plane. The effects on the RMS spot radius in the x plane and xy plane when the system is decentered to correct for target movement in the y plane are shown in ***Table 10(b)*** *and* ***Table 10(c)***. The extreme distances from the centre of the image sensor have been highlighted in the ***Tables 10(a-c)***. ***Figure 99*** is a diagram indicating where these points are on a circular focal plane.

	Distance of image from the centre of the focal plane (mm)										
Target Position (y)(°)	**(-) 4.237 (y)**	**(-) 3.375 (y)**	**(-) 2.523 (y)**	**(-) 1.678 (y)**	**(-) 0.838 (y)**	**0**	**0.838 (y)**	**1.678 (y)**	**2.523 (y)**	**3.375 (y)**	**4.237 (y)**
	RMS Spot radius of image (μm)										
0	15.266	12.186	9.457	7.049	5.179	4.4	5.179	7.049	9.457	12.186	15.266
-1	12.713	9.33	6.312	4.469	5.112	7.332	9.827	12.211	14.474	16.786	19.496
-2	12.791	8.193	4.784	5.864	9.853	14.041	17.738	20.727	23.008	24.812	26.69
-3	16.751	9.422	5.786	10.77	17.827	24.492	30.136	34.433	37.262	38.775	39.569
-4	24.195	12.475	9.07	18.725	30.066	40.525	49.306	55.893	59.986	61.596	61.282
-5	34.715	16.513	14.196	30.502	48.096	64.145	77.6	87.681	93.842	95.908	94.38

Table 10(a) *– RMS spot radius of spots formed at 0mm, ±0.838mm, ±1.678mm, ±2.523mm, ±3.375mm and ±4.237mmin the y plane with 1° increments in incident angle.*

	Distance of image from the centre of the focal plane (mm)										
Target Position (y)(°)	**(-) 4.237 (x)**	**(-) 3.375 (x)**	**(-) 2.523 (x)**	**(-) 1.678 (x)**	**(-) 0.838 (x)**	**0**	**0.838 (x)**	**1.678 (x)**	**2.523 (x)**	**3.375 (x)**	**4.237 (x)**
	RMS Spot radius of image (μm)										
0	15.266	12.186	9.457	7.049	5.179	4.4	5.179	7.049	9.457	12.186	15.266
-1	16.224	13.419	11.059	9.135	7.814	7.332	7.814	9.135	11.059	13.419	16.224
-2	19.597	17.574	16.053	14.948	14.27	14.041	14.27	14.948	16.053	17.574	19.597
-3	26.69	25.775	25.193	24.803	24.57	24.492	24.57	24.803	25.193	25.775	26.69
-4	39.433	39.768	40.113	40.345	40.485	40.525	40.485	40.345	40.113	39.768	39.433
-5	59.748	61.397	62.67	63.521	63.995	64.145	63.995	63.521	62.67	61.397	59.748

Table 10(b) *– RMS spot radius of spots formed at 0mm, ±0.838mm, ±1.678mm, ±2.523mm, ±3.375mm and ±4.237mm in the x plane with 1° increments in incident angle.*

	Distance of image from the centre of the focal plane (mm)										
Target Position (y)(°)	**(-) 2.996 (x&y)**	**(-) 2.401 (x&y)**	**(-) 1.790 (x&y)**	**(-) 1.189 (x&y)**	**(-) 0.593 (x&y)**	**0**	**0.593 (x&y)**	**1.189 (x&y)**	**1.790 (x&y)**	**2.401 (x&y)**	**2.996 (x&y)**
	RMS Spot radius of image (µm)										
0	15.266	12.255	9.483	7.059	5.18	4.4	5.18	7.059	9.483	12.255	15.266
-1	13.714	10.672	7.963	6.184	6.023	7.332	9.282	11.402	13.584	15.935	18.599
-2	14.155	11.093	9.145	9.301	11.296	14.041	16.79	19.214	21.237	23.022	24.904
-3	17.033	13.779	13.208	15.76	19.967	24.492	28.6	31.902	34.226	35.652	36.572
-4	22.33	18.863	20.438	26.105	33.324	40.525	46.862	51.81	55.046	56.511	56.551
-5	29.976	35.405	26.621	31.517	41.528	64.145	73.828	81.357	86.21	88.144	87.421

Table 10(c) *– RMS spot radius of spots formed at 0mm, ±0.593mm, ±1.189mm, ±1.790mm, ±2.401mm and ±2.996mm in the xy plane with 1° increments in incident angle.*

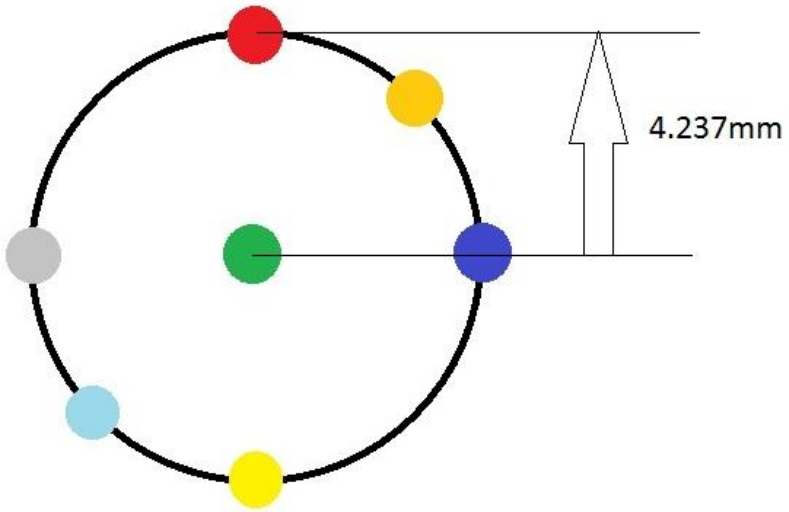

Figure 99 *– Image to show the positions of the spots highlighted in* ***Tables 10 (a-c)****.*

4.4 Athermalisation

Due to thermal effects, varying the temperature of the surroundings changes the back focal length of the system. In order to overcome this one option is to vary the distance between the back surface of the last lens and the detector. The specification for this project suggests that the device would need to work over a range of -40°C to +70°C. By changing the surrounding temperature in the environmental tab of Zemax, and re-optimising for RMS spot radius the distance between the last lens and the detector was determined. By specifying that only this distance is variable ensures that the rest of the design is unchanged. The temperature was changed in increments of 10° and re-optimised. The determined changes to back focal length are described by ***Table 11***. ***Figure 100*** shows that there is a linear relationship between the surrounding temperature and the back focal length of the design.

Temperature (°C)	Back Focal Length (mm)	Total Track Length (mm)
-40	21.99161066	208.1274960951
-30	21.92657982	208.0624652551
-20	21.86160866	207.9974940951
-10	21.79671936	207.9326047951
0	21.73186883	207.8677542651
10	21.6670716	207.8029570351
20	21.60138132	207.7372667551
30	21.53762604	207.6735114751
40	21.47297361	207.6088590451
50	21.40834544	207.5442308751
60	21.34379045	207.4796758851
70	21.27928929	207.4151747251

Table 11 *– Change in back focal length with varying temperature*

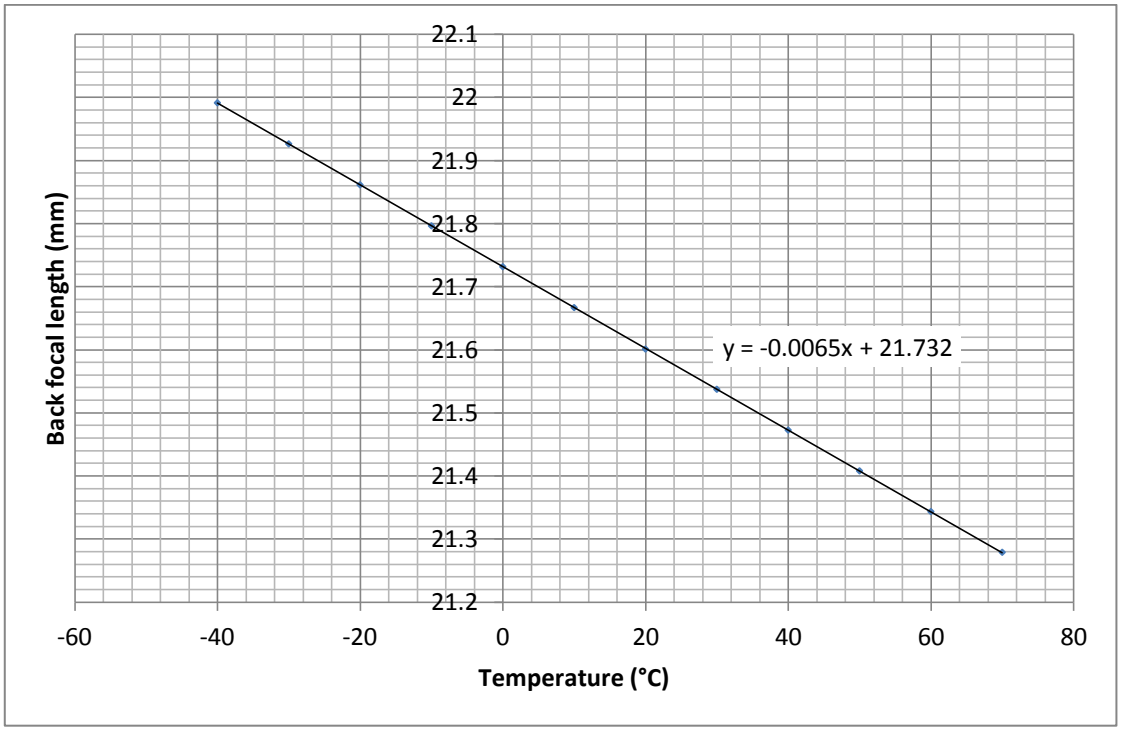

Figure 100 *– Graph showing the linear relationship between temperature and back focal length*

Spot diagrams and diffraction MTF's are shown in ***Figure 101*** to ***Figure 104*** indicating the on axis performance of the system at the two extreme temperatures (-40°C and 70°C).

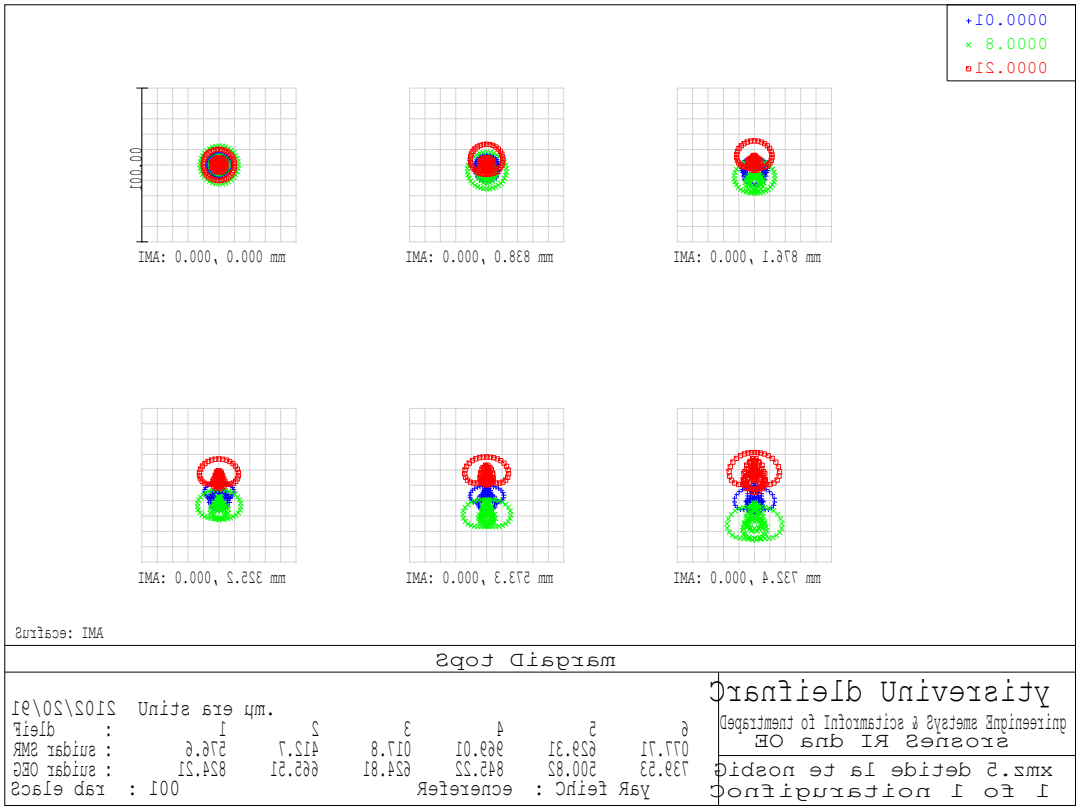

Figure 101 *– Spot diagrams for on axis design at 70°C.*

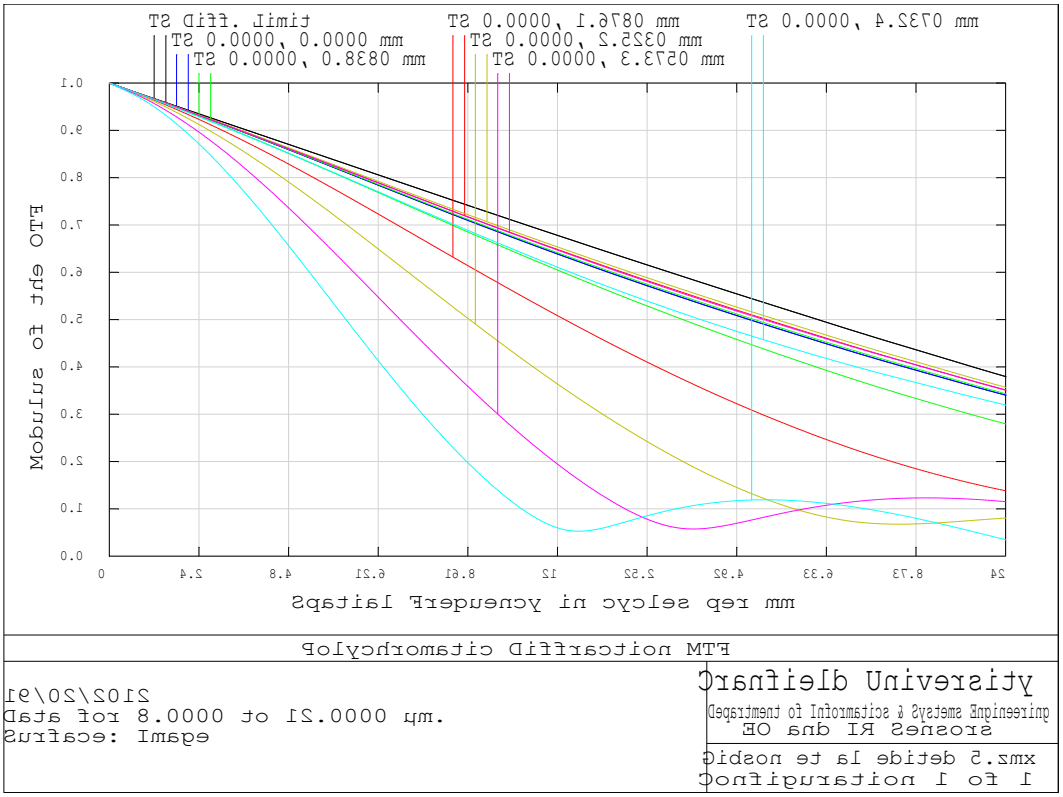

Figure 102 *– Diffraction Mtf curves for on axis system at 70°C.*

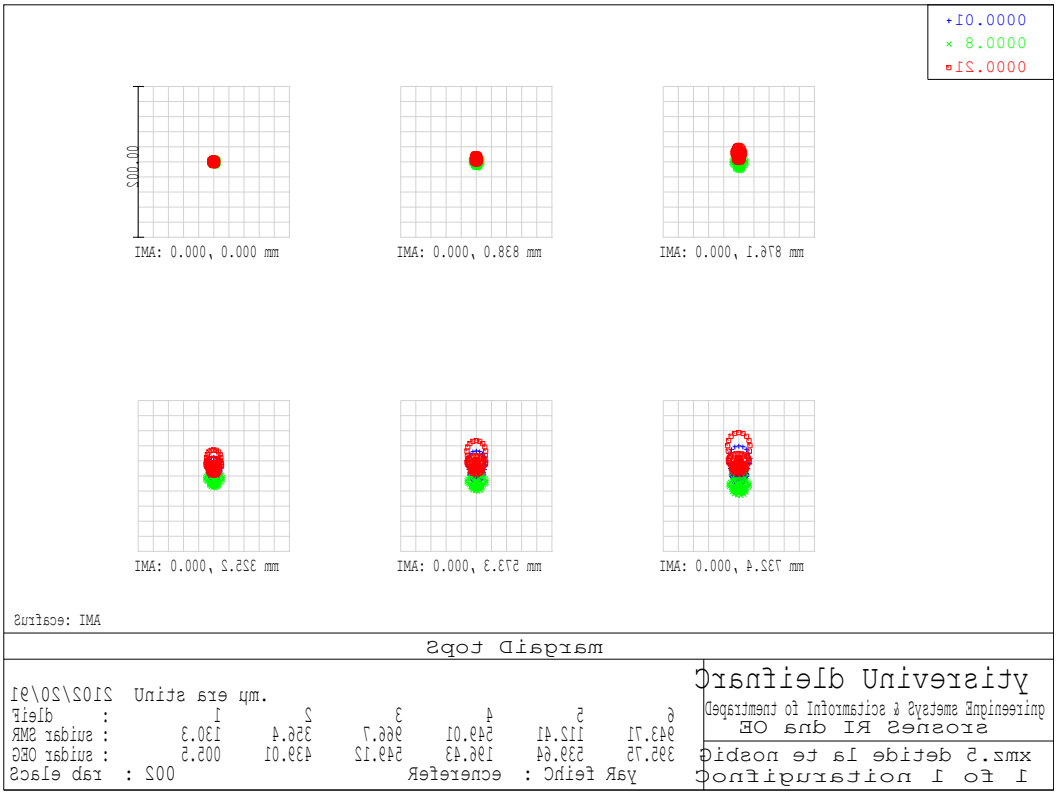

Figure 103 *– Spot diagrams for on axis design at -40°C.*

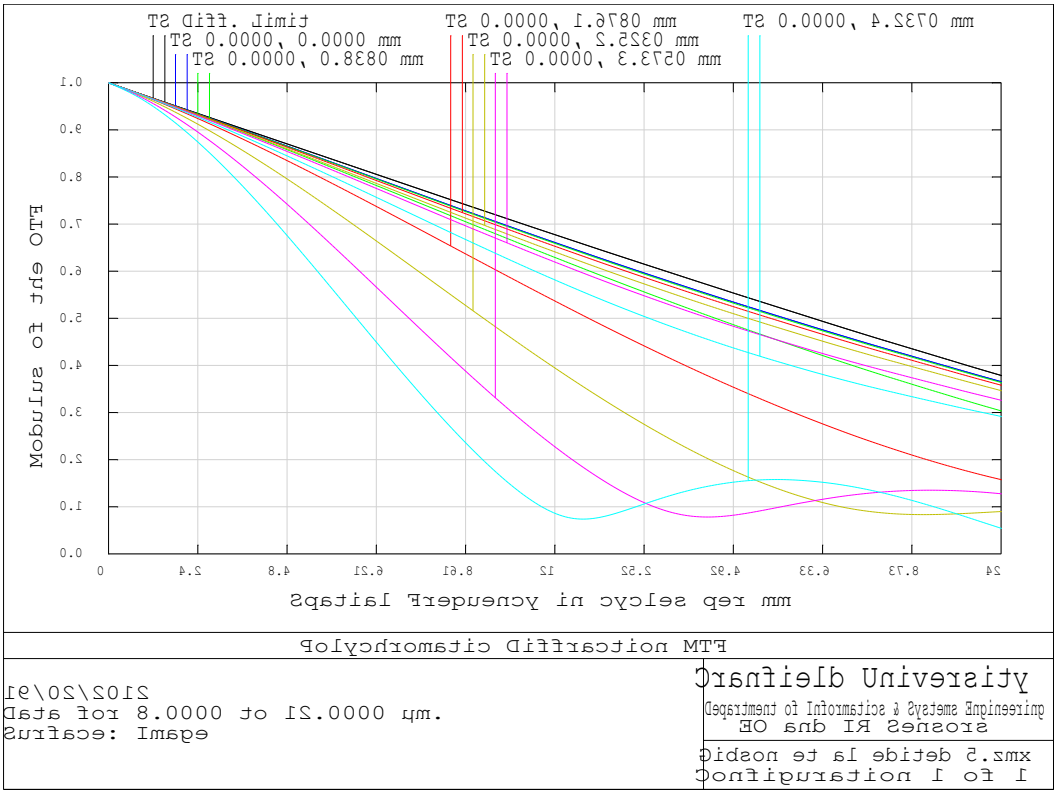

Figure 104 *– Diffraction MTF curves for on axis system at -40°C.*

5. Summary

A review of current state of the art electro-optical technologies is provided. These technologies have been assessed to see which fit the requirements for this project. The most promising technologies have been highlighted with the aid of a table and traffic light system. From here a decision to proceed with an optical design based on the decentred lens technology was made.

Two possible ways in which to achieve line of sight stabilisation in a system consisting purely of lenses and a detector have been shown;

- Moving the detector to counteract movement of the target
- Moving lenses to counteract movement of the target

5.1 Design 1

- Shows promising performance in terms of spot sizes and diffraction MTF
- Has a field of view of ±15° in the x and y planes.
- Fits the requirements of the project with respect to;
    - focal length (48mm)
    - F/# (1 – 1.2)
    - Full field of view (30°)
    - Field of view at sensor level (25.2 mm x 18.9 mm)
    - Track length (≤150mm)
- Shows promising ;
    - Performance over the specified temperature range
- Does not satisfy;
    - Image stabilisation by decentering lenses. Has no decentering capabilities and therefore needs to be stabilised via moving the sensor. This is disadvantageous as wires connected to the sensor are in danger of becoming detached due to movement of the sensor.

- To take this design further the problem with athermalisation could be addressed by further optimisation to improve the performance in terms of spot radius and MTF. This design shows no promise in line of sight stabilisation by moving lenses and so there would be no benefit in further investigating this design in this respect.

5.2 Design 2

- Shows promising performance with respect to on axis spot sizes.
- Shows promise for line of sight stabilisation without moving the image sensor.
- Shows promise in athermal performance with varying back focal length.
- Has a field of view of ±5° in the x and y planes.
- Fits the requirements of the project with respect to;
    - Focal length (48mm)
    - F/# (1 – 1.2)
- Shows promising;
    - Field of view – The field of view can be increased by increasing the diameters of the lenses, however performance becomes increasingly worse as the field angle increases.
    - Field of view at sensor level currently covers ± 4.237mm from the centre of the focal plane in both x and y planes. This can also be increased with larger diameter lenses.
- Does not satisfy;
    - Track length (≤150mm) – Currently the total track length of the design varies between 207.42mm and 207.74mm depending on the surrounding temperature.
    - Moving lens element mass (≤50g) – This design has two moving lens elements. The mass of the first moving lens is 351.38g and the mass of the second moving lens is 231.349g. The total mass of the system is 1161.11g.
- To take this design further the track length and masses could be addressed. By focussing on decreasing the length of the beam steering section of the design it may be possible to decrease the total length and weight of the system. With the current design there is a trade off between size of the lenses and the achievable field of view, with the front surface lens in particular. Higher field angles are achievable by increasing the diameters of the lenses however this increases the mass of the moving elements and the system as a whole. Decreasing the entrance beam diameter would increase the field of view achieved by this design however the entrance pupil diameter is dictated to be between 40mm and 48mm by the desire to have a working F/# of 1-1.2 and a 48mm focal length. With this design there is a trade off between the length of the design and the image quality achieved at the focal plane. It would be possible to reduce the length of the system by removing one of the doublet lenses at the rear of the design however this would reduce the image quality at the focal plane. The performance with respect to diffraction MTF could be improved by inserting another lens in to the design. This however would give

unwanted increases in track length and mass of the system, and also cause losses in power and image quality.

5.3 Other Technologies

Other technologies such as MEMS and FSMs were also considered and show promise for line of sight applications. The control units required to steer FSMs are large in general and would not be ideal for this project. With development in the reduction of response times bimorph actuator based MEMS micro-mirror arrays would be more promising with respects to the requirements of this project. With fast response times the electrostatic based MEMS micro-mirrors are also a promising developing technology. In order for these to fit the system requirements developments in steering angles and optical aperture would need to be made. Larger optical apertures could be made possible with larger arrays of micro-mirrors than are currently available.

6. References

[1] Reflecting Telescope, refractive optical system – Available at: http://edumacation101.wordpress.com/2009/12/03/reflecting-telescopes-vs-refracting-telescopes/ (Accessed May 2011)

[2] Plane mirror – Available at: http://www.daviddarling.info/encyclopedia/L/laws_of_reflection.html (Accessed May 2011)

[3] Convergine mirror – Available at: http://www.antonine-education.co.uk/physics_gcse/Unit_3/Topic_4/topic_4.html (Accessed May 2011)

[4] Diverging mirror – Available at: http://en.allexperts.com/q/Physics-1358/2009/6/convex-mirror-work.html (Accessed May 2011)

[5] Thin Diverging Lens Ray Diagram – Available at: http://www.physics.upenn.edu/courses/gladney/phys151/lectures/lecture_apr_14_2003.shtml. (Accessed May 2011)

[6] Plano-Convex Lens – Available at: http://www.daviddarling.info/encyclopedia/P/plano-convex_lens.html. (Accessed May 2011)

[7] Available Infrared Lenses – Available at: http://www.newport.com/Infrared-Lenses/381068/1033/catalog.aspx. (Accessed June 2011)

[8] Karen Sheard. Image Stabilisation Explained – Available at: http://www.whatdigitalcamera.com/techniques/features/guides/504488/image-stabilisation-explained.html (Accessed March 2012)

[9] Dr. David Fairhurst, Nottingham Trent University (2008), *Optics Lecture Notes*. (unpublished lecture notes).

[10] Liquid Lens Diagraqms – Available at: http://www.physorg.com/news308.html. (Accessed March 2012)

[11] Koyama, Daisuke, Isago, Ryoichi and Nakamura, Kentaro (2011) 'High-speed focusing of a liquid microlens using acoustic radiation force', *21st International Conference on Optical Fiber Sensors*, s.l. 15 May, pg 77535

[12] Oku, Hiromasa, Ishikawa, Masatoshi (2010) 'High-speed liquid lens with 2-ms response and 80.3-nm root-mean-square wavefront error', *MOEMS and Miniaturized Systems IX*, *s.l* 11 February, pg 759407.

[13] Su Xu, Yifan Liu, Hongwen Ren, Shin-Tson Wu (2010) 'A novel adaptive mechanical-wetting lens for visible and near infrared imaging'. *Optics Express*, 18 (12), pp. 12430-12435.

[14] Available liquid lens products – Available at: http://www.optotune.com/index.php?option=com_content&task=view&id=18&Itemid=37 (Accessed March 2012)

[15] Available liquid lens products – Available at: http://www.varioptic.com (Accessed March 2012)

[16] Liquid Crystal Lens by Shin-Tson Wu et al, Institute of Physics publication – Available at: http://physicsworld.com/cws/article/news/24936 (Accessed March 2012)

[17] Huang, Yi-Pai, Chen, Chih-Wei and Huang, Yi-Ching (2011) 'Fast response Fresnel liquid crystal lens for 2D/3D autostereoscopic display', *Advances in Display Technologies; and E-papers and Flexible Displays*, s.l.10 February (2011), pg 79560

[18] Li, Hui, Liu, Kan, Zhu, Chen, et al. (2010) '128 x 128 elements liquid crystal cylindrical lens array with electrically tunable focal length', *Liquid Crystals XIV*,s.l. 19 August 2010, pg 777517.

[19] Bin Wang, Mao Ye and S. Sato (2006) 'Liquid crystal lens with focal length variable from negative to positive values'. *Photonics Technology Letters, IEEE*, 18(1), pp 79-81.

[20] Optra. Compact Beam Steering – Available at: http://www.optra.com/tbcompactbeamsteering.html (Accessed March 2012)

[21] Duncan, Bradley D., Bos, Philip J. and Sergan, Vassili (2003) 'Wide-angle achromatic prism beam steering for infrared countermeasure applications'. *Optical Engineering*, 42(4), pp1038-1047.

[22] Chulwoo Oh, Jihwan Kim, Muth, J., Serati, S. and Escuti, M. J.(2010) 'High-Throughput Continuous Beam Steering Using Rotating Polarization Gratings'. *Photonics Technology Letters, IEEE,* 22(4), pp200-202.

[23] Gibson, Jennifer L., Duncan, Bradley D., Watson, Edward A. and Loomis, John S (2004) 'Wide-angle decentered lens beam steering for infrared countermeasures applications'. *Optical Engineering*, 43(10), pp2312-2321.

[24] Qingkun Zhou, Ben-Tzvi, P., Dapeng Fan and Goldenberg, A. A. (2008) 'Design of Fast Steering Mirror systems for precision laser beams steering', *Robotic and Sensors Environments, ROSE 2008. International Workshop on.* s.l. 2008, pp 144-149.

[25] Fast Steering Mirror System – Available at: http://www.newport.com/ (Accessed March 2012)

[26] Fast Steering Mirror System –Available at: http://www.physikinstrumente.com/en/index.php (Accessed March 2012)

[27] Infrared Mirror Coatings – Available at: http://www.lbp.co.uk/index.html (Accessed March 2012)

[28] Infrared Mirror Coatings – Available at: www.evaporatedcoatings.com/dielectric-mirror-infrared-optical-materials.html (Accessed March 2012)

[29] Infrared Mirror Coatings – Available at: http://www.reynardcorp.com/infrared_technology.php (Accessed March 2012)

[30] Beam Splitters – Available at: http://www.thorlabs.com/NewGroupPage9.cfm?ObjectGroup_ID=4805 (Accessed March 2012)

[31] Beam Splitters – Available at: http://www.edmundoptics.com/onlinecatalog/displayproduct.cfm?productid=3035 (Accessed March 2012)

[32] Lei Wu, Huikai Xie.(2009) 'Large-aperture, rapid scanning MEMS micromirrors for free-space optical communications', *Optical MEMS and Nanophotonics, 2009 IEEE/LEOS International Conference on*, s.l. 2009, pp 131-132.

[33] Huikai Xie.(2008) ‘Large-range large-aperture MEMS micromirrors for biomedical imaging applications’, *Solid-State and Integrated-Circuit Technology, 2008. ICSICT 2008. 9th International Conference on*, s.l. 2008, pp 2549-2552.

[34] Kemiao Jia, Pal, S. and Huikai Xie.(2009) ‘An Electrothermal Tip–Tilt–Piston Micromirror Based on Folded Dual S-Shaped Bimorphs’.*Microelectromechanical Systems, Journal of*, 18(5), pp 1004-1015.

[35] Lei Wu, Dooley, S., Watson, E. A., McManamon, P. F. and Huikai Xie. (2010) ‘A Tip-Tilt-Piston Micromirror Array for Optical Phased Array Applications’. *Microelectromechanical Systems, Journal of*, 19(6), pp 1450-1461.

[36] Lixia Zhou, Kahn, J. M. and Pister, K. S. J. (2006) ‘Scanning micromirrors fabricated by an SOI/SOI wafer-bonding process’. *Microelectromechanical Systems, Journal of*, 15(1), pp 24-32.

[37] Hongjun Zeng, Zhiliang Wan and Feinerman, A. D. (2006) ‘Tilting Micromirror With a Liquid-Metal Pivot’. *Microelectromechanical Systems, Journal of*, 15(6), pp 1568-1575.

[38] Pardo, F., Simon, M. E., Aksyuk, V. A., et al. (2006) ‘Characterization of Piston-Tip-Tilt mirror pixels for scalable SLM arrays’, *Optical MEMS and Their Applications Conference, 2006. IEEE/LEOS International Conference on*, s.l. 2006, pp 21-22.

[39] Milanovic, V., Castelino, K. and McCormick, D. (2006) ‘Fully-Functional Tip-Tilt-Piston Micromirror Array’, *Optical MEMS and Their Applications Conference, 2006. IEEE/LEOS International Conference on*, s.l. 2006, pp 38-39.

[40] Shahriari, Esmaeil, Yunus, W. M. M. and Saion, Elias. (2010) ‘Effect of particle size on nonlinear refractive index of Au nanoparticle in PVA solution’ *Brazilian Journal of Physics*, 40(2), pp 256-260.

[41] Figure 63, Figure 64, and Table 3 – Available at: http://www.u-optic.com/material.htm (Accessed March 2012)

[42] Figure 65- Available at: http://www-cpg.ch.cam.ac.uk/Research/ChalcogenideBasedOpticalWaveguides.php (Accessed March 2012)

[43] Table 4 – Available at: http://www.amorphousmaterials.com/Amtir-1.htm (Accessed March 2012)

[44] He, Guang S., Gvishi, Raz, Prasad, Paras N. and Reinhardt, Bruce A (1995) 'Two-photon absorption based optical limiting and stabilization in organic molecule-doped solid materials' *Optics Communications*, 117(1-2), pp 133-136

[45] Ramani Duraiswami. Image Motion – Available at: http://www.umiacs.umd.edu/~ramani/cmsc426/Lecture18_19_motion.pdf (Accessed March 2012)

[46] Motion Field Picture – Available at: http://of-eval.sourceforge.net/. (Accessed March 2012)

[47] Bray, Mark, Panella, Isabella (2010) 'Research strategy for the electro-optics sensors domain of the Materials and Components for Missiles Innovative Technology Partnership' *Airborne Intelligence, Surveillance, Reconnaissance (ISR) Systems and Applications VII*, s.l. 23 April, pg 7668.

[48] Infrared Lenses – Available at: http://www.irlenses.co.uk/. (Accessed March 2012)

[49] Brand, Richard A., Marks, John E. (1990) 'Composite structures for optical-mirror applications' *Advances in Optical Structure Systems*, s.l. 1 October, pp 488-496.

[50] Wu, L., Maley, S. B., Dooley, S. R., Nelson, T. R., McManamon, P. F. and Xie, H. (2008) 'A large-aperture, piston-tip-tilt micromirror for optical phase array applications' *Micro Electro Mechanical Systems, 2008. MEMS 2008. IEEE 21st International Conference on*, s.l. 2008, pp 754-757.

[51] Kemiao Jia, Samuelson, S. R. and Huikai Xie (2011) 'High-Fill-Factor Micromirror Array With Hidden Bimorph Actuators and Tip–Tilt-Piston Capability' *Microelectromechanical Systems, Journal of*, 20(3), pp 573-582.